PHYSIK-DEPARTMENT

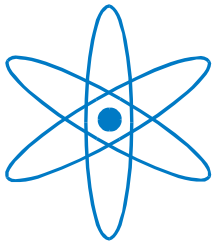

Synthetic and Biological Polyelectrolytes: Detection and Characterization by a Silicon-on-Insulator based Thin Film Resistor

Dissertation von

Petra A. Neff

TECHNISCHE UNIVERSITÄT MÜNCHEN

Physik Department
der Technischen Universität München
Lehrstuhl für Biophysik E22

Synthetic and Biological Polyelectrolytes:

Detection and Characterization by a Silicon-on-Insulator based Thin Film Resistor

Petra A. Neff

Vollständiger Abdruck der von der Fakultät für Physik der Technischen Universität München zur Erlangung des akademischen Grades eines

Doktors der Naturwissenschaften (Dr. rer. nat.)

genehmigten Dissertation.

Vorsitzender:	Univ.-Prof. Dr. Roland Netz
Prüfer der Dissertation:	1. Univ.-Prof. Dr. Andreas Bausch 2. Univ.-Prof. Christine Papadakis, Ph.D.

Die Dissertation wurde am 24.01.2007 bei der Technischen Universität München eingereicht und durch die Fakultät für Physik am 06.03.2007 angenommen.

Contents

Zusammenfassung

Feldeffekt-basierte Halbleiterbauelemente zur markierungsfreien Detektion molekularer Wechselwirkungen stellen eine vielversprechende Entwicklung im Bereich der Biosensorik dar. In den letzten Jahren wurden mehrere derartige Sensoren entwickelt, die es ermöglichen, Nukleinsäuren und Proteine unmittelbar durch ihre elektrische Ladung zu detektieren. In dieser Arbeit wird ein Feldeffektsensor auf Silicon-on-Insulator (SOI)-Basis dazu verwendet, geladene Moleküle markierungsfrei nachzuweisen. Um eine quantitative Analyse der Sensorantwort zu ermöglichen, haben wir eine theoretische Beschreibung entwickelt, die das System in Form von Kapazitäten modelliert. Dieses Kapazitätsmodell berücksichtigt sowohl dielektrische Effekte als auch die Debye-Abschirmung der Molekülladungen durch mobile Ionen in der Nähe der Sensoroberfläche.

Polyelektrolyte mit entgegengesetzten Ladungen können abwechselnd auf die Sensoroberfläche aufgebracht werden. Dabei bilden sich sogenannte Polyelektrolytmultilagen (PEMs), die einzigartige Materialeigenschaften aufweisen. Jedoch können erst dann maßgeschneiderte Materialien hergestellt werden, wenn sowohl die Bildung als auch die Eigenschaften der Filme grundlegend verstanden sind. In dieser Arbeit wurde mit Hilfe des SOI-Sensors die Bildung der PEMs untersucht. Die Adsorption der Polyelektrolyte führt zu einer Änderung des Oberflächenpotentials, was mit den Sensoren in Echtzeit verfolgt werden kann. Durch mobile Ionen innerhalb des Polymerfilms werden die Polyelektrolytladungen abgeschirmt. Dies führt zu einer Abnahme der Potentialänderung mit zunehmender Anzahl von Lagen. Die Detektion der Multilagen können wir mit Hilfe unseres Kapazitätsmodells beschreiben. Dabei haben wir herausgefunden, dass die Abschirmlänge κ^{-1} innerhalb des Polymerfilms größer ist als in der Pufferlösung außen. Außerdem ist die Abschirmlänge in PEMs aus Poly(diallyldimethylammoniumchlorid), PDADMAC und Poly(styrensulfonat), PSS deutlich größer als in PEMs aus Poly(allylaminhydrochlorid), PAH und PSS. Betrachtet man die Ionenverteilung zwischen Polymerfilm und Pufferlösung, können die Dielektrizitätskonstante der PEMs sowie die Konzentration mobiler Ladungen ermittelt werden. Wir konnten zeigen, dass beides signifikant von der Art der verwendeten Polyelektrolyte abhängt. Dies könnte sich als nützlich erweisen für Biosensoranwendungen, wo die Ladung des Analyten nicht durch das darunterliegende Polymerkissen abgeschirmt werden darf. Neben dem Abschirmverhalten der PEMs haben wir auch die pH-Sensitivität von Sensoren untersucht, die mit Polyelektrolyten beschichtet wurden. Dabei bleibt die pH-Sensitivität der Sensoren erhalten, was auf eine hohe Permeabilität der Filme für Protonen hinweist. In einer Reihe von weiteren Experimenten haben wir den Einfluss der Polymerladungsdichte auf die Bildung von Multilagen untersucht. Dazu

wurde PSS in Kombination mit dem statistischen Copolymer Poly(diallyldimethylammoniumchlorid-*stat*-*N*-methyl-*N*-vinylacetamid), P(DADMAC-*stat*-NMVA) mit verschiedenen Ladungsdichten verwendet. Bei einer Ladungsdichte von unter 75% hört die Bildung der Multilagen schon nach wenigen Adsorptionsschritten auf. In früheren Veröffentlichungen wurde eine Ladungsinversion nach jedem Adsorptionsschritt als Voraussetzung für die Bildung von Multilagen angesehen. Wir haben jedoch keine Ladungsinversion beobachtet, sondern festgestellt, dass die Schwelle der Multilagenbildung mit der Schwelle der Kompensation der vorhergehenden Oberflächenladung zusammenfällt.

Der in dieser Arbeit verwendete SOI-Sensor kam nicht nur zur Untersuchung vom PEMs aus synthetischen Polyelektrolyten, sondern auch als Biosensor zum Einsatz. Dazu haben wir eine neue Technik entwickelt, mir der enzymatische Aktivitäten bestimmt werden können. Wir konnten zeigen, dass die Adsorption von Polyelektrolyten im Gegensatz zu der von Monomeren oder kurzen Oligomeren leicht mit dem Sensor nachgewiesen werden kann. Daher können Enzyme, die Polyelektrolyte schneiden, durch eine Verringerung des Sensorsignals nachgewiesen werden. Als Anwendung betrachten wir die Serinendopeptidase Trypsin, die Poly-L-Lysin (PLL) schneidet. Wir konnten zeigen, dass PLL zunächst auf dem Sensor adsorbiert werden kann und dann unmittelbar auf der Oberfläche enzymatisch abgebaut wird. Dabei entstehen hauptsächlich Dimere und Trimere, die aus entropischen Gründen von der Oberfläche desorbieren. Dies führt zu einer messbaren Änderung des Oberflächenpotentials und erlaubt die Detektion von Trypsin bis hin zu 50 ng/ml. Bei Chymotrypsin handelt es sich ebenfalls um eine Endopeptidase, die jedoch eine andere Spezifität als Trypsin besitzt. Tatsächlich haben wir beobachtet, dass Chymotrypsin PLL mit einer geringeren Effizienz schneidet. Mit Hilfe eines kinetischen Modells für enzymatische Oberflächenreaktionen konnten wir die Aktivität von Trypsin quantitativ analysieren. Außerdem konnten wir zeigen, dass Trypsin durch einen Serinproteaseinhibitor gehemmt werden kann. Wir haben die Anwendbarkeit dieser neuen Technik auch anhand eines zweiten Enzyms untersucht. Das sulfatierte Glykosaminoglykan Heparin ist der am stärksten geladene Polyelektrolyt bei Säugetieren. Mit dem SOI-Sensor kann seine Adsorption leicht nachgewiesen werden. Heparin wird selektiv vom Enzym Heparinase I gespalten. Dabei entstehen hauptsächlich Disaccharide, die kaum an die Sensoroberfläche binden. Daher konnte mit Heparinase I behandeltes Heparin durch die verringerte Sensorantwort von einer unbehandelten Probe unterschieden werden. Allerdings konnte die Aktivität der Heparinase I nicht unmittelbar an der Sensoroberfläche verfolgt werden, was auf eine verringerte Zugänglichkeit des Substrats oder eine Inaktivierung des Enzyms durch die Oberflächennähe zurückzuführen sein könnte.

Summary

Field-effect based semiconductor devices for the label-free detection of molecular interactions represent a promising development for biosensor applications. Recently, several such devices have been presented for the direct electrical detection of nucleic acids and proteins. However, a detailed and quantitative understanding of experimental observations is still elusive in most cases. In this thesis, a recently introduced Silicon-on-Insulator (SOI) based thin film resistor is employed for the label-free detection of molecules by their intrinsic charge. To allow for a quantitative analysis of the sensor response, we have developed a theoretical description which models the system in terms of capacitances. This capacitor model accounts for dielectric effects as well as for Debye screening by mobile ions within the layers of molecules bound to the surface.

Polyelectrolytes of opposite charge can be adsorbed alternately to the sensor surface, forming self-assembled polyelectrolyte multilayers (PEMs) with unique material properties. These layered films possess a high application potential, e.g. as sensor materials or functional coatings, for catalysis or optical devices. A fundamental physical understanding of the multilayer assembly and properties is a prerequisite for the tailoring of specific material qualities. In this work, we have investigated the buildup of PEMs. To this end, we have employed the SOI based field effect device for sensing changes in the surface potential. Differently charged polyelectrolytes adsorbing to the sensor surface result in defined potential shifts, which can be monitored in real time. Screening of polyelectrolyte charges by mobile ions within the polymer film leads to a decrease of the potential shifts with the number of layers deposited. We show that our capacitor model can be successfully applied to the detection of these films. Thereby, we found that the screening length κ^{-1} inside the PEMs is increased as compared to the value corresponding to the bulk solution. The obtained screening length is much larger for PEMs consisting of poly(diallyl-dimethyl-ammoniumchloride), PDADMAC and poly(styrene sulfonate), PSS in comparison to PEMs consisting of poly(allylamine-hydrochloride), PAH and PSS. Taking into account the partitioning of mobile ions between the bulk phase and the polyelectrolyte film, we have been able to derive the dielectric constant of the PEMs and the concentration of mobile charges. It was found that the dielectric constant of the polyelectrolyte film and the concentration of mobile ions within the film depend significantly on the type of polyelectrolyte used in the deposition process. This could prove useful for biosensing field effect applications, where it is mandatory that the intrinsic charge of the analyte is not screened by the underlying polymer cushion. In addition to the experiments on the screening properties of PEMs, we have investi-

gated the pH sensitivity of the polyelectrolyte-functionalized SOI sensor. We found that the pH sensitivity is not reduced by the adsorption of PEMs, indicating a high permeability for protons. In a further series of experiments, we have studied the influence of polymer charge density on multilayer buildup using the strong polyanion PSS combined with the statistical copolymer poly(diallyl-dimethyl-ammoniumchloride-*stat*-*N*-methyl-*N*-vinylacetamide), P(DADMAC-*stat*-NMVA) at various degrees of charge (DC). The multilayer formation stops after a few deposition steps for a DC below 75%. In previous publications, charge inversion after each deposition step was discussed as a precondition for multilayer formation. In this work, no inversion of the preceding surface charge was observed. However, we have found that the threshold of multilayer formation corresponds to the threshold of surface charge compensation.

In addition to the study of PEMs built from synthetic polyelectrolytes, we have employed the SOI based field effect device as a biosensor. To this end, we have developed a novel technique for the detection of enzymatic activity. We have found that the adsorption of polyelectrolytes, as opposed to charged monomers or short oligomers, can be readily observed by the sensor. Enzymes, which cleave polyelectrolyte substrates, are therefore detected by a decrease of the polyelectrolyte signal. As an application, we consider the serine endopeptidase trypsin, which cleaves poly-L-lysine (PLL). We show that PLL adsorbs to the sensor and is digested by trypsin directly at the surface. The main products of this enzymatic surface reaction are dilysine and trilysine, which are released into the bulk solution due to entropic reasons. This results in a measurable change of the surface potential allowing for the detection of trypsin concentrations down to 50 ng/ml. Chymotrypsin is a similar endopeptidase with a different specificity. Indeed, it was found that chymotrypsin cleaves PLL with a lower efficiency as compared to trypsin. The activity of trypsin was analyzed quantitatively employing a kinetic model for enzyme-catalyzed surface reactions. Moreover, we have demonstrated the specific inactivation of trypsin by a serine protease inhibitor, which covalently binds to the active site. The applicability of this newly developed technique for the detection of enzymatic activity was examined for a second enzyme. The sulfated glycosaminoglycan heparin is the most highly charged polyelectrolyte in mammalian tissue. Its adsorption can be easily detected by the SOI sensor. Heparinase I cleaves heparin selectively, mainly producing disaccharides, which hardly adsorb to the sensor surface. Therefore, we could distinguish heparinase I treated heparin from an untreated sample by its decreased sensor response. However, the action of heparinase I could not be monitored directly at the sensor surface, which could be attributed to a reduced accessibility of the substrate or an inactivation of the enzyme by the surface proximity.

1 Introduction

Advances in the development of biofunctional semiconductor systems allow for the label-free electrical detection of molecules by their intrinsic charge. Recently, several field effect based semiconductor devices for the detection of nucleic acids [1, 2, 3] and proteins [4, 5, 6] have been presented. At the present time, various substrate materials are studied for their potential in biosensing applications. For example, group III-nitrides have been shown to be nontoxic and stable under physiological conditions [7] operating at a high signal-to-noise ratio [8]. The successful electrochemical passivation of GaAs/AlGaAs heterostructures has been demonstrated allowing stable measurements at a high sensitivity [9]. Moreover, diamond exhibits a good biocompatibility as well as a high stability and has been used for the fabrication of biosensors [5, 10]. In this thesis, an Ion-Sensitive Field-Effect-Transistor (ISFET) based on Silicon-on-Insulator (SOI) is studied, possessing the advantage that standard silicon technology can be used [11]. For all biosensing field effect devices, sensor signals strongly depend on screening effects in the electrolyte solution and on the charge distribution within the biofunctional layers. For a quantitative understanding of the detection mechanisms and the experimental results, we developed a theoretical description based on a capacitor model. This model allows us to relate the response of an ISFET such as the SOI device to a certain change at the sensor surface.

1.1 Polyelectrolyte Multilayers

Polyelectrolyte multilayers (PEMs) have been investigated intensively since they were first proposed [12]. PEMs are prepared by the layer–by–layer deposition of polyanions and polycations from aqueous solutions [13, 14]. The method is very attractive due to its simplicity and its broad range of potential applications. However, for using multilayers as functional materials for complex devices, it is important to understand the internal structure and the formation process [15]. The multilayer thickness, the water content, the mechanical properties and the swelling behavior of different PEMs systems have been extensively studied. During the adsorption process, polyanion/polycation complexes are formed with the previously adsorbed polyelectrolyte layer [16]. The exchange of counterions by the oppositely charged polyelectrolyte could be the reason for the counterion concentration inside the PEMs to be below the detection limit [17]. Thus, it seems that most of the charges within the PEMs are compensated intrinsically by the opposite polymer charges and not by the presence of small counterions. Related to the intrinsic charge compensation may be the strong interdigitation between adjacent layers found by neutron

reflectometry [18, 19]. While the potential of the outer surface of the polyelectrolyte film is well investigated by electrokinetic measurements [20], not much is known about the internal electrostatic properties like ion distribution and mobility. Using a pH-sensitive fluorescent dye, the distribution of protons within the PEMs has been determined [21]. Assuming Debye screening and a constant mobility for all ions within the PEMs the potential drop within polyelectrolyte films composed of poly(allylamine hydrochloride) (PAH) and poly(sodium 4-styrenesulfonate) (PSS) has been calculated. From these measurements an independent determination of the ionic strength and the dielectric constant was not possible. Direct measurements of the potential drop inside the PEMs would be best suited for determining electrostatic properties such as the Debye length or the dielectric constant of the PEMs. The capacitance of the PEMs can be measured by electrochemical methods such as AC voltammetry [22]. Another approach is the use of field effect devices which allows the determination of the surface potential at the sensor/electrolyte interface. This is in contrast to electrokinetic studies, where the potential at a shear plane outside the outer Helmholtz plane is measured with respect to the outer solution bulk value. Therefore, the changes in surface potential measured by a field effect device are strongly dependent not only on the amount of charge adsorbed to the outermost surface, but also on screening effects within the multilayers *inside* the polyelectrolyte films, which cannot be determined by zeta potential measurements. The deposition of PAH/PSS as well as poly(L-lysine)/DNA multilayers and even DNA hybridization have been detected by such devices [1, 2, 3]. However, the quantitative response of the sensor has not yet been related to the dielectric properties and ion mobility inside the PEMs. It remains a crucial question how these properties are affected by the chemical nature of the polymers. While most times polyelectrolytes are described in a coarse-grained model neglecting their specific chemical nature, it could well be that the backbone of the polymer has an important influence on the PEMs properties. Multilayers with different dielectric properties could prove useful for the specific application in the functionalization of biosensing field effect devices. It is desirable to separate the silicon dioxide from the aqueous solution and possibly decrease unspecific adsorptions. However, for such applications it is mandatory that the intrinsic charge of the analyte is not screened by the underlying polymer cushion [6]. In this thesis, different polyelectrolyte systems have been investigated. The SOI based thin film resistor can be used to monitor in real time the build up of polyelectrolyte multilayers. The deposition of the differently charged polyelectrolytes results in defined potential shifts. At the same time, the SOI device proves useful for the characterization of PEMs giving insight into the buildup process as well as the physical properties.

As yet, the charge inversion after each deposition step has been discussed as a pre-

condition for multilayer formation, and it was assumed that electrostatic interactions are its main driving forces [14, 23]. This was supported by the fact that in electrokinetic measurements the zeta potential changes its sign after each deposition step, resulting in a kind of zigzag curve [20]. In electrokinetic measurements, the surface potential itself is not accessible. Further on, the importance of electrostatic interactions was underlined by studies of the effect of polymer charge density. There, the influence of polymer charge was studied using the strong polyanion PSS combined with the linear statistical copolymer poly(diallyl-dimethyl-ammoniumchloride-*stat*-*N*-methyl-*N*-vinylacetamide) (P(DADMAC-*stat*-NMVA)) at various degrees of polymer charge (DC). It was found that the multilayer formation stops after a few deposition steps for a DC below 75 % [24, 25, 26, 27, 28]. Besides the balance of electrostatic attraction and repulsion, the gain in entropy due to the release of counterions is one of the driving factors of multilayer formation. Moreover, also non-electrostatic contributions such as hydrogen bonding and hydrophobic interactions play a role in multilayer stabilization [29, 30, 31]. Recent theoretical studies have demonstrated that non-electrostatic short range interactions strongly influence multilayer formation [32, 33], and polymer specific effects on multilayer formation have been observed. Here, the influence of polymer charge density on multilayer buildup is studied using polyelectrolytes at various degrees of charge. Employing a field effect based sensor device, variations of the surface potential can be directly determined. We found that multilayer formation requires a certain minimal charge density corresponding to the threshold of surface charge compensation. However, no inversion of the preceding surface charge was observed.

1.2 Biosensing Applications

Since the development of the first biosensor in 1962 [34], research and the number of publications in the field have enormously increased [35]. Meanwhile, also numerous field effect devices have been presented among the variety of different concepts for the realization of biosensors. Silicon-based devices possess several advantages, among them are the small size and weight, fast response, high reliability, on chip integration of biosensor arrays and the prospect of low-cost mass production [36]. A definition for an electrochemical biosensor was given by the IUPAC (International Union of Pure and Applied Chemistry) [37]: "An electrochemical biosensor is a self-contained integrated device, which is capable of providing specific quantitative or semi-quantitative analytical information using a biological recognition element (biochemical receptor) which is retained in direct spatial contact with an electrochemical transduction element." Different types of molecules or

living biological systems may serve as biological recognition elements; among these are enzymes, antibodies, antigens, proteins, nucleic acids, cells, tissue, intact organs or whole organisms [36]. The specific biomolecular interaction with the analyte produces a change which is converted by the transduction element into an electrical signal. Bioaffinity sensors are based on recognition elements, e.g. antibodies or nucleic acids, which specifically bind to analyte molecules. Biocatalytic biosensors are based on enzymes, which combine the specific binding with a specific biochemical reaction. In most cases, surface immobilized enzymes have been used [38, 39, 40, 41], where a substrate in solution reacts to create a detection signal. Accordingly, in a classical enzyme field effect transistor (ENFET), immobilized enzymes are used for the direct analysis of substrates or inhibitors [42]. The first ENFET, which was presented in 1980, was designed for penicillin determination using the membrane-bound enzyme penicillinase [43]. The catalyzed reaction produces protons and therefore decreases the local pH, which is detected by the sensor. Indeed, in most reported ENFETs protons are produced or consumed by an enzymatic reaction [44]. It is a drawback of ENFET technology that only a limited number of enzymes can produce or consume electrochemically active species such as protons [36].

In this thesis, the SOI sensor is employed as a biosensor for the detection of enzymatic activity. As opposed to the classical ENFET, the enzyme is not used as the biological recognition element, but it is the analyte to be detected. Therefore, it is not immobilized but free in the buffer solution. A suitable substrate must be immobilized on the sensor surface. This substrate serves as the biological recognition element. In the course of the enzymatic reaction, a change occurs at the surface, which can be transduced by the sensor into a measurable signal. Here, enzymes are used which cleave polyelectrolyte substrates. The adsorption of polyelectrolytes is easily observed by field effect devices due to the high charge density. When the adsorbed polyelectrolytes are enzymatically cleaved into smaller fragments, these fragments desorb from the sensor surface changing the surface charge. This change is transduced by the SOI sensor into an increase or decrease of the current, depending on the polyelectrolyte charge. Thereby, the activity of the enzyme can be directly monitored in real time allowing for a kinetic analysis. A schematic picture of the reaction is shown in Fig. 1.1. The application of the method is limited to enzymes for which a suitable polyelectrolyte substrate is available. In this thesis, the activity of the serine endopeptidases trypsin and chymotrypsin is detected via the degradation of an immobilized polypeptide substrate. The detection of the glycosidase heparinase I could not be observed directly at the sensor surface, here the reaction had to be carried out in bulk solution. The subsequent addition of the reaction mixture to the sensor device allows for the detection of the heparinase I activity.

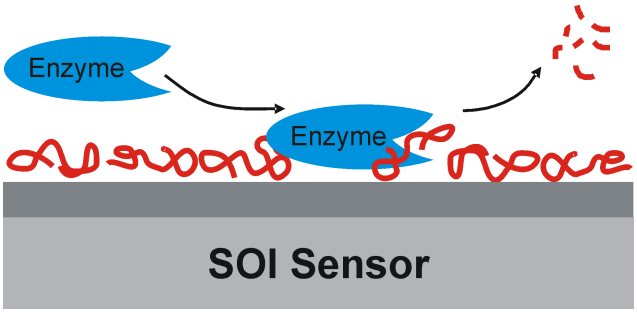

Figure 1.1: Polyelectrolytes are used as substrates for an enzymatic reaction. The enzyme cleaves the polyelectrolyte substrate into smaller fragments, which desorb from the sensor surface. The activity of the enzyme is monitored in terms of a surface potential change.

The determination of enzymatic activity is widely used, e.g. for medical diagnostics, for the study of metabolic cycles or for the monitoring of biotechnological processes [45]. The characterization of enzymes regarding their catalytic properties requires the measurement of their turnover rate at different conditions. Optical methods such as photometry and fluorimetry are the most frequently used techniques in enzyme analysis [45]. These reactions are usually carried out in bulk. When enzymes in solution are combined with an immobilized substrate, a special reaction scheme has to be considered. In this case, the amount of enzyme is in excess as compared to the amount of substrate on the surface. In this thesis, the activity of trypsin could be analyzed quantitatively applying a model for surface-catalyzed reactions [46].

2 Theory

2.1 Ion-Sensitive-Field-Effect-Transistors (ISFETs)

The Silicon-on-Insulator based sensor devices used here work according to the basic principles of the Ion-Sensitive Field-Effect-Transistor (ISFET). The ISFET has been introduced more than 30 years ago by Bergveld [47]. These sensors were initially mainly meant for biomedical applications such as electrophysiological measurements and only in the later years went in the direction of ion sensing in general [35]. An ISFET is basically a Metal-Oxide-Semiconductor Field-Effect-Transistor (MOSFET) in which the gate metal is replaced by a reference electrode inserted in an aqueous solution, which is in contact with the gate oxide. Usually, a MOSFET is composed of a Metal-Oxide-Semiconductor (MOS) diode and two p-n-junctions. When a gate voltage is applied to the metal gate of the transistor, a conducting channel is formed between the source and the drain. The conductance of this channel can be modulated by varying the gate voltage. In an ISFET the conductance of the channel is modulated by variations of the surface potential at the gate oxide/electrolyte interface. MOSFETs and ISFETs can also be fabricated on insulating substrates (Silicon-on-Insulator – SOI), e.g. on silicon oxide. Compared with bulk silicon devices, the isolation scheme of a SOI device is simplified and does not need complicated well structures [48]. In the ideal MOS structure, the energy band is flat (flat-band condition) when no gate voltage V is applied (Fig. 2.1(a)). This means that the energy difference between the metal work function and the semiconductor work function is zero. When positive or negative bias voltages are applied, three cases can be considered at the semiconductor surface: For a p-type semiconductor, a negative voltage applied to the metal gate will induce an upward bending of the energy bands and therefore an *accumulation* of holes (Fig. 2.1(b)). When small positive voltages are applied, the energy bands are bent downward leading to a *depletion* of holes (Fig. 2.1(c)). When even larger positive voltages are applied, the bands bend down further and negative carriers are induced (*inversion*, Fig. 2.1(d)). In a practical MOS, the work function difference is generally not zero. To achieve ideal flat-band conditions, an external voltage has to be applied (flat band voltage). Additionally, charges in the oxide and at the semiconductor/oxide interface affect the flat band voltage. In an ISFET, the gate voltage is replaced by the potential of the reference electrode and the characteristics of the Electrolyte-Oxide-Semiconductor (EOS) system determines the functioning of such a sensor. The potential profile in an EOS system is sketched in Fig. 2.2. The chemical sensitivity of an ISFET is related to a variation of the potential at the electrolyte-oxide interface caused by a

variation of the electrolyte composition. In the following, the electrochemical properties of the electrolyte-oxide interface will be discussed.

2.2 Electrolyte-Oxide Interface

When two phases are brought into contact, a potential difference is generated at the interface. An electrical double layer is created and the surface charges are screened by the ions in the electrolyte solution. The potential distribution in the electrical double layer at flat surfaces can be described using the Gouy-Chapman model [49]. In this model, due to the thermal motion a diffuse layer of charges is assumed leading to a statistical distribution of the ions in the electrical field. The potential ψ and the charge density at the interface are related by the Poisson equation. Combining a Boltzmann distribution of the ions with the Poisson equation, the Poisson-Boltzmann equation is obtained:

$$\Delta\psi = -\frac{e}{\varepsilon_0\varepsilon_r}\sum_i n_i^0 z_i \exp\left(-\frac{z_i e\psi}{kT}\right) \tag{2.1}$$

with the elementary charge e, the vacuum permittivity ε_0, the relative permittivity ε_r, the bulk concentration n_i^0 and valency z_i of the ion of type i, the Boltzmann constant k and the temperature T.

2.2.1 Debye-Hückel Approximation

In general, this differential equation cannot be solved explicitly. However, for small values of the potential $z_i e\psi < kT$ the exponential can be expanded up to first order (Debye-Hückel approximation) leading to

$$\Delta\psi = \frac{e^2\sum_i n_i^0 z_i^2}{\varepsilon_0\varepsilon_r kT} = \kappa^2\psi \tag{2.2}$$

with the Debye length

$$\kappa^{-1} = \left[\frac{\varepsilon_0\varepsilon_r kT}{e^2\sum_i n_i^0 z_i^2}\right]^{\frac{1}{2}}. \tag{2.3}$$

For the boundary conditions $\psi(0) = \psi_\mathrm{S}$ and $\psi(\infty) = 0$ an exponential potential distribution is obtained

$$\psi(x) = \psi_\mathrm{S}\exp\left(-\kappa x\right). \tag{2.4}$$

The thickness of the diffuse double layer is characterized by the Debye length κ^{-1}, which is inversely proportional to the square root of the ionic strength $I = \frac{1}{2}\sum_i n_i^0 z_i^2$ of the

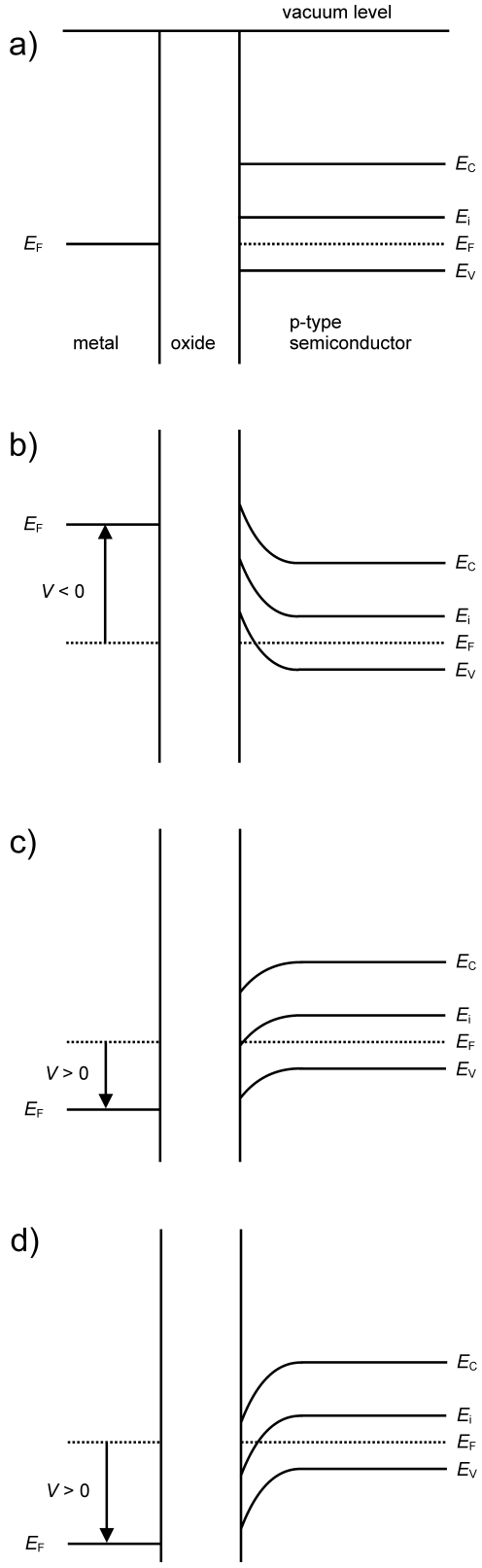

Figure 2.1: Energy band diagrams of an ideal MOS: a) flat band condition, b) accumulation, c) depletion and d) inversion. E_F, E_i, E_C, and E_V are the Fermi level, the intrinsic Fermi level, the conducting band energy and the valence band energy, respectively.

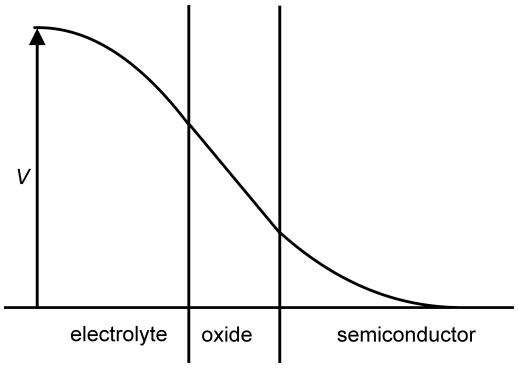

Figure 2.2: Sketch of the potential profile in an EOS system. The voltage V is applied by the reference electrode.

solution.

2.2.2 Solution of the Poisson-Boltzmann Equation for Symmetric z:z Electrolytes

For symmetric z:z electrolytes ($z = |z_i|$), the Poisson-Boltzmann equation can be integrated without the restrictions of the Debye-Hückel approximation, i. e. also for $ze\psi > kT$. Imposing the boundary conditions given above the potential profile is given by [50]

$$\frac{\tanh\left(ze\psi/4kT\right)}{\tanh\left(ze\psi_{\mathrm{S}}/4kT\right)} = \exp\left(-\kappa x\right). \tag{2.5}$$

Again, in the limit of small values of the potential ($ze\psi < 2kT$), an exponential form is obtained as for the linear equation. This form is a good approximation for $\psi < 50$ mV at room temperature. A relation between the surface charge σ_{S} and the potential ψ_{S} (Grahame equation) can be obtained for arbitrary ψ from the Gauss' law imposing charge neutrality as shown in Ref. [50] yielding

$$\sigma_{\mathrm{S}} = \left(8\varepsilon_0\varepsilon_r kTn^0\right)^{\frac{1}{2}} \sinh\left(\frac{ze\psi_{\mathrm{S}}}{2kT}\right). \tag{2.6}$$

For $ze\psi < 2kT$ this relation can be linearized to

$$\sigma_{\mathrm{S}} = \varepsilon\kappa\psi_{\mathrm{S}}. \tag{2.7}$$

The quantity $\varepsilon\kappa$ has the dimension of a capacitance. Eq. (2.7) shows that for small values of the potential the diffuse layer behaves like a parallel plate capacitor with a spacing of

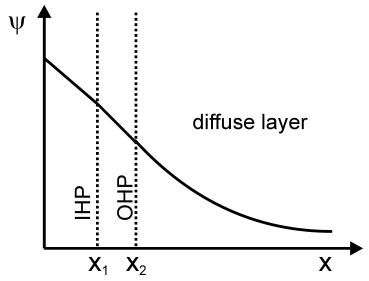

Figure 2.3: Sketch of the potential profile of the electrical double layer. The inner and outer Helmholtz planes (IHP and OHP) form the Stern layer. Beyond a distance of x_2 from the surface, the potential drops according to the Gouy-Chapman model (diffuse double layer).

the Debye length κ^{-1} between the plates.

2.2.3 Stern's Modification

In the Gouy-Chapman model, ions are considered as point charges and as such they can approach the surface arbitrarily close. Stern's modification of the model takes into account the finite radius of the hydrated counter ions assuming a plane of closest approach for the centers of the ions at a distance x_2. This plane is called the outer Helmholtz plane. In addition to nonspecifically adsorbed counter ions, specifically adsorbed dehydrated ions can be taken into account. They are assumed to be situated at a distance $x_1 < x_2$ in a plane called inner Helmholtz plane. Between the surface and the inner and outer Helmholtz planes (in the Stern layer), the potential drops linearly, while at larger distances from the surface the Poisson-Boltzmann equation applies and the potential drops according to the Gouy-Chapman model. A sketch of the potential profile is given in Fig. 2.3.

2.2.4 Site-Binding Model

The surface charge on a silicon oxide surface depends on the pH of the electrolyte solution. The amphoteric -SiOH sites on the silicon oxide are in equilibrium with the electrolyte by exchanging protons. As protons are charged species, this equilibrium depends on the surface potential ψ_S. The relation between the surface charge σ_S and ψ_S can be described by the site-binding model [51]. The surface reactions are given by

$$-\mathrm{SiOH}_2^+ \rightleftharpoons -\mathrm{SiOH} + \mathrm{H}^+ \tag{2.8}$$

and

$$-\mathrm{SiOH} = -\mathrm{SiO^-} + \mathrm{H^+} \tag{2.9}$$

with the equilibrium constants

$$K_\mathrm{A} = \frac{[-\mathrm{SiOH}]\left[\mathrm{H^+}\right]_\mathrm{S}}{\left[-\mathrm{SiOH_2^+}\right]} \tag{2.10}$$

and

$$K_\mathrm{B} = \frac{\left[-\mathrm{SiO^-}\right]\left[\mathrm{H^+}\right]_\mathrm{S}}{[-\mathrm{SiOH}]} \tag{2.11}$$

where $\left[\mathrm{H^+}\right]_\mathrm{S}$ is the activity of protons at the surface. $\left[\mathrm{H^+}\right]_\mathrm{S}$ is related to the activity of protons in the bulk (and thus the pH) by a Boltzmann distribution:

$$\left[\mathrm{H^+}\right]_\mathrm{S} = \left[\mathrm{H^+}\right] \exp\left(-e\psi_\mathrm{S}/kT\right). \tag{2.12}$$

The number of surface sites is given by

$$N_\mathrm{S} = [-\mathrm{SiOH}] + \left[-\mathrm{SiOH_2^+}\right] + \left[-\mathrm{SiO^-}\right] \tag{2.13}$$

and the total surface charge is given by

$$\sigma_\mathrm{S} = e\left(\left[-\mathrm{SiOH_2^+}\right] - \left[-\mathrm{SiO^-}\right]\right). \tag{2.14}$$

Combining these equations, we obtain σ_S as a function of ψ_S

$$\sigma_\mathrm{S} = eN_\mathrm{S}\frac{\left(\left[\mathrm{H^+}\right]/K_\mathrm{A}\right)\exp\left(-e\psi_\mathrm{S}/kT\right) - \left(K_\mathrm{B}/\left[\mathrm{H^+}\right]\right)\exp\left(e\psi_\mathrm{S}/kT\right)}{1 + \left(\left[\mathrm{H^+}\right]/K_\mathrm{A}\right)\exp\left(-e\psi_\mathrm{S}/kT\right) + \left(K_\mathrm{B}/\left[\mathrm{H^+}\right]\right)\exp\left(e\psi_\mathrm{S}/kT\right)}. \tag{2.15}$$

The Grahame equation (Eq. (2.6)) or for small potentials Eq. (2.7) also give σ_S as a function of ψ_S. The combination of either equation with Eq. (2.15) unambiguously defines σ_S and ψ_S at a given ionic strength and a given pH. A modification that also accounts for the influence of the Stern layer is given in Ref. [52].

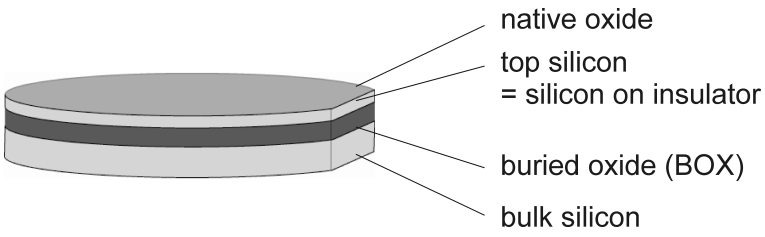

Figure 3.1: Typical layer structure of Silicon-on-Insulator (SOI). The top silicon layer is covered by a native oxide. The bulk silicon wafer is separated from the top silicon by an insulating layer of silicon oxide (buried oxide).

3 Experimental Part

In recent years, SOI technology has gradually been adopted by industrial manufacturers, however mainly limited for use in high-end applications as the costs still exceed the costs of generic CMOS technology. SOI is a layered structure consisting of a thin layer of silicon, which is created on an insulating substrate such as silicon oxide. A typical layer structure is shown in Fig. 3.1. The conducting silicon layer is sandwiched between two oxide layers, the top oxide later serving as gate oxide in devices, and the buried oxide (BOX) insulating the channel from the substrate wafer. Here, chips were fabricated from commercially available ELTRAN wafers (Canon). In the ELTRAN (epitaxial layer transfer) process, a handle wafer is bonded on top of a seed wafer, on which epitaxial silicon has been grown and partially oxidized. A water jet is used to split the bonded wafers, and the seed wafer can be reused. The process is described in detail in Ref. [53]. For our devices, wafers with a handle wafer thickness of 675 μm, a BOX thickness of 200 nm and a slightly boron-doped (10^{16} cm^{-3}) top silicon layer of 30 nm were used. In the following, the production of the SOI sensors as well as the measurement setup and method are described in detail. The operation of the sensor is illustrated and its calibration using a Ag/AgCl reference electrode is explained.

3.1 Sensor Fabrication

For the fabrication of SOI sensors, the 6 inch wafers were first sliced into 0.93×0.93 cm^2 pieces by a wafer saw (K&S Wafer Dicing System 784, Lehrstuhl für Feingerätebau und Mikrotechnik, TU München). Next, they were sonicated for 1 min in acetone and isopropanol and dried in a nitrogen stream. For the photolithography, a positive photoresist (S1805) was spin-coated onto the chips (40 s at 9000 rpm). The photoresist was dried for 30 min at 90°C (soft bake). The masks used for the photolithography are shown in

Fig. 3.2. The photoresist-coated chips were consecutively illuminated with UV light using the structures (a) for the outer edge definition and (b) for the definition of the hallbar structure. After illumination, the structures were developed for 10 s, rinsed with water and dried in a nitrogen stream. The photoresist was hard-baked for 120 min at 120°C. For the definition of the sensitive structure, part of the top-silicon has to be removed down to the oxide layer. The silicon was etched for 90 – 120 s in a solution containing 50% nitric acid and 0.5% hydrofluoric acid. At the time when the silicon is completely removed, the color changes to black, which was used as an indicator for the etching time. Afterwards, the chips were rinsed three times with water and dried in a nitrogen stream. In a second photolithography step the contact pads for the metallization were defined. The positive photoresist S1818 was spin-coated onto the chips for 40 s at 6000 rpm. After the soft bake (30 min at 90°C), the chips were illuminated with UV light using structure (c). After illumination, the structure was developed for 10 s, rinsed with water and dried in a nitrogen stream. Prior to metallization, the chips were glued onto a microscopic slide using a droplet of photoresist which was dried for 10 min at 90°C. Immediately before metallization, the native oxide was removed in hydrofluoric acid vapor by holding the chips over a bottle containing 50% hydrofluoric acid for 2 min. Metal contacts were deposited in an electron beam evaporation chamber (20 nm Ti, 300 nm Au). Photoresist and excess metal were removed in a lift-off process using acetone. The chips were cleaned using acetone and isopropanol and dried in a nitrogen stream. Next, the chips were glued into a chip carrier using a conductive coat creating a contact with the substrate (back gate contact). The gold wires were not bonded directly to the contact pads to avoid a leakage from the top silicon to the substrate. Instead they were glued onto the contact pads using a two-component conductive coat. This coat was dried for 60 min at 90°C before the chips could be encapsulated with a silicone rubber glue to insulate the contacts from the electrolyte solution.

3.2 Measurement Setup and Method

The bonded and encapsulated chip is inserted into a socket. Every lead is connected to a BNC connector, which can be contacted separately. A flow chamber is put on top of the encapsulated sensor. The electrolyte solution is contacted with a Ag/AgCl reference electrode to which a reference voltage U_{ref} is applied. A back gate voltage U_{bg} is applied to the sensor substrate to control the charge carrier density in the conducting channel. A photograph of the setup is shown in Fig. 3.3. The sheet resistance of the device is measured in a four point geometry (Fig. 3.4): The voltage U_{sd} is applied between the

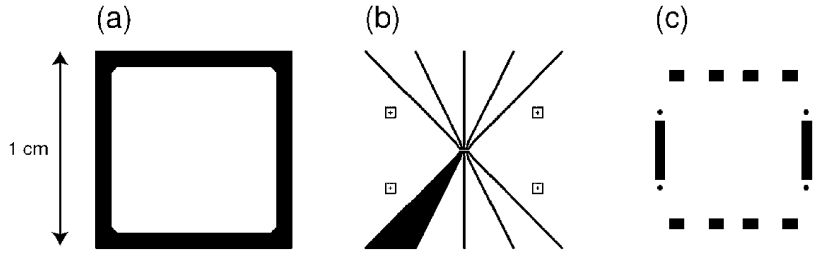

Figure 3.2: Masks used for the photolithography of the sensor processing. Structures (a) and (b) are used to define the outer edge and the active region in the etching process. Structure (c) defines the contact pads for the metallization.

source and the drain of the device and the current I_{sd} is measured. At the same time, the voltage drop V between two of the inner contacts (four point contacts) is measured. All instruments used were connected to a computer and controlled via a GPIB interface. The measurement software is written in LabVIEW and is described in detail in Ref. [54]. For the determination of the sheet resistance, a voltage-current characteristics (U_{sd} vs. I_{sd} or V vs. I_{sd}) is measured in the linear regime. The two- and four-point resistances are given by the slope of these characteristics, respectively, and can be plotted against measurement time. A back gate characterization was used to define the working point of the sensor. At high back gate voltages, the charge carrier concentration is in the saturation regime (strong inversion). Thus, a change in surface potential only leads to a small change in resistance. In contrast, at low back-gate voltages, the charge carrier density is low (weak inversion) yielding a high sensitivity. At the same time however, the noise level is comparatively high. At the working point, the optimum signal-to-noise ratio is obtained. Typical working points were in the range of $U_{\mathrm{bg}} = 20 - 30$ V.

3.3 Sensor Calibration

The Ag/AgCl reference electrode is used to control the potential of the electrolyte solution and for calibration. Before each experiment, a calibration measurement relating a change in sheet resistance ΔR to the corresponding change in surface potential $\Delta\psi_{\mathrm{S}}$ was performed. A certain change in the reference voltage is equivalent to a change in surface potential of the same magnitude when the capacitance of the sensor chip C_{S} is small compared to the capacitance of the electrical double layer C_{D}. This can be illustrated by a series connection of C_{S} and C_{D}. Here, a change in the reference voltage ΔU_{ref} corresponds

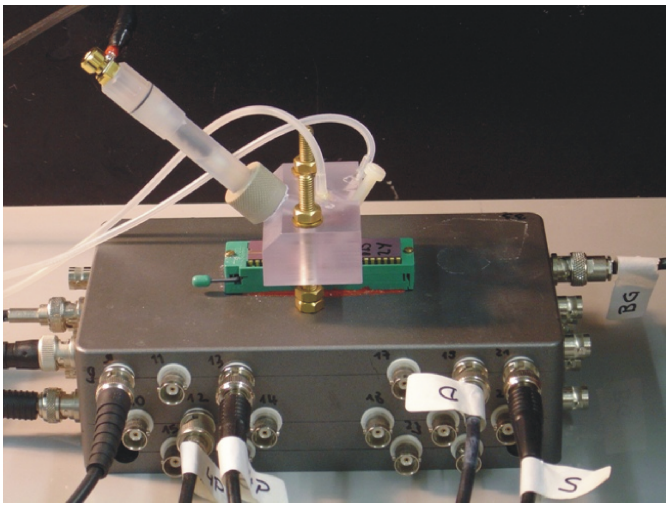

Figure 3.3: Measurement setup: The sensor is plugged into a socket. A flow chamber including a Ag/AgCl reference electrode is put on top of the encapsulated chip.

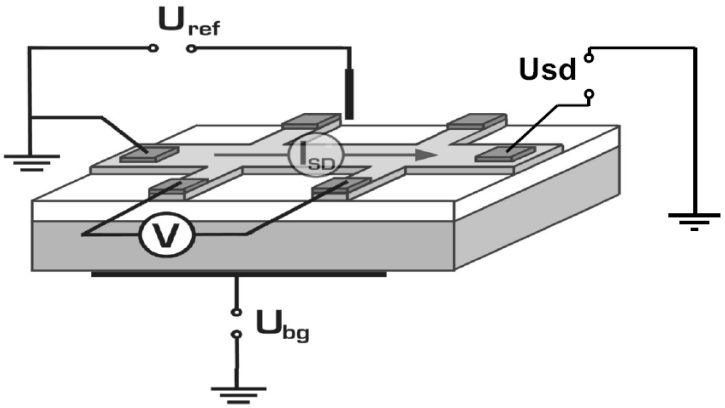

Figure 3.4: Schematic view of the measurement geometry: The voltage U_{sd} is applied between the source and the drain. The current I_{sd} and the voltage drop V are measured allowing the determination of the sheet resistance. A Ag/AgCl reference electrode is used to contact the electrolyte solution with a reference voltage U_{ref}.

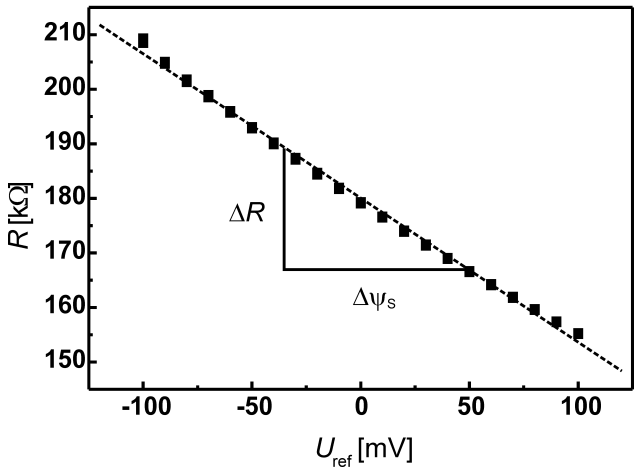

Figure 3.5: Typical calibration curve. A change in sheet resistance ΔR can be related to a corresponding change in surface potential $\Delta\psi_{\mathrm{S}}$.

to a change in surface potential $\Delta\psi_{\mathrm{S}}$ according to

$$\Delta\psi_{\mathrm{S}} = \frac{C_{\mathrm{D}}}{C_{\mathrm{S}} + C_{\mathrm{D}}} \Delta U_{\mathrm{ref}}. \tag{3.1}$$

In Ref. [52] a maximal error of 5% was estimated. Therefore, the sensors can be calibrated by measuring the sheet resistance at different reference voltages U_{ref}. A typical calibration curve (frontgate characteristics) is shown in Fig. 3.5. During an experiment, U_{ref} is set to zero.

4 Results and Discussion

This chapter is structured as follows: First, a theoretical description for the quantitative analysis of the sensor response and the detection of polyelectrolyte multilayers (PEMs) is introduced. Next, the experimental study and characterization of PEMs employing the SOI based sensor are presented and discussed. Subsequently, a newly developed technique for the detection of enzymatic activity using polyelectrolyte substrates is demonstrated. Eventually, the detection of the protein Bovine Serum Albumin (BSA) is shown, and an interpretation of the results is given in terms of a dipolar adsorption.

4.1 Capacitor Model: A Quantitative Description of the Sensor's Response

Field-effect devices such as the SOI device used here allow for the determination of variations of the surface potential at the silicon oxide/electrolyte interface. For a quantitative analysis of the sensor signal, we need to relate a certain change in surface potential to a corresponding change at the sensor surface, such as the binding of charged molecules. For this purpose, a one dimensional capacitor model was developed. In combination with the sensor calibration, this allows us to relate the sensor signal, e.g. sheet resistance, directly to the sensor functionalization. It is assumed that the sheet resistance depends linearly on the surface potential, which is a good approximation for changes of the surface potential in the order of 100 mV, as can be seen from the typical frontgate characteristics (Fig. 3.5). A basic approach to the analysis of field effect devices based on silicon/silicon oxide has been presented in Ref. [55]. The fundamentals of this description have been applied here. First, we derive a basic expression for multiple charged layers on top of a field effect device. Second, we include screening by mobile ions into our description and give an equation for the quantitative analysis of PEMs.

4.1.1 Basic Model for Multiple Charged Layers

A capacitor model used for the determination of the surface potential and thus the sensor signal of a field effect device functionalized with multiple charged layers is derived here. It can be adapted to a specific problem such as the charge distribution in polyelectrolyte multilayers [56] or in adsorbed protein layers [57] as shown later. The potential at the sensor surface is calculated as a function of additional charged layers located next to the surface. The system consisting of the sensor and these additional layers is described in

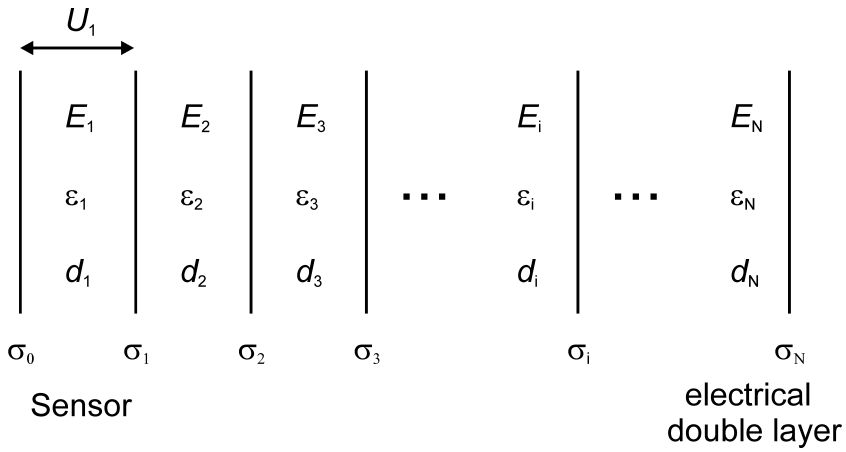

Figure 4.1: A capacitor model consisting of $N+1$ charged plates is used to describe the system consisting of the sensor and several charged layers.

a capacitor model consisting of $N+1$ charged plates surrounded by media of different dielectric constants (Fig. 4.1). The sensor is represented by the first two layers. σ_0 is the space charge in the silicon layer and σ_1 is the surface charge of the silicon oxide, which in a first approximation is assumed to be constant. By σ_i $(1 < i < N)$ we denote the charge of the additional layers. σ_N is the charge of the electrical double layer, which can be treated as a parallel plate capacitor with a spacing of $\kappa^{-1} = d_{\mathrm{N}}$ according to Eq. (2.7). The dielectric constants are ε_i, the distance between the plates are denoted by d_i. The total voltage U_{tot} between the first plate with surface charge σ_0 and the last plate with surface charge σ_N is fix. It is determined by the applied reference voltage U_{ref}, as well as by the potential drop over the reference electrode and at the metal contacts. The potential at the first layer is set to zero. Thus the voltage drop U_1 between the first and the second plate corresponds to the potential at the sensor surface ψ_{S}, which is the parameter we want to determine. U_1 can be calculated according to Appendix A. It is found that

$$U_1 = \psi_{\mathrm{S}} \;=\; \frac{d_1}{\varepsilon_1}\frac{1}{\sum_{i=1}^{N}\frac{d_i}{\varepsilon_i}}\left(U_{\mathrm{tot}} - \sum_{i=1}^{N}\frac{d_i}{\varepsilon_i}\sum_{j=1}^{i-1}\sigma_j\right). \tag{4.1}$$

To simplify matters, this result can be rewritten in terms of surface normalized capacitances $C_i = \frac{\varepsilon_i}{d_i}$

$$\psi_{\mathrm{S}} = \frac{1}{C_1}\frac{1}{\sum_{i=1}^{N}\frac{1}{C_i}}\left(U_{\mathrm{tot}} - \sum_{i=1}^{N}\frac{1}{C_i}\sum_{j=1}^{i-1}\sigma_j\right). \tag{4.2}$$

Here C_1 is the capacitance of the sensor device and C_N is the capacitance of the electrical double layer. Eq. (4.2) differs from the well known expression obtained for N simple

capacitors in series by the term $-\sum_{i=1}^{N} \frac{1}{C_i} \sum_{j=1}^{i-1} \sigma_j$. This additional term accounts for the fix charges σ_i determined by the surface charge of the sensor and the charge of the additional layers lacking in the case of a simple serial connection of capacitors.

4.1.2 Capacitor Model for One Charged Layer Including Screening

The model described in the previous section constitutes the most simple case, where charged layers of surface charges σ_i with certain dielectric constants ε_i are adsorbed to the sensor device. However, between the layers no screening is assumed. The total charge of the system, which is made up by the semiconductor charge, the silicon oxide surface charge and the charges of the adsorbed layers, is screened only in the electrolyte solution as described by a parallel plate capacitor with a spacing of $\kappa^{-1} = d_{\mathrm{N}}$. For example, such a system could consist of a silanized sensor chip functionalized by a lipid monolayer containing charged lipids as has been described in Ref. [54]. In this case, no mobile ions are assumed to be present within the lipid monolayer and the silane, so the charge of the lipids is not screened within the lipid and silane layers. However, for most systems under investigation, screening effects will not only play a role in the electrolyte solution, but also within the layers of molecules bound to the sensor surface. In the following, we consider a system that consists of the sensor plus one charged layer. In between the sensor and the additional charge, screening by mobile ions can occur. This can be pictured as one charged plate at a certain distance d from the sensor surface. The potential in the silicon/silicon oxide structure is assumed to be linear. It is determined by the capacitance per area of the device $C_{\mathrm{S}} = \frac{\varepsilon_1}{d_1}$ which is given by the effective dielectric constant ε_1 and the thickness d_1. The charge of the silicon oxide surface is given by σ_1. If we assume that the Debye-Hückel approximation is valid, the Debye-Hückel equation must be solved in between the sensor surface and the charged layer. As there are no volume charges other than mobile ions (all fix charges are assumed to be surface charges), the Debye Hückel equation reads

$$\frac{\mathrm{d}^2}{\mathrm{d}x^2}\psi\left(x\right) - \kappa^2 \psi\left(x\right) = 0. \tag{4.3}$$

The screening length in between the sensor surface and the charged layer is assumed to be κ^{-1} and the dielectric constant is ε. The diffuse electrical double layer in the electrolyte is described by the dielectric constant for water ε_{w} and the screening length κ_0^{-1} which is equal to the effective double layer thickness d_L. The potential within the electrolyte is described by a plate capacitor with the Debye capacitance per area $C_{\mathrm{D}} = \varepsilon_{\mathrm{w}}\kappa_0$. A sketch of the described system is given in Fig. 4.2. The surface charges σ_0 and σ_L represent the space charges within the semiconductor and the electrical double layer of the electrolyte,

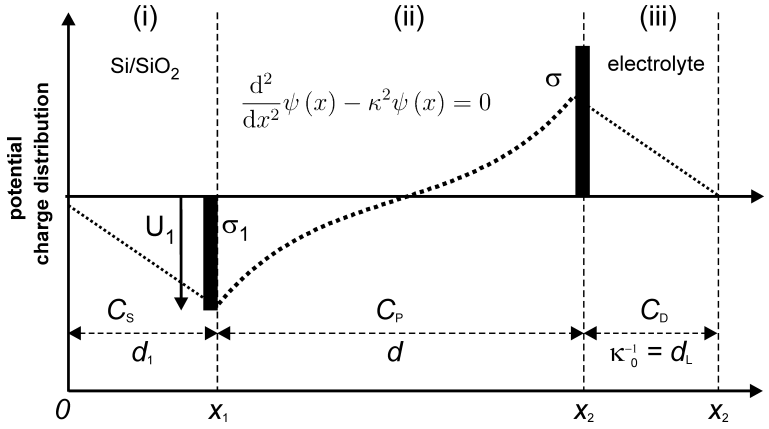

Figure 4.2: Sketch of the system consisting of the sensor plus one charged layer including screening.

respectively. The potential difference between the bulk semiconductor and the bulk electrolyte is U_{tot}. The potential within the three domains (i) - silicon/silicon oxide, (ii) - between the sensor surface and the charged layer and (iii) - electrical double layer is given by

$$\psi_{(\mathrm{i})}(x) = A'x + A, \tag{4.4}$$

$$\psi_{(\mathrm{ii})}(x) = C\exp(-\kappa x) + D\exp(\kappa x), \tag{4.5}$$

$$\psi_{(\mathrm{iii})}(x) = B'x + B. \tag{4.6}$$

We apply the following boundary conditions

$$\psi_{(\mathrm{i})}(0) = 0, \qquad \psi'_{(\mathrm{i})}(0) = -\frac{\sigma_0}{\varepsilon_1}, \tag{4.7}$$

$$\psi_{(\mathrm{iii})}(x_L) = U_{\mathrm{tot}}, \qquad \psi'_{(\mathrm{iii})}(x_L) = \frac{\sigma_L}{\varepsilon_{\mathrm{w}}}, \tag{4.8}$$

$$\psi_{(\mathrm{ii})}(x_1) - \psi_{(\mathrm{i})}(x_1) = 0, \qquad \varepsilon\psi'_{(\mathrm{ii})}(x_1) - \varepsilon_1\psi'_{(\mathrm{i})}(x_1) = -\sigma_1, \tag{4.9}$$

$$\psi_{(\mathrm{iii})}(x_2) - \psi_{(\mathrm{ii})}(x_2) = 0, \qquad \varepsilon_{\mathrm{w}}\psi'_{(\mathrm{iii})}(x_2) - \varepsilon\psi'_{(\mathrm{ii})}(x_2) = -\sigma, \tag{4.10}$$

with

$$x_1 = d_1, \tag{4.11}$$

$$x_2 = d_1 + d, \tag{4.12}$$

$$x_L = d_1 + d + d_L. \tag{4.13}$$

These conditions allow us to calculate the potential $\psi_S = \psi(x_1) = U_1$ which determines the sheet resistance of the device (Appendix B)

$$U_1 = -\frac{d_1}{\varepsilon_1}\frac{1}{\varepsilon\kappa}\frac{2U_{tot} + 2\sigma\frac{d_L}{\varepsilon_L} + \sigma_1\left[\exp(-\kappa d)\left(\frac{d_L}{\varepsilon_L} - \frac{1}{\varepsilon\kappa}\right) + \exp(\kappa d)\left(\frac{d_L}{\varepsilon_L} + \frac{1}{\varepsilon\kappa}\right)\right]}{\left(\frac{d_L}{\varepsilon_L} - \frac{1}{\varepsilon\kappa}\right)\exp(-\kappa d)\left(\frac{x_1}{\varepsilon_1} - \frac{1}{\varepsilon\kappa}\right) - \left(\frac{d_L}{\varepsilon_L} + \frac{1}{\varepsilon\kappa}\right)\exp(\kappa d)\left(\frac{x_1}{\varepsilon_1} + \frac{1}{\varepsilon\kappa}\right)}. \quad (4.14)$$

This can be rewritten in terms of capacitances with the Debye capacitance of the adsorbed layer $C_P = \varepsilon\kappa$

$$U_1 = \frac{2U_{tot} + 2\sigma\frac{1}{C_D} + \sigma_1\left[\exp(\kappa d)\left(\frac{1}{C_D} + \frac{1}{C_P}\right) + \exp(-\kappa d)\left(\frac{1}{C_D} - \frac{1}{C_P}\right)\right]}{\left(\frac{1}{C_D} + \frac{1}{C_P}\right)(C_P + C_S)\exp(\kappa d) - \left(\frac{1}{C_D} - \frac{1}{C_P}\right)(C_P - C_S)\exp(-\kappa d)}. \quad (4.15)$$

For $\frac{1}{C_D} = \frac{1}{C_P}$ and $U_{tot} = 0$ this results in

$$\begin{aligned} U_1 &= \frac{2\sigma\frac{1}{C_D} + \sigma_1\exp(\kappa d)\left(\frac{2}{C_D}\right)}{\left(\frac{2}{C_D}\right)(C_D + C_S)\exp(\kappa d)} \\ &= \frac{\sigma}{(C_D + C_S)\exp(\kappa d)} + \frac{\sigma_1}{(C_D + C_S)} \\ &= \frac{\sigma}{(C_D + C_S)}\exp(-\kappa d) + \frac{\sigma_1}{(C_D + C_S)}. \end{aligned} \quad (4.16)$$

This implicates that the adsorption of a surface charge σ at a distance d from the sensor surface will change the measured surface potential by

$$\Delta U_1 = U_1(\sigma) - U_1(\sigma = 0) = \frac{\sigma}{(C_D + C_S)}\exp(-\kappa d). \quad (4.17)$$

Thus the sensor signal caused by the adsorption of a charge decreases exponentially with increasing distance form the sensor surface.

4.1.3 Capacitor Model for the Description of Polyelectrolyte Multilayers

Polyelectrolyte multilayers are assumed to be composed of layers carrying alternate charges that are equal in magnitude. First, we consider a model for polyelectrolyte multilayers where the charges are situated on plates with the surface charge density $\pm\sigma$. The plates are separated by a distance d as shown in Fig. 4.3(a). This is comparable to the situation depicted in Fig. 4.2 where we have considered one charged layer at a distance d from the device. However, for multilayers consisting of N alternately charged layers we have to find

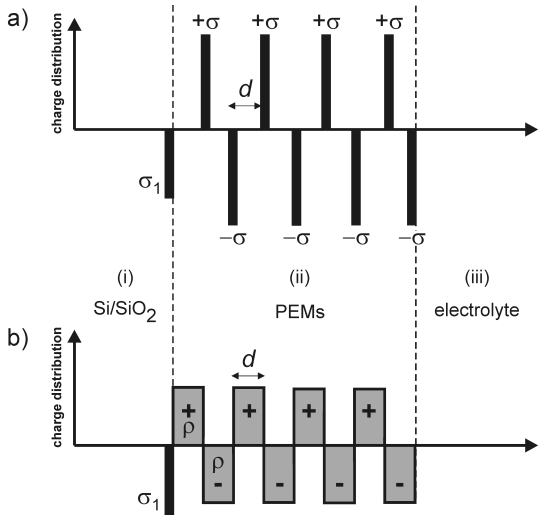

Figure 4.3: Polyelectrolyte multilayers modeled as surface charges (a) and volume charges (b). The surface charges are separated by a distance d; volume charges have a thickness of d.

the solutions in the $N+2$ domains (i), $(\text{ii})_1$, ..., $(\text{ii})_N$ und (iii)

$$\psi_{(\text{i})}(x) = A'x + A, \tag{4.18}$$

$$\psi_{(\text{ii})_n}(x) = C_n \exp(-\kappa x) + D_n \exp(\kappa x), \qquad n = 1, \ldots, N \tag{4.19}$$

$$\psi_{(\text{iii})}(x) = B'x + B. \tag{4.20}$$

The boundary conditions are given by

$$\psi_{(\text{i})}(0) = 0, \qquad \psi'_{(\text{i})}(0) = -\frac{\sigma_0}{\varepsilon_1}, \tag{4.21}$$

$$\psi_{(\text{iii})}(x_L) = U_{\text{tot}}, \qquad \psi'_{(\text{iii})}(x_L) = \frac{\sigma_L}{\varepsilon_L} \tag{4.22}$$

$$\psi_{(\text{ii})_1}(x_1) - \psi_{(\text{i})}(x_1) = 0, \qquad \varepsilon\psi'_{(\text{ii})_1}(x_1) - \varepsilon_1\psi'_{(\text{i})}(x_1) = -\sigma_1, \tag{4.23}$$

$$\psi_{(\text{iii})}(x_{N+1}) - \psi_{(\text{ii})_N}(x_{N+1}) = 0, \qquad \varepsilon_L\psi'_{(\text{iii})}(x_{N+1}) - \varepsilon\psi'_{(\text{ii})_N}(x_{N+1}) = (-1)^N \sigma, \tag{4.24}$$

$$\psi_{(\text{ii})_n}(x_n) - \psi_{(\text{ii})_{n-1}}(x_n) = 0, \qquad \varepsilon\psi'_{(\text{ii})_n}(x_n) - \varepsilon\psi'_{(\text{ii})_{n-1}}(x_n) = (-1)^{n-1} \sigma, \tag{4.25}$$

$$n = 2, \ldots, N$$

with

$$x_0 = 0, \tag{4.26}$$

$$x_n = d_1 + (n-1)\,d, \qquad n = 1, \ldots, N+1, \tag{4.27}$$

$$x_L = d_1 + Nd + d_L. \tag{4.28}$$

These conditions allow us to calculate the potential $\psi_S = \psi(x_1) = U_1$ which determines the sheet resistance of the device (Appendix C).

$$U_1 = \frac{d_1}{\varepsilon_1} \frac{\left(s_1 e^{-\kappa x_{N+1}} \left(-\frac{d_L}{\varepsilon_L} + \frac{1}{\kappa\varepsilon}\right) + s_2 e^{\kappa x_{N+1}} \left(\frac{d_L}{\varepsilon_L} + \frac{1}{\kappa\varepsilon}\right)\right)}{\left(\frac{1}{\kappa\varepsilon} - \frac{x_1}{\varepsilon_1}\right)\left(\frac{1}{\kappa\varepsilon} - \frac{d_L}{\varepsilon_L}\right) e^{-\kappa N d} - \left(\frac{1}{\kappa\varepsilon} + \frac{x_1}{\varepsilon_1}\right)\left(\frac{1}{\kappa\varepsilon} + \frac{d_L}{\varepsilon_L}\right) e^{\kappa N d}} \tag{4.29}$$

with

$$\begin{pmatrix} s_1 \\ s_2 \end{pmatrix} = \begin{pmatrix} \frac{1}{\kappa\varepsilon}\sigma_1 e^{\kappa x_1} - \frac{(-1)^N}{\kappa\varepsilon}\sigma e^{\kappa x_{N+1}} - e^{\kappa x_{N+1}} U_{\text{tot}} \\ -\frac{1}{\kappa\varepsilon}\sigma_1 e^{-\kappa x_1} + \frac{(-1)^N}{\kappa\varepsilon}\sigma e^{-\kappa x_{N+1}} - e^{-\kappa x_{N+1}} U_{\text{tot}} \end{pmatrix} + \frac{1}{\kappa}\frac{\sigma}{\varepsilon} \begin{pmatrix} e^{\kappa d_1} \frac{e^{\kappa d} + (-1)^N e^{\kappa d N}}{1 + e^{\kappa d}} \\ -e^{-\kappa d_1} \frac{e^{-\kappa d} + (-1)^N e^{-\kappa d N}}{1 + e^{-\kappa d}} \end{pmatrix}. \tag{4.30}$$

For $N = 1$ the result simplifies to

$$U_1 = -\frac{d_1}{\varepsilon_1}\frac{1}{\varepsilon\kappa} \frac{2U_{\text{tot}} + 2\sigma\frac{d_L}{\varepsilon_L} + \sigma_1\left[e^{-\kappa d}\left(\frac{d_L}{\varepsilon_L} - \frac{1}{\varepsilon\kappa}\right) + e^{\kappa d}\left(\frac{d_L}{\varepsilon_L} + \frac{1}{\varepsilon\kappa}\right)\right]}{\left(\frac{d_L}{\varepsilon_L} - \frac{1}{\varepsilon\kappa}\right) e^{-\kappa d}\left(\frac{x_1}{\varepsilon_1} - \frac{1}{\varepsilon\kappa}\right) - \left(\frac{d_L}{\varepsilon_L} + \frac{1}{\varepsilon\kappa}\right) e^{\kappa d}\left(\frac{x_1}{\varepsilon_1} + \frac{1}{\varepsilon\kappa}\right)} \tag{4.31}$$

which is exactly what we have obtained in the previous section for one charged layer (Eq. (4.14)).

In a more realistic description of polyelectrolyte multilayers, the charges are assumed to be homogeneously distributed in layers with a volume charge density $\rho = \pm\frac{\sigma}{d}$ as depicted in Fig. 4.3(b). To obtain an expression for the potential $\psi_S = \psi(x_1) = U_1$ we can make use of the result obtained for charged plates (Appendix D). In the PEMs, the Debye-Hückel (DH) equation

$$\frac{\mathrm{d}^2}{\mathrm{d}x^2}\psi(x) - \kappa^2\psi(x) = -\frac{1}{\varepsilon}\rho(x) \tag{4.32}$$

is solved for each single polyelectrolyte layer with $\rho(x) = \pm\frac{\sigma}{d}$. The screening length inside the PEMs is assumed to be κ^{-1} and the dielectric constant is ε. The potential ψ within

the $N+2$ domains (i), (ii)$_1$, ..., (ii)$_N$, and (iii) is given by

$$\psi_{(\mathrm{i})}(x) = A'x + A, \tag{4.33}$$

$$\psi_{(\mathrm{ii})_n}(x) = C_n \exp(-\kappa x) + D_n \exp(\kappa x) + \psi_n(x), \qquad n = 1, \ldots, N \tag{4.34}$$

$$\psi_{(\mathrm{iii})}(x) = B'x + B, \tag{4.35}$$

where $C_n \exp(-\kappa x) + D_n \exp(\kappa x)$ is the general solution of the homogeneous DH equation and $\psi_n(x)$ is a particular solution of the inhomogeneous DH equation for $\rho(x) = -\frac{\sigma}{d}(-1)^n$. We apply the following boundary conditions

$$\psi_{(\mathrm{i})}(0) = 0, \qquad \psi'_{(\mathrm{i})}(0) = -\frac{\sigma_0}{\varepsilon_1}, \tag{4.36}$$

$$\psi_{(\mathrm{iii})}(x_L) = U_{\mathrm{tot}}, \qquad \psi'_{(\mathrm{iii})}(x_L) = \frac{\sigma_L}{\varepsilon_{\mathrm{w}}}, \tag{4.37}$$

$$\psi_{(\mathrm{ii})_1}(x_1) - \psi_{(\mathrm{i})}(x_1) = 0, \qquad \varepsilon\psi'_{(\mathrm{ii})_1}(x_1) - \varepsilon_1\psi'_{(\mathrm{i})}(x_1) = -\sigma_1, \tag{4.38}$$

$$\psi_{(\mathrm{iii})}(x_{N+1}) - \psi_{(\mathrm{ii})_N}(x_{N+1}) = 0, \qquad \varepsilon_{\mathrm{w}}\psi'_{(\mathrm{iii})}(x_{N+1}) - \varepsilon\psi'_{(\mathrm{ii})_N}(x_{N+1}) = 0, \tag{4.39}$$

$$\psi_{(\mathrm{ii})_n}(x_n) - \psi_{(\mathrm{ii})_{n-1}}(x_n) = 0, \qquad \varepsilon\psi'_{(\mathrm{ii})_n}(x_n) - \varepsilon\psi'_{(\mathrm{ii})_{n-1}}(x_n) = 0, \tag{4.40}$$

$$n = 2, \ldots, N$$

with

$$x_n = d_1 + (n-1)d, \qquad n = 1, \ldots, N+1, \tag{4.41}$$

$$x_L = d_1 + Nd + d_L. \tag{4.42}$$

These conditions allow us to calculate $U_1(N)$ (Appendix D). With the Debye capacitance per area $C_{\mathrm{P}} = \varepsilon\kappa$ within the polyelectrolyte medium we can write U_1 as

$$U_1(N) = \frac{(\sigma_1 + \sigma_{\mathrm{eff}})\left[\frac{1}{C_{\mathrm{P}}}\sinh(\kappa N d) + \frac{1}{C_{\mathrm{D}}}\cosh(\kappa N d)\right] + \left(U_{\mathrm{tot}} - \frac{1}{C_{\mathrm{D}}}(-1)^N\sigma_{\mathrm{eff}}\right)}{(C_{\mathrm{S}}/C_{\mathrm{P}} + C_{\mathrm{P}}/C_{\mathrm{D}})\sinh(\kappa N d) + (1 + C_{\mathrm{S}}/C_{\mathrm{D}})\cosh(\kappa N d)} \tag{4.43}$$

with the effective polyelectrolyte surface charge

$$\sigma_{\mathrm{eff}} = \frac{1}{\kappa d}\left[\frac{1 - \exp(-\kappa d)}{1 + \exp(-\kappa d)}\right]\sigma. \tag{4.44}$$

Note that the DH approximation used in the present theoretical model is valid for relatively small values of the electrostatic potential. At room temperature, for symmetrical monovalent electrolytes these are potentials below 50 mV. In Ref. [50] it is demonstrated

that under these condition the error does not exceed 20% even for potentials as high as 100 mV. In general, a full non-linear Poisson-Boltzmann analysis would be necessary, which, however, is not analytically solvable for the present system. The main advantage of the DH approach lies in obtaining a simple analytical expression for the sensor device functionalized by PEMs enabling a direct comparison with the experimental data.

4.2 Detection and Characterization of Polyelectrolyte Multilayers

The structural parameters of polyelectrolyte multilayers such as the layer thickness or surface coverage have been studied intensively for more than ten years [58, 59, 15]. In particular, techniques such as X-ray and neutron reflectivity have been employed for the characterization of the polymer films. Recently, attention has been directed towards the internal properties of the multilayer assembly such as water or ion content. The buildup of PEMs can be observed by field effect based sensing devices such a the SOI sensor used here, providing an insight into their electrostatic properties. At the same time, due to their well-defined architecture, the deposition of PEMs allows for the adsorption of defined charges at defined distances, which proves useful for the investigation of the detection mechanism of field effect devices. In the following sections, our results concerning the detection of PEMs are presented and analyzed using the capacitor model introduced in the previous section. The buildup of PEMs consisting of different polyelectrolytes was monitored and the resulting shifts of the surface potential were extracted from the data. Thereby, we have observed a characteristic signal decrease for different conditions of the deposition resulting from screening by mobile ions inside the polyelectrolyte film. For a quantitative analysis of these screening effects, the thickness of the polyelectrolyte films must be known. Here, we have determined the multilayer thickness by ellipsometry and X-ray reflectivity. From the screening length inside the polymer films, we were able to derive the dielectric properties and the concentration of mobile ions in the films. Furthermore, we studied the concentration of protons and their permeability in the films by measuring the pH response of the sensor during PEMs deposition. For multilayer buildup, a certain minimal charge density of the polyelectrolytes is required. Polyelectrolytes with a variable charge density have been employed for the investigation of this minimal charge density and of charge compensation during multilayer buildup.

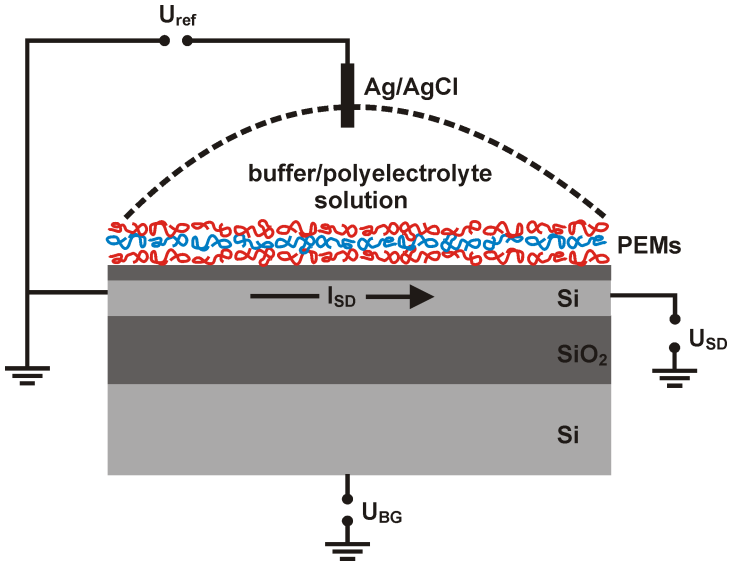

Figure 4.4: Polyelectrolyte multilayers are adsorbed directly at the sensor surface. First, the positively charged polymer is injected and will bind to the negatively charged silicon oxide surface. After a washing step the anionic polymer is injected forming a second layer. After another washing step, the adsorption cycle can be repeated.

4.2.1 Buildup of Polyelectrolyte Multilayers

The SOI based thin film resistor is suited to monitor in real time the buildup of polyelectrolyte multilayers as the sheet resistance of the field effect device is sensitive to variations of the potential ψ_S at the silicon oxide surface. The deposition of the differently charged polyelectrolytes results in defined potential shifts which can be analyzed quantitatively.

Experimental Procedure. For the deposition of polyelectrolyte layers, the respective polymer was directly dissolved at 5 mg/ml in the buffer solution. Buffer solutions were prepared using ultrapure water (Millipore, France) with a resistivity > 18 MΩcm. For all experiments, a 10 mM Tris buffer at pH 7.5 containing 50 or 500 mM NaCl was used. For the deposition of PEMs, the sensor was first equilibrated in the buffer solution. Next, a calibration measurement was performed as described in Section 3.3. Usually, the polyelectrolyte solutions were injected twice into the flow chamber to ensure full coverage of the sensor surface, starting with the positively charged polymer. After obtaining a stable sensor signal, the chamber was thoroughly rinsed with buffer solution. As soon as a stable signal was obtained, the next polyelectrolyte solution was injected and the procedure was repeated up to 20 times. The sheet resistance of the thin film resistor was monitored continuously during the multilayer deposition. A schematic view of the experimental setup and the adsorbed polyelectrolyte layers is given in Fig. 4.4.

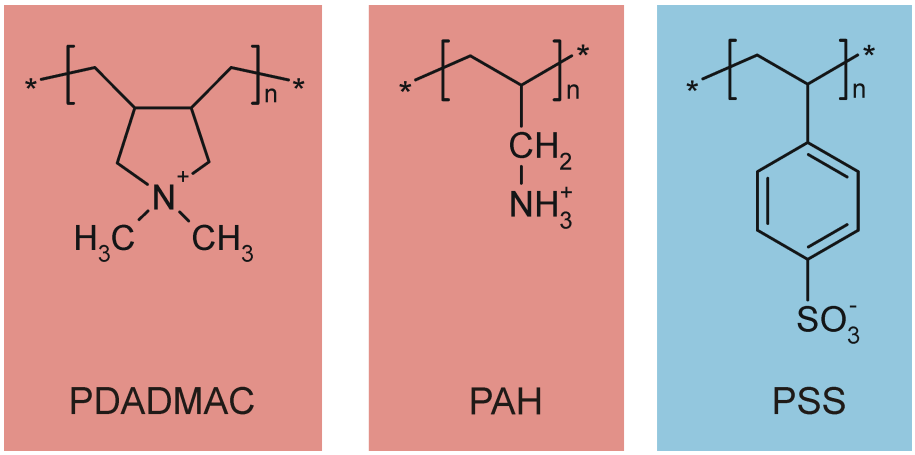

Figure 4.5: Chemical structures of the polyelectrolytes used for the deposition of PEMs. Poly(diallyl-dimethyl-ammoniumchloride), PDADMAC and poly(allylamine-hydrochloride), PAH are cationic polyelectrolytes, poly(styrene sulfonate), PSS is an anionic polyelectrolyte.

Polyelectrolyte Structures. Poly(diallyl-dimethyl-ammoniumchloride), PDADMAC, and poly(allylamine-hydrochloride), PAH, were used as cationic polyelectrolytes. In all experiments, poly(styrene sulfonate), PSS was used as anionic polyelectrolyte. PSS (MW 70,000) and PAH (MW 60,000) were purchased from Sigma-Aldrich. PDADMAC was provided by Werner Jaeger (Fraunhofer Institut für Angewandte Polymerforschung). The chemical structures of the polyelectrolytes are shown in Fig. 4.5. PDADMAC and PSS are strong polyelectrolytes, meaning that they are fully charged at any pH. PAH is a week polyelectrolyte. Its degree of protonation depends on the pH of the solution as well as on the local chemical environment. The pK value of the primary amine inside the polyelectrolyte film differs from its pK in solution and thus the actual degree of charge may vary with the type of polyelectrolyte film [60].

Deposition of Multilayers. In Fig. 4.6 the first two cycles of the deposition of PAH/PSS and PDADMAC/PSS multilayers from buffer solution containing 50 mM NaCl are shown. In both cases, we start with the blank, negatively charged silicon oxide surface of the sensor device. The adsorption of positively charged molecules will increase the surface potential. This leads to a decrease of the sheet resistance, which is observed in the measurement. In the case of PAH/PSS layers, there is a significant change in sheet resistance when the chamber is rinsed with buffer (also containing 50 mM NaCl) after the adsorption of PAH. This is caused by a change in the pH of the solution when the weak polyelectrolyte PAH is dissolved. The amine group will partially deprotonate, leading to a decrease of pH in the polyelectrolyte solution. The SOI sensor is sensitive to pH changes as explained in

Section 2.2.4 by the site binding model. A lower pH leads to a more positively charged surface decreasing the sheet resistance of the device. To get rid of such pH effects, the potential change between adjacent deposition steps $\Delta\psi_S$ was determined from the sheet resistance after the sensor was rinsed with buffer solution. In this manner, only values for the sheet resistance measured with the same buffer solution are compared. In the next step, the solution containing the negatively charged PSS can be injected into the flow chamber. This leads to the binding of negatively charged molecules to the surface. Thereby, the surface potential decreases again and the sheet resistance is increased. Next, the deposition cycle is completed by another rinse with buffer solution and can be repeated an arbitrary number of times.

Surface Potential Shifts. From this type of experiment we can extract the change in sheet resistance between adjacent deposition steps, which is caused by the adsorption of polyelectrolyte molecules. The corresponding change in potential $\Delta\psi$ can be calculated using the calibration data (Section 3.3). $\Delta\psi$ can be plotted against the number of deposition steps as demonstrated in Fig. 4.7. Here, the oscillations of the surface potential are shown for the deposition of PDADMAC/PSS layers from buffer solution containing 50 mM NaCl. However, it must be noted that only relative values are obtained as important parameters such as contact potential, number of surface sites or quality of the oxide are not accessible. The values are given relative to the potential of the blank silicon oxide surface. In contrast, electrokinetic studies such as streaming potential measurements can provide absolute values of the zeta potential (potential at the shear plane at some distance from the surface), which must be distinguished from the surface potential.

4.2.2 Screening in Polyelectrolyte Multilayers

Surface Potential and Zeta-Potential. The potential jumps observed with the SOI sensor during the deposition of polyelectrolyte multilayers decrease with the number of layers deposited. This is in contrast to electrokinetic studies such as the measurement of the streaming potential, where the potential steps remain constant over a large range of deposited layers. In these measurements, the zeta potential at a shear plane outside the outer Helmholtz plane is determined with respect to the outer solution bulk value. Thus in case of PEMs, the zeta potential is measured at the side where new layers are adsorbed, whereas field effect devices such as the SOI sensor measure the surface potential at the substrate/polyelectrolyte interface (Fig. 4.8(a)). Therefore, the latter are strongly dependent on screening effects within the polyelectrolyte films, which are not accessible by zeta potential measurements. A direct comparison of zeta-potential measurements with

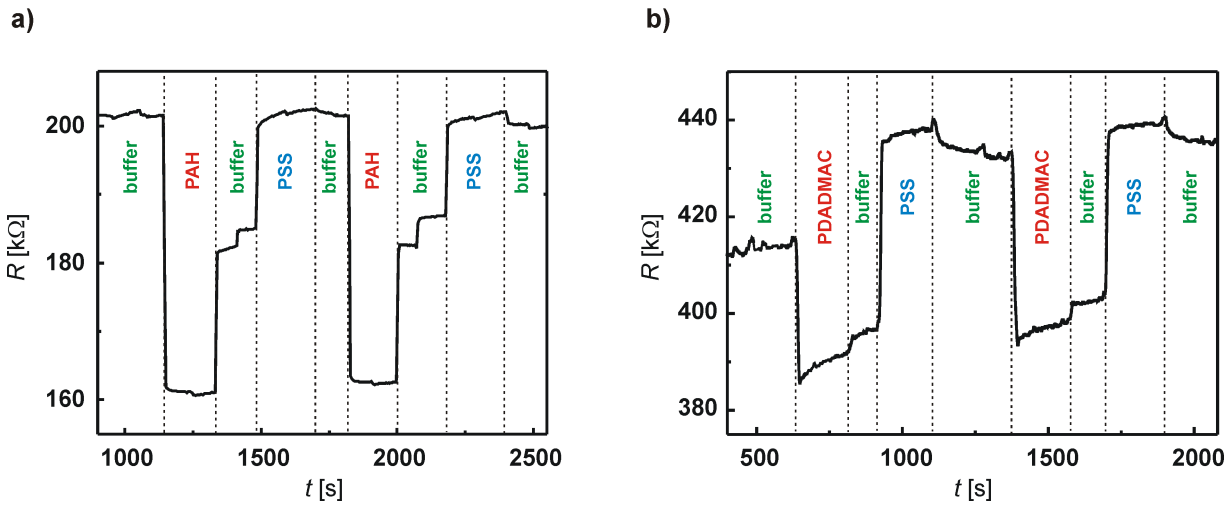

Figure 4.6: Deposition of PAH/PSS (a) and PDADMAC/PSS (b) multilayers. Two full deposition cycles are shown. First, the positively charged polyelectrolyte is adsorbed to the sensor surface decreasing the sheet resistance. After a buffer rinse, the negatively charged PSS is adsorbed, which increases the sheet resistance. A second buffer rinse completes the first deposition cycle and the procedure can be repeated.

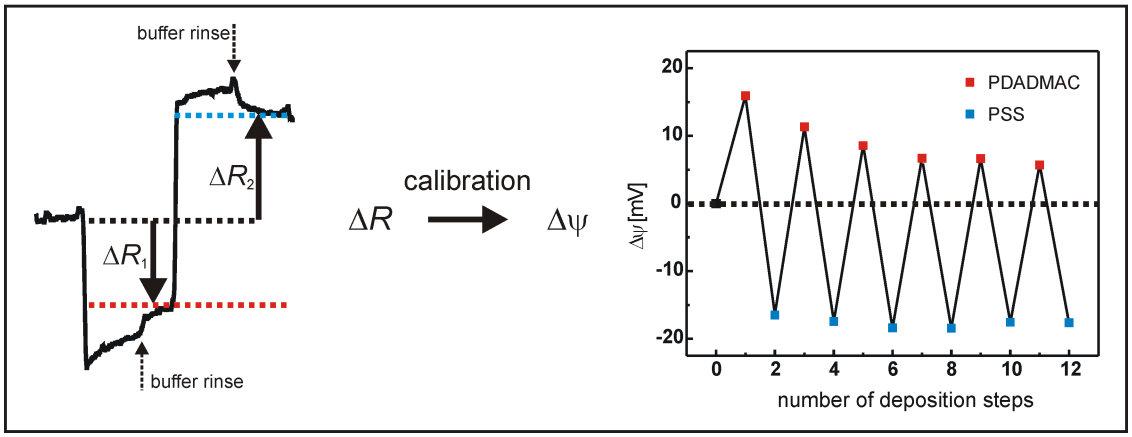

Figure 4.7: The change in sheet resistance ΔR between subsequent deposition steps is related to the corresponding change in surface potential $\Delta\psi$. Here, the deposition of PDADMAC/PSS layers from buffer containing 50 mM NaCl is shown. Only variations of the surface potential can be quantified and relative values are obtained. In the graph on the right, these values are given with respect to the potential of the blank sensor surface. The solid lines are a guide to the eye.

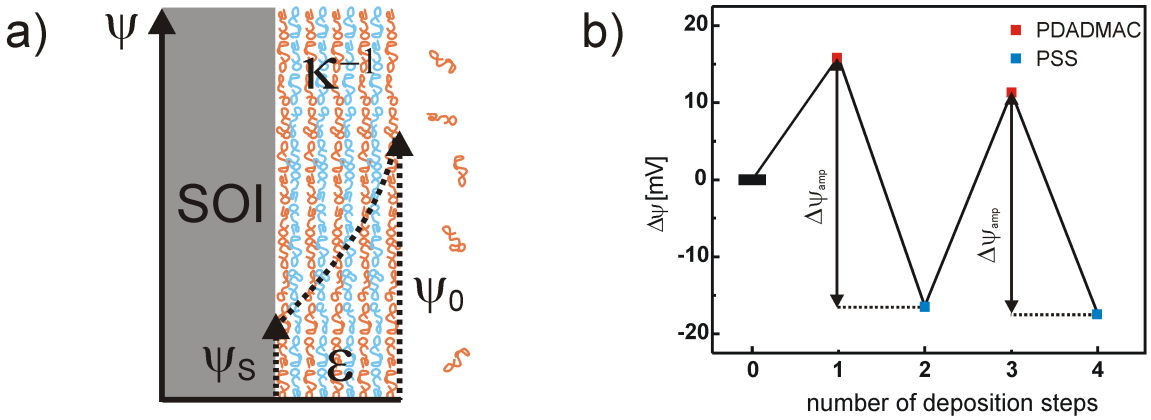

Figure 4.8: (a) Field effect devices such as the SOI sensor measure the surface potential ψ_s at the substrate/polyelectrolyte interface. Therefore, the signals obtained are strongly dependent on screening effects within the polyelectrolyte films. (b) The amplitude $\Delta\psi_{amp}$ of the potential oscillations is illustrated for the case of PDADMAC/PSS multilayers. The decrease of $\Delta\psi_{amp}$ can be used to visualize the signal decrease with increasing number of layers. The solid lines are a guide to the eye.

surface potential measurements is of extreme difficulty as different boundary conditions apply for either experiment. In the case of zeta-potential measurements, the boundary conditions for the solution of the Poisson-Boltzmann equation are given by the surface charge of the substrate and total charge neutrality. This leads immediately to alternating zeta-potentials independent of the number of layers assuming the same absolute charge densities for adjacent PE layers. In contrast, in our system the boundary conditions are given by a constant reference voltage. Combined measurements of surface potential and zeta-potential have shown that even for uncoated substrates variations of the surface potential and the zeta-potential can differ by an order of magnitude as the zeta-potential is measured outside the outer Helmholtz plane at a few angstroms from the surface [61].

Signal Decrease. Here, we make use of the signal decrease caused by the screening of polyelectrolyte charges by mobile ions to gain information on internal properties of the polyelectrolyte films. A suitable measure for the signal and hence the signal decrease upon polyelectrolyte adsorption is the amplitude $\Delta\psi_{amp}$ of the potential oscillations. As depicted in Fig. 4.8(b), $\Delta\psi_{amp}$ is the potential change between adjacent deposition steps of positively and negatively charged polymers. Here potential variations are not given with respect to the potential of the blank sensor surface but with respect to the previous polyelectrolyte layer. This allows us to be independent of long-term drift effects and clearly visualizes the observed signal decrease. Fig. 4.9 shows $\Delta\psi_{amp}$ plotted against the

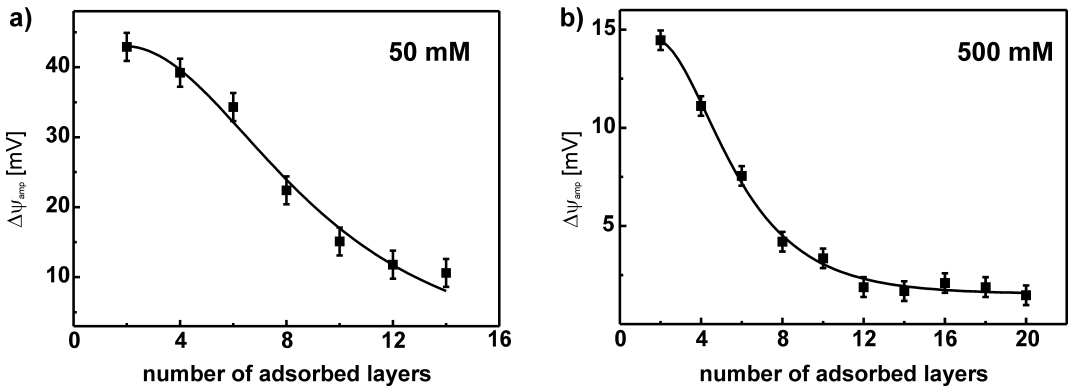

Figure 4.9: The potential change caused by the adsorption of charged polyelectrolyte layers on top of the sensor device is increasingly screened with increasing number of adsorbed layers. This signal decrease is shown in terms of $\Delta\psi_{\mathrm{amp}}$ for PAH/PSS multilayers for the deposition from buffer solutions containing 50 mM (a) and 500 mM (b) NaCl, respectively. The solid lines represent a fit by Eq. (4.51) as explained in Section 4.2.4.

number of adsorbed layers for PAH/PSS films. In a) the layers were adsorbed from a buffer solution containing 50 mM NaCl, whereas b) shows the adsorption from 500 mM NaCl. In terms of layer numbers, the decrease is faster in the case of 500 mM. At the same time, the decrease starts from a significantly lower value (14.5 ± 0.5 mV for 500 mM as compared to 42.9 ± 1.8 mV for 50 mM). However, from this alone it is not possible to draw a conclusion on the actual screening length inside the polyelectrolyte films, as the thickness of polyelectrolyte layers depends on the ionic strength of the solution used in the deposition process. Yet, the screening length in the buffer solution can be calculated from the known composition of the buffer. For the buffer containing 50 mM NaCl, a screening length of 1.3 nm is obtained, for the 500 mM buffer a screening length of 0.4 nm is obtained. If we assume that the same amount of charge is adsorbed for both buffers, the bulk screening lengths can explain the striking difference of the initial value for $\Delta\psi_{\mathrm{amp}}$. From Eq. (2.7) it follows for equal surface charges that

$$\kappa_{50\mathrm{mM}}\Delta\psi_{50\mathrm{mM}} = \kappa_{500\mathrm{mM}}\Delta\psi_{500\mathrm{mM}} \tag{4.45}$$

which is met rather well. As shown in Fig. 4.10 the signal decrease observed in the case of PDADMAC/PSS multilayers (buffer containing 50 mM NaCl) is considerably slower as compared to the decrease observed for PAH/PSS. Assuming that the thickness of PDADMAC/PSS layers is in the same order of magnitude as the thickness of PAH/PSS layers, screening inside these layers is much less pronounced.

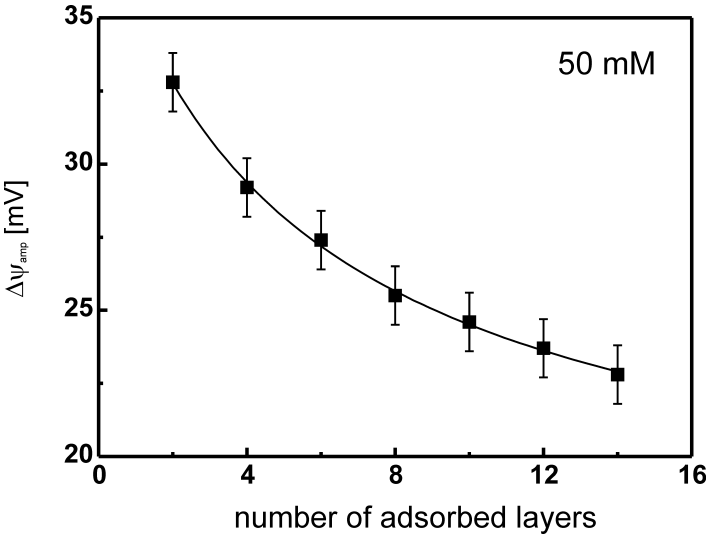

Figure 4.10: $\Delta\psi_{\text{amp}}$ is shown for PDADMAC/PSS multilayers for the deposition from 50 mM NaCl. The screening effect in these polyelectrolyte films is much less pronounced than in multilayers consisting of PAH/PSS assuming a similar layer thickness. The solid line represents a fit by Eq. (4.51) as explained in Section 4.2.4.

4.2.3 Determination of Multilayer Thickness by Ellipsometry and X-Ray Reflectivity

For a more detailed analysis of the signal decrease obtained for the different PEMs it is crucial to know the polyelectrolyte layer thickness. It is known that the thickness is depending not only on the type of polyelectrolyte and the ionic strength and pH of the solution used in the deposition process but also on the degree of hydration. Most literature values have been obtained with dried samples, partly at controlled humidity. A measurement performed in electrolyte solution will be suited best to obtain reliable values for the interpretation of screening data. X-ray reflectivity [62] as well as ellipsometry in buffer solution [56] have been employed to gain values for the thickness of PEMs under the conditions applied in the electric measurements.

Ellipsometry. Ellipsometry has been carried out using an Optrel Multiscope. Samples have been prepared by a dipping procedure without drying of the samples between the dipping steps. For this, silicon wafers with a thermal oxide of 150 nm were first cleaned by sonication in acetone and isopropanol. Next, the wafers were dipped into a buffer solution (10 mM Tris at pH 7.5 containing either 50 or 500 mM NaCl) for 3 min. After equilibration in buffer solution, the wafers were immediately dipped into 5 mg/ml PAH dissolved in the respective buffer solution. After 3 min the wafers were rinsed three times by immersion into fresh buffer solution for 1 min, respectively. Subsequently, the wafers were dipped into

5 mg/ml PSS solution dissolved in the respective buffer solution. After 3 min the wafers were rinsed again three times. The deposition cycle was repeated as often as needed. Part of the samples were briefly rinsed with water and dried in a nitrogen stream for dry measurements. The other samples were stored in the respective buffer solution and kept under buffer solution during the measurements. For multilayer deposition from 50 mM no significant difference of monolayer thickness between the dried layers (1.17 ± 0.04 nm) and the hydrated layers (1.26 ± 0.05 nm) was found. However, for the deposition from 500 mM a significant difference for the monolayer thickness between the dried layers (1.69 ± 0.17 nm) and the hydrated samples was found (2.16 ± 0.06 nm). The values for the monolayer thickness are summarized in Table 4.2.3.

X-Ray Reflectivity. X-ray reflectivity measurements at 19.0 keV were carried out at the Hamburger Synchrotronstrahlungslabor (Hasylab, beamline D4). A microfluidic chamber (Fig. 4.11) was used for the deposition of PEMs on a silicon wafer substrate. The deposition was carried out according to the protocol used for the electric measurements. Polyelectrolyte multilayers were found to show only negligible contrast in electron density as compared to water. Therefore, lipid bilayers were deposited on the PEMs to gain contrast. For this purpose, lipid stock solutions of 1,2-dioleoyl-sn-glycero-3-phosphatidylcholine (DOPC, neutral) and 1,2-dioleoyl-sn-glycero-3-phosphatidyl-L-serine (DOPS, negative net charge) were partitioned into desired quantities and dried under nitrogen flow, followed by 24 hours in an evacuated exsiccator. Multilamellar vesicle suspensions (concentration 1 mg/ml) were obtained by hydration with deionized pure water. Sonication of these suspensions gave small unilamellar vesicles (SUVs). The fresh SUV solution was injected into the microchannel and incubated at room temperature for two hours, allowing the vesicles to adsorb on the top polyelectrolyte layer. The microchannel was subsequently rinsed with buffer solution. Due to osmotic pressure between the water-filled vesicles and the buffer environment, SUVs tend to deform and to rupture, giving lipid bilayer disks on the substrate. Such disks subsequently form continuous bilayers on the substrate. PAH/PSS multilayers were deposited from buffer solution containing 50 mM NaCl. Fig. 4.12 shows the reflectivity of a DOPS membrane supported by 7 monolayers, and the reflectivity of a DOPC membrane supported by 13 monolayers. The corresponding electron density profile can be extracted from a fit of the reflectivity (Fig. 4.13). The electron density profile can be correlated to the structure of the PEMs/lipid bilayer system. The signature of the lipid membrane is dominated by the electron density of the hydrocarbon chains, which are the only hydrophobic components in the system and therefore do not show swelling in the presence of water molecules. An average monolayer thickness of 1.10 ± 0.08 nm is obtained, which is in good agreement with ellipsometry data (Table 4.2.3). In the follow-

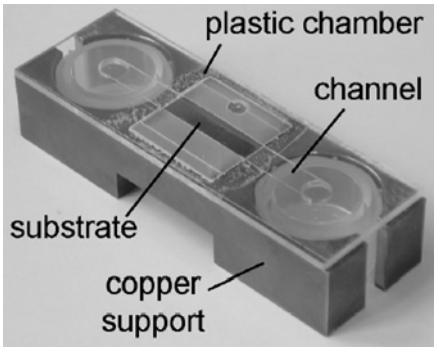

Figure 4.11: Microfluidic chamber as used in the X-ray reflectivity experiments for the determination of the multilayer thickness.

ing, the values obtained from ellipsometry of the hydrated samples are used for further analysis.

Method	**Thickness [nm] (50 mM)**	**Thickness [nm] (500 mM)**
ellipsometry dry	1.17 ± 0.04	1.69 ± 0.17
ellipsometry in buffer	1.26 ± 0.05	2.16 ± 0.06
X-ray reflectivity in buffer	1.10 ± 0.08	not measured

Table 4.1: Thickness of a polyelectrolyte monolayer as measured by ellipsometry and X-ray reflectivity for the deposition of PEMs from 50 mM and 500 mM NaCl.

4.2.4 Quantitative Analysis of Multilayer Deposition

Charge Distribution. Up to now we have assumed that the multilayer charges are situated in well-defined layers which do not intermix in the course of the deposition process. Yet, in experiments it has been found that adjacent oppositely charged polyelectrolyte layers intermix up to a certain degree leading to a charge distribution that differs from the one assumed in the derivation of our capacitor model [13, 19]. We consider two extreme cases of the charge distribution, which are depicted schematically in Fig. 4.14. In case (a) the layers are well-ordered corresponding to the charge distribution assumed in the capacitor model. However, in (b) charges are totally intermixed leaving the interior of the multilayer film neutral. An overlap of charges as shown in Fig. 4.15 will lead to a neutral multilayer film where the only charges that remain are located at the sensor surface and at the PEMs/electrolyte interface. The amount of charge that remains depends on the degree of overlap. In the next step, we want to derive an expression analogous to

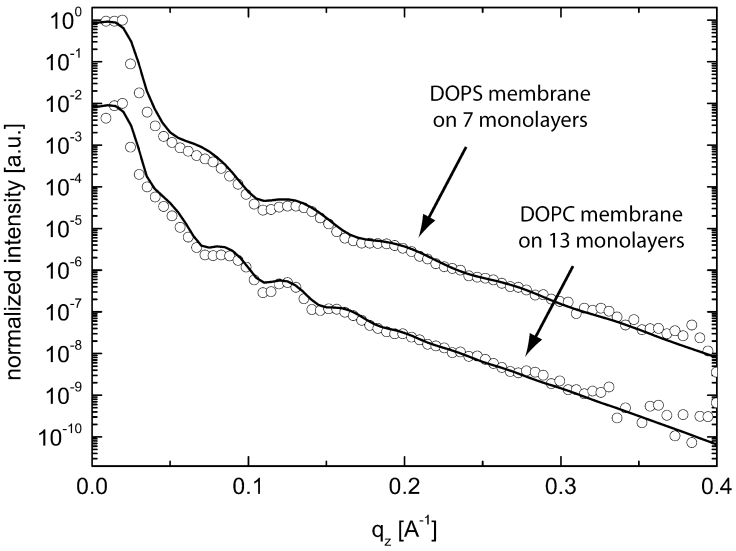

Figure 4.12: Reflectivity of a DOPS membrane on 7 monolayers of PAH/PSS and of a DOPC-membrane on 13 monolayers of PAH/PSS. The scans are shifted for clarity.

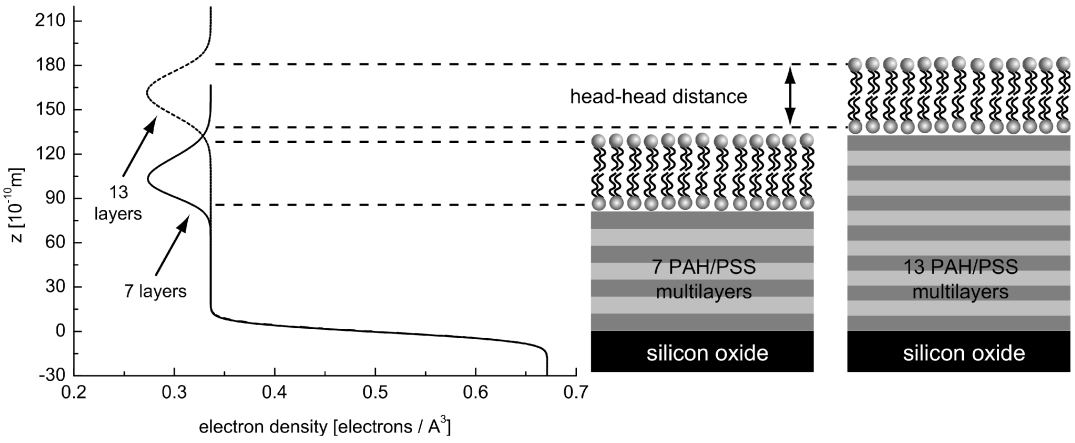

Figure 4.13: Electron density profiles for the data in Fig. 4.12. The dominant contrast contribution to the reflectivity signal results from the water-free chain region of the floating membrane.

Eq. (4.43) assuming that the charges completely neutralize each other inside the multilayers. Directly at the sensor surface there will be the surface charge $\sigma' = \frac{\sigma}{2}$ caused by the cationic polyelectrolyte. For even numbers of layers N, the surface charge is $-\sigma'$ at a distance of Nd, whereas for odd numbers the surface charge is σ'. This corresponds to the situation of a charged plate at the distance of Nd from the sensor surface. So we can immediately make use of Eq. (4.14)

$$U_1 = \frac{1}{\kappa\varepsilon}\frac{d_1}{\varepsilon_1}\frac{\sigma_1\left[\left(\frac{1}{\varepsilon\kappa}-\frac{d_L}{\varepsilon_L}\right)e^{-\kappa d}-\left(\frac{1}{\varepsilon\kappa}+\frac{d_L}{\varepsilon_L}\right)e^{\kappa d}\right]-2\left(U_{\text{tot}}+\frac{d_L}{\varepsilon_L}\sigma\right)}{\left(\frac{1}{\varepsilon\kappa}-\frac{d_L}{\varepsilon_L}\right)\left(\frac{1}{\varepsilon\kappa}-\frac{d_1}{\varepsilon_1}\right)e^{-\kappa d}-\left(\frac{1}{\varepsilon\kappa}+\frac{d_L}{\varepsilon_L}\right)\left(\frac{1}{\varepsilon\kappa}+\frac{d_1}{\varepsilon_1}\right)e^{\kappa d}}. \tag{4.46}$$

To describe the situation illustrated above, we have to modify this equation by adding σ' to the surface charge of the silicon oxide σ_1. For even numbers of layers N we have to account for the surface charge $-\sigma'$ at the PEMs/electrolyte interface:

$$U_1 = \frac{1}{\kappa\varepsilon}\frac{d_1}{\varepsilon_1}\frac{(\sigma_1+\sigma')\left[\left(\frac{1}{\varepsilon\kappa}-\frac{d_L}{\varepsilon_L}\right)e^{-\kappa Nd}-\left(\frac{1}{\varepsilon\kappa}+\frac{d_L}{\varepsilon_L}\right)e^{\kappa Nd}\right]-2\left(U_{\text{tot}}-\frac{d_L}{\varepsilon_L}\sigma'\right)}{\left(\frac{1}{\varepsilon\kappa}-\frac{d_L}{\varepsilon_L}\right)\left(\frac{1}{\varepsilon\kappa}-\frac{d_1}{\varepsilon_1}\right)e^{-\kappa Nd}-\left(\frac{1}{\varepsilon\kappa}+\frac{d_L}{\varepsilon_L}\right)\left(\frac{1}{\varepsilon\kappa}+\frac{d_1}{\varepsilon_1}\right)e^{\kappa Nd}}. \tag{4.47}$$

For odd numbers we have to account for the surface charge $+\sigma'$ at the PEMs/electrolyte interface:

$$U_1 = \frac{1}{\kappa\varepsilon}\frac{d_1}{\varepsilon_1}\frac{(\sigma_1+\sigma')\left[\left(\frac{1}{\varepsilon\kappa}-\frac{d_L}{\varepsilon_L}\right)e^{-\kappa Nd}-\left(\frac{1}{\varepsilon\kappa}+\frac{d_L}{\varepsilon_L}\right)e^{\kappa Nd}\right]-2\left(U_{\text{tot}}+\frac{d_L}{\varepsilon_L}\sigma'\right)}{\left(\frac{1}{\varepsilon\kappa}-\frac{d_L}{\varepsilon_L}\right)\left(\frac{1}{\varepsilon\kappa}-\frac{d_1}{\varepsilon_1}\right)e^{-\kappa Nd}-\left(\frac{1}{\varepsilon\kappa}+\frac{d_L}{\varepsilon_L}\right)\left(\frac{1}{\varepsilon\kappa}+\frac{d_1}{\varepsilon_1}\right)e^{\kappa Nd}}. \tag{4.48}$$

For arbitrary numbers we combine these equations and obtain

$$U_1 = \frac{1}{\kappa\varepsilon}\frac{d_1}{\varepsilon_1}\frac{(\sigma_1+\sigma')\left[\left(\frac{1}{\varepsilon\kappa}-\frac{d_L}{\varepsilon_L}\right)e^{-\kappa Nd}-\left(\frac{1}{\varepsilon\kappa}+\frac{d_L}{\varepsilon_L}\right)e^{\kappa Nd}\right]-2\left(U_{\text{tot}}-\frac{d_L}{\varepsilon_L}(-1)^N\sigma'\right)}{\left(\frac{1}{\varepsilon\kappa}-\frac{d_L}{\varepsilon_L}\right)\left(\frac{1}{\varepsilon\kappa}-\frac{d_1}{\varepsilon_1}\right)e^{-\kappa Nd}-\left(\frac{1}{\varepsilon\kappa}+\frac{d_L}{\varepsilon_L}\right)\left(\frac{1}{\varepsilon\kappa}+\frac{d_1}{\varepsilon_1}\right)e^{\kappa Nd}}. \tag{4.49}$$

Rewritten in terms of capacitances this result is equal to the result which was obtained for well-ordered charges when the effective polyelectrolyte charge σ_{eff} in Eq. (4.43) is replaced by σ'. Thus in our model the actual charge distribution within the PEMs is not crucial for the interpretation of the signal decrease and thus for the screening inside the polyelectrolyte film. However, the actual amount of adsorbed charges derived from the model will depend on the degree of charge overlap. In addition, surface properties such as the density of surface sites that can be protonated and deprotonated have an influence on the signal amplitude [63]. This surface site density influences the charge sensitivity

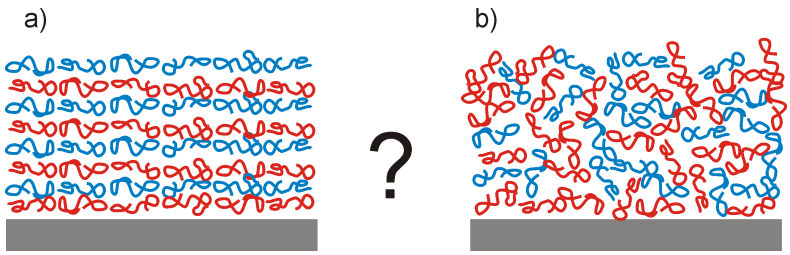

Figure 4.14: Two extreme cases for the charge distribution in PEMs are shown schematically. Positively charged and negatively charged polyelectrolytes can either be assumed to be well ordered in a layered structure (a) or totally intermixed leading to an overall neutral polyelectrolyte film (b).

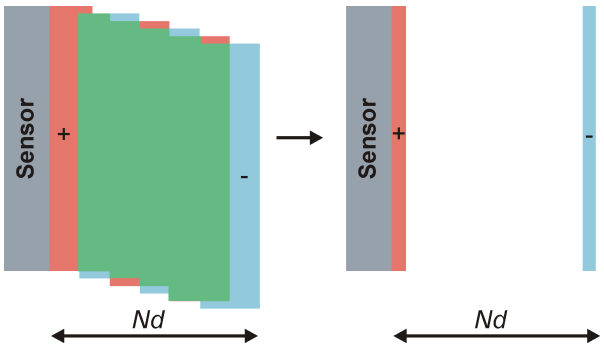

Figure 4.15: Layers can be thought of as overlapping. Negative charges (blue) and positive charges (red) neutralize each other (green) so that the only charges remaining are situated at the silicon oxide/polyelectrolyte interface and the polyelectrolyte/electrolyte interface, respectively. The layers have been displaced vertically for clarity.

of the sensor because any change of surface charge caused by adsorbed molecules can partially be compensated by protonation or deprotonation, which has been neglected in our capacitor model, where a constant surface charge was assumed. This effect can alter the signal amplitude, however relative measurements, such as the signal decrease with increasing number of layers are not affected.

Determination of $\Delta\psi_{\mathrm{amp}}(\mathbf{N})$. We have determined the thickness of the multilayer films by ellipsometry and X-ray reflectivity. Knowing the thickness of the polyelectrolyte multilayers, the screening of charges by mobile ions inside the PEMs can be quantified. For this purpose, we could in principle apply Eq. (4.43). However, this equation contains several unknown parameters such as the total voltage U_{tot} and the surface charge of the silicon oxide σ_1. Indeed, in section 4.2.2 we have plotted the decay of the signal amplitude $\Delta\psi_{\mathrm{amp}}$ against the number of layers deposited as a measure for the screening inside the polyelectrolyte films. The use of $\Delta\psi_{\mathrm{amp}}$ allows us to get rid of the parameters U_{tot} and σ_1 for

$\kappa d \ll 1$ ($\exp(\kappa d) \approx 1$), thus for a screening length much larger than the monolayer thickness. For this condition, the potential change between adjacent layers $U_1(N) - U_1(N-1)$, which equals the signal amplitude $\Delta\psi_{\mathrm{amp}}$, can be written as

$$U_1(N) - U_1(N-1) \approx \frac{1}{\kappa\varepsilon}\frac{d_1}{\varepsilon_1}\frac{4\frac{d_L}{\varepsilon_L}(-1)^N\sigma'}{\left(\frac{1}{\varepsilon\kappa}-\frac{d_L}{\varepsilon_L}\right)\left(\frac{1}{\varepsilon\kappa}-\frac{d_1}{\varepsilon_1}\right)e^{-\kappa Nd} - \left(\frac{1}{\varepsilon\kappa}+\frac{d_L}{\varepsilon_L}\right)\left(\frac{1}{\varepsilon\kappa}+\frac{d_1}{\varepsilon_1}\right)e^{\kappa Nd}}. \tag{4.50}$$

For even numbers of N as plotted in section 4.2.2 and rewritten in terms of capacitances this leads to

$$\begin{aligned}\Delta\psi_{\mathrm{amp}}(N) &= U_1(N) - U_1(N-1) \\ &= \frac{\sigma\, C_{\mathrm{D}}^{-1}}{(C_{\mathrm{S}}/C_{\mathrm{P}} + C_{\mathrm{P}}/C_{\mathrm{D}})\sinh(\kappa Nd) + (1 + C_{\mathrm{S}}/C_{\mathrm{D}})\cosh(\kappa Nd)}.\end{aligned} \tag{4.51}$$

4.2.5 Determination of Dielectric Properties and Concentration of Mobile Ions

Determination of the Screening Length. For the interpretation of the signal decrease shown in section 4.2.2 we can apply Eq. (4.51). Here, the number of layers, N, appears only in the hyperbolic functions. A value for the screening length κ^{-1} inside the PEMs can be obtained from the measured signal amplitude $\Delta\psi_{\mathrm{amp}}$ with the thickness d of the polyelectrolyte layers at the given ionic strength. As can be seen in Fig. 4.9 and Fig. 4.10, the measured $\Delta\psi_{\mathrm{amp}}$ can be fitted for κd using Eq. (4.51). For PAH/PSS multilayers we find $\kappa^{-1} = 6.3 \pm 1.0$ nm for the buildup of the PEMs from buffer solution containing 50 mM NaCl and $\kappa^{-1} = 6.5 \pm 1.0$ nm for deposition from buffer containing 500 mM NaCl. For PDADMAC/PSS multilayers, screening is less pronounced. For a monolayer thickness of 1 nm [28], a screening length of $\kappa^{-1} = 33$ nm is obtained for layers deposited from buffer solution containing 50 mM NaCl. This is by a factor of 5 larger than the corresponding value for PAH/PSS films. The screening length depends not only on the ionic strength and thus on the concentration of mobile ions, but also on the dielectric constant of the polymer film as shown by Eq. (2.3).

$$\kappa^{-1} = \left[\frac{\varepsilon_0\varepsilon_r kT}{e^2\sum_i n_i^0 z_i^2}\right]^{\frac{1}{2}}. \tag{4.52}$$

Determination of ε and c. A high dielectric constant will increase the screening length, while a high concentration of mobile ions will reduce it. At the same time, the concentration c of mobile ions inside the polyelectrolyte film depends on the dielectric constant

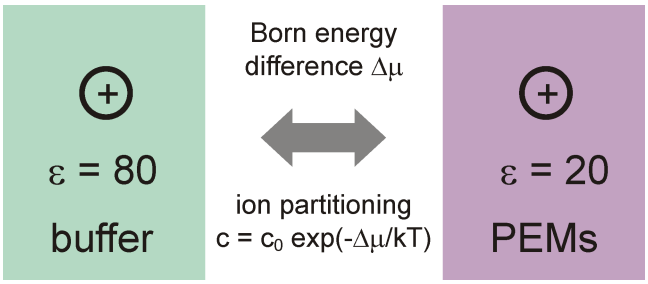

Figure 4.16: The ion partitioning between two media with different dielectric constants is governed by the Born energy difference.

of the film because the dominant factor governing the ion-partitioning in the PEMs/bulk electrolyte system is the Born energy change

$$\Delta\mu = \frac{e^2}{8\pi\varepsilon_0 a}\left[\frac{1}{\varepsilon} - \frac{1}{\varepsilon_\mathrm{w}}\right], \tag{4.53}$$

which arises because of the difference in self-energy of the ions (of radius a) in the PEMs and in the bulk (Fig. 4.16). The concentration c of mobile ions is set by the thermodynamic equilibrium between the ions in the bulk solution (of concentration c_0) and those in the PEMs. Applying the Boltzmann distribution law, this leads to an ion-partitioning according to [64, 65]

$$c = c_0 \exp\left(-\Delta\mu/kT\right). \tag{4.54}$$

Combining Eq. (4.52) with Eq. (4.53) and Eq. (4.54), the relative dielectric constant ε of the PEMs can be calculated numerically from the values obtained for κ

$$\frac{\kappa^2}{\kappa_\mathrm{w}^2} = \frac{\varepsilon_\mathrm{w}}{\varepsilon}\exp\left(-\frac{\frac{e^2}{8\pi\varepsilon_0 a}\left[\frac{1}{\varepsilon} - \frac{1}{\varepsilon_\mathrm{w}}\right]}{kT}\right). \tag{4.55}$$

Knowing ε and κ, also the concentration of mobile ions can be determined by Eq. (4.52). For PAH/PSS multilayers we find $\varepsilon = 30 \pm 2$ and $\varepsilon = 21 \pm 1$ for the multilayers adsorbed from buffers containing 50 mM NaCl and 500 mM NaCl, respectively. The corresponding concentration of mobile ions inside the PEMs amounts to 0.9 ± 0.3 mM and 0.6 ± 0.2 mM, respectively. For the PDADMAC/PSS film deposited from buffer containing 50 mM NaCl a relative dielectric constant of $\epsilon = 19$ is obtained. This corresponds to a concentration of mobile ions within the PDADMAC/PSS film of 0.02 mM, which is more than a magnitude smaller than the value obtained for PAH/PSS at the same ionic strength of the bulk electrolyte. For all films the concentration of mobile ions inside the PEMs is reduced

by 1-3 orders of magnitude as compared to the bulk concentration as a consequence of the low dielectric constant of the film. For PDADMAC/PSS films this leads to a screening of charges which is almost negligible in sensor applications. The different values for ϵ obtained for the two different polycations can be interpreted in terms of the different chemical structure of the polymer backbone (Fig. 4.5). Measurements of the contact angle of PDADMAC and PAH coated surfaces demonstrated a higher hydrophobicity of PDADMAC [66] corresponding to the lower ϵ found in this paper. Different values for the dielectric constants of PDADMAC/PSS films ($\epsilon = 120$) and PAH/PSS films ($\epsilon = 50$) were derived from pyrene fluorescence measurements probing the local polarity of the films [67]. Pyrene fluorescence data of the films has been compared with that of various isotropic solvents of low molecular weight. Of course, not only the backbone, but also the charge density affects the hydrophobicity. However, it is difficult to compare the charge density of both types of polyelectrolytes, since PAH is a weak polyelectrolyte and thus can change the degree of protonation at the interface with respect to the degree of protonation in solution. The different values for ε obtained for PAH/PSS films deposited from different salt concentrations can be interpreted in terms of a different water content of the polyelectrolyte films. A water content of about 40% was estimated by neutron reflectometry for PAH/PSS films deposited from different salt concentrations [19, 68, 69, 70] suggesting that the ionic strength of the solution does not change the water content of the PEMs. Assuming an equal water content for both salt concentrations, the observed variation of the dielectric constant could be ascribed to a different fraction of immobilized to free water within the polymer layers as oriented water molecules show a lower dielectric constant. Decreased water mobility inside PEMs has already been determined by NMR studies [71]. Comparing measurements at different conditions will be necessary to further determine the origin of the dielectric constants of PEMs.

4.2.6 pH Response and Permeability for Protons

Monitoring of the pH Sensitivity. In the previous section we have discussed the concentration of mobile ions (NaCl from the buffer solution) inside polyelectrolyte films. In this section we will take a look at the concentration of protons present in the PEMs. Using a pH-sensitive dye it has been shown that PEMs exhibit a high permeability for protons [21]. Thus after the deposition of polyelectrolyte films, the pH sensitivity of the SOI sensor should be maintained. To check this, the pH response of the sensor was monitored during the deposition of PDADMAC/PSS multilayers from buffer solution containing 50 mM NaCl at pH 7.5. After each deposition step, a buffer solution of pH 8.5 was injected.

When a stable signal was obtained, the flow chamber was rinsed with buffer solution of pH 7.5. In Fig. 4.17 the potential change $\Delta\psi_{\mathrm{pH}}$ caused by this buffer exchange was plotted against the number of layers deposited. It was found that the pH sensitivity is not changed considerably by the adsorption of charged polymers confirming the high permeability for protons. An explanation for the high permeability of protons as compared to ions such as Na^+ could be a Grotthuss-like mechanism of delocalized protons inside the polyelectrolyte films leading to an almost equal partitioning of protons between bulk electrolyte and PEMs. While other cations such as Na^+ or K^+ simply diffuse through random thermal motion, protons can diffuse through the hydrogen bond network of water and other molecules [72]. In previous publications, it has been shown that this effect can explain e.g. the selectivity of proton channels [73, 74].

Oscillations of the pH Response. As can be seen from Fig. 4.17, the adsorption of alternately charged polymers leads to defined oscillations of $\Delta\psi_{\mathrm{pH}}$, the amplitude of which is decreasing slowly with increasing layer number. A more positive surface charge (after the deposition of PDADMAC) increases the pH sensitivity, while a more negative surface charge (after the deposition of PSS) decreases it. These oscillations can be ascribed to a change of the local pH at the sensor surface caused by the adsorption of charges. A more positive surface will increase the local pH, whereas a more negative surface will decrease it. This effect can be explained within the site binding theory. Therefore, we modify the Grahame equation (Eq. (2.6)) by accounting for both the silicon oxide surface charge σ_{S} and the additional polyelectrolyte charge σ_{extra}

$$\sigma_{\mathrm{S}} + \sigma_{\mathrm{extra}} = \left(8\varepsilon_0\varepsilon_r kTn^0\right)^{\frac{1}{2}} \sinh\left(\frac{ze\psi_{\mathrm{S}}}{2kT}\right). \tag{4.56}$$

In combination with Eq. (2.15)

$$\sigma_{\mathrm{S}} = eN_{\mathrm{S}} \frac{\left(\left[\mathrm{H}^+\right]/K_{\mathrm{A}}\right)\exp\left(-e\psi_{\mathrm{S}}/kT\right) - \left(K_{\mathrm{B}}/\left[\mathrm{H}^+\right]\right)\exp\left(e\psi_{\mathrm{S}}/kT\right)}{1 + \left(\left[\mathrm{H}^+\right]/K_{\mathrm{A}}\right)\exp\left(-e\psi_{\mathrm{S}}/kT\right) + \left(K_{\mathrm{B}}/\left[\mathrm{H}^+\right]\right)\exp\left(e\psi_{\mathrm{S}}/kT\right)} \tag{4.57}$$

ψ can be calculated numerically as a function of the pH. Assuming an additional charge σ_{extra} of 0.02 $\frac{\mathrm{C}}{\mathrm{m}^2}$ [56] and a surface site density of $N_{\mathrm{S}} = 5{\cdot}10^{18}\ \mathrm{m}^{-2}$ [51], an initial difference in $\Delta\psi_{\mathrm{pH}}$ of approximately 3 $\frac{\mathrm{mV}}{\mathrm{pH}}$ is found with the more positively charged surface showing the higher pH sensitivity as it was observed in the measurement. However, this simple model does not take into account the screening effects inside the polyelectrolyte films as the charges are assumed to be situated directly at the sensor surface. Screening by mobile ions will cause the oscillations to finally level out since the adsorption of another polyelectrolyte layer is not sensed any more at the sensor surface. The absolute value of the pH sensitivity

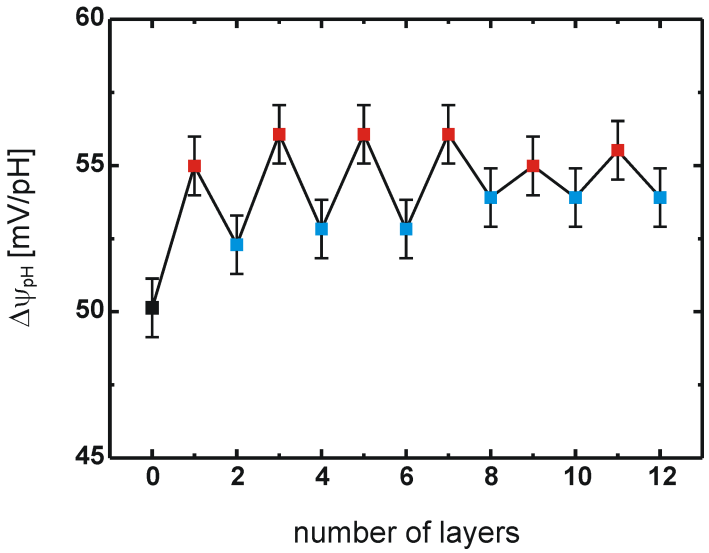

Figure 4.17: The pH response was monitored during the deposition of PDADMAC/PSS multilayers. Only slight oscillations of the pH response could be observed with recharging of the sensor surface.

observed in the measurement is not obtained by the model using the parameters given above, yet it offers a qualitative understanding of the specified oscillations. Using a pH-sensitive dye, a dependence of the apparent pK value of the dye on the charge of the terminating polyelectrolyte layer has been observed [21]. Assuming that the real pK value of the dye is not changed, this indicates a deviation of the local pH in the film from the bulk pH. The apparent pK value is decreased for a positively terminated surface, while it is increased for a negatively terminated surface. This corresponds to a local increase or decrease of the pH, respectively, which is in agreement with our observations. In addition, it was found that the influence of the terminating polyelectrolyte layer on the fluorescent dye decreases with increasing layer number, which can be explained in terms of screening.

4.2.7 Polyelectrolytes with Variable Charge Density: Multilayer Buildup Threshold

For the investigation of the multilayer formation, polyelectrolytes with a varying degree of charge (DC) have been employed in previous studies for ellipsometric, spectroscopic and quartz crystal microbalance measurements as well as for X-ray reflectivity studies [24, 25, 26, 27, 28]. In these studies, the influence of polymer charge density was studied using the strong polyanion poly(styrene sulfonate), PSS combined with

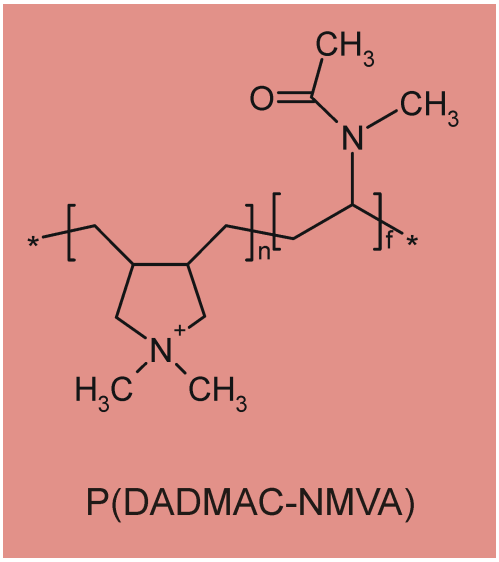

Figure 4.18: Chemical structure of the statistical copolymer P(DADMAC-*stat*-NMVA). The degree of charge can be varied in this polymer.

the linear statistical copolymer poly(diallyl-dimethyl-ammoniumchloride-*stat*-*N*-methyl-*N*-vinylacetamide), P(DADMAC-*stat*-NMVA) at various DCs (Fig. 4.18). It was found that the multilayer formation stops after a few deposition steps for a DC below 75%. Charge overcompensation was suggested to be the stringent condition for multilayer formation. The direct electrical detection of multilayer deposition makes it possible to check this hypothesis and gain further insight into the driving forces of multilayer formation.

Experimental Procedure. The deposition of the cationic polyelectrolyte P(DADMAC-*stat*-NMVA) with a variable charge density and the fully charged PSS was studied by field effect detection and ellipsometry. P(DADMAC-*stat*-NMVA) consists of positively charged diallyldimethylammonium chloride monomers (DADMAC) and neutral *N*-methyl*N*-vinylacetamide (NMVA) monomers. It was used at total charge densities of 0% (pure PNMVA), 24%, 50%, 75% and 100% (pure PDADMAC). Multilayer deposition was carried out from buffer containing 50 mM NaCl. During the deposition process, the sheet resistance is monitored continuously. Ellipsometry has been carried out using an Optrel Multiscope. Samples have been prepared by a dipping procedure as described in section 4.2.3. The samples were briefly rinsed with water and dried in a nitrogen stream before the measurements [75].

Results and Discussion. Fig. 4.19 shows the increase of thickness with increasing number of layers deposited. For the uncharged polymer (DC 0%), the deposition stops after the second layer, for a DC of 50% four layers are adsorbed before the deposition stops.

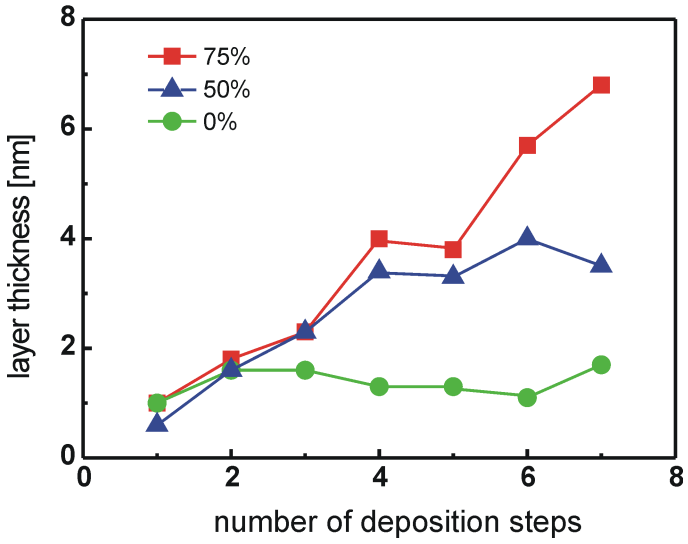

Figure 4.19: The increase of total PEMs thickness is shown as a function of the number of layers deposited. For a DC below 75% the deposition stops after the first cycles, whereas otherwise a continuous increase the thickness is observed.

For a DC beyond the multilayer deposition threshold, (75% in this case), the thickness increases continuously with the number of layers. In the electrical measurements, the deposition of PEMs results in defined potential shifts (Fig. 4.7). Nevertheless, small potential oscillations of constant amplitude are observed also when the film thickness does not increase anymore as can be seen in Fig. 4.20 for DCs of 0% and 24%. Thus, even for charge densities below the multilayer buildup threshold, small potential shifts are obtained. We ascribe this to a dynamic exchange of polyelectrolyte molecules [30]. Some polymers of the topmost layer desorb upon addition of the oppositely charged polyelectrolyte solution, which has previously been demonstrated by fluorescence labeling [20]. The measured potential oscillations for the DC of 24% correspond to an exchange of surface charge of $\Delta\sigma \approx 3$ mC/m^2 as can be estimated from the Grahame equation (Eq. (2.6)). For the deposition of the uncharged polymer PNMVA, oscillations are of the order of $\Delta\sigma \approx 2$ mC/m^2. Interestingly, an increase of the surface potential is also observed for the adsorption of the uncharged PNMVA (Fig 4.20), which cannot be explained within the capacitor model. A pure dielectric effect can be excluded, as this should lead to a decrease in surface potential. The capacitor model excludes effects such as variation of the local pH and the specific adsorption of ions, which possibly could explain the observed potential shift. At least for the adsorption of the first polyelectrolyte layers, such effects could play a role and be superposed to the pure charge and dielectric shift implied by the capacitor model.

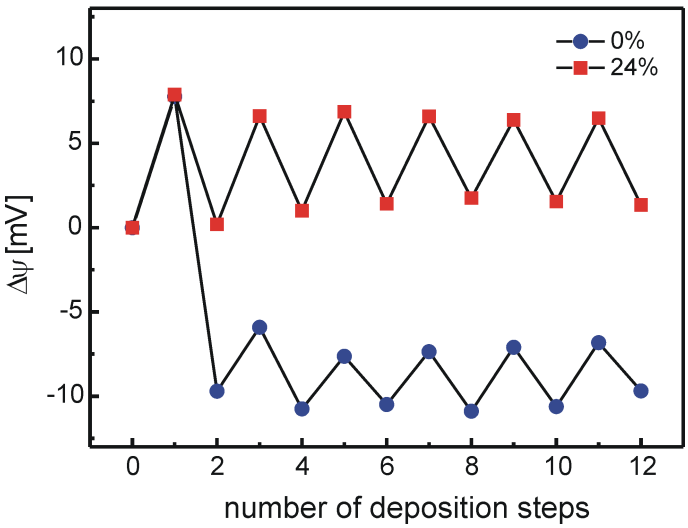

Figure 4.20: The polyelectrolyte deposition is shown for P(DADMAC-*stat*-NMVA) with a DC of 24% and for pure PNMVA (DC 0%). Typical errors are in the range of 2 mV. Even for DCs below the deposition threshold where no multilayer buildup takes place, small oscillations are observed in the course of the deposition cycles. This can be explained in terms of a small amount of polyelectrolyte that exchanges with the polyelectrolyte solution.

4.2.8 Charge Compensation and Multilayer Buildup

Calculation of the Total Surface Charge. In the previous section we have found that for the buildup of multilayers from P(DADMAC-*stat*-NMVA)/PSS a minimal charge density of 50% is needed. In former studies it was assumed that a charge overcompensation is required for multilayer formation [27]. The SOI based field effect device enables us to verify this assumption. Here, we take advantage of the fact that changing the ionic strength of the buffer solution on top of a field effect device causes a change in the Debye capacitance of the electrical double layer and thus in the surface potential, which is detected by the measured sheet resistance (Fig. 4.21). The change in surface potential $\Delta\psi_{\text{salt}}$ caused by a change of the ionic strength of the buffer solution is a direct measure of the sensor's surface charge: for an uncharged surface, no such change in surface potential occurs. The total surface charge $\sigma_S + \sigma_{\text{extra}}$ can be calculated numerically from the change in surface potential combining the modified Grahame equation (Eq. (4.56)) with site-binding theory (Eq. (2.15)) as explained in section 4.2.6. In this calculation, screening within the polyelectrolyte film is neglected, which is an acceptable simplification for PDADMAC/PSS layers where little screening is found (see section 4.2.5).

Buffer Exchange Experiment. To monitor the total surface charge σ during multilayer

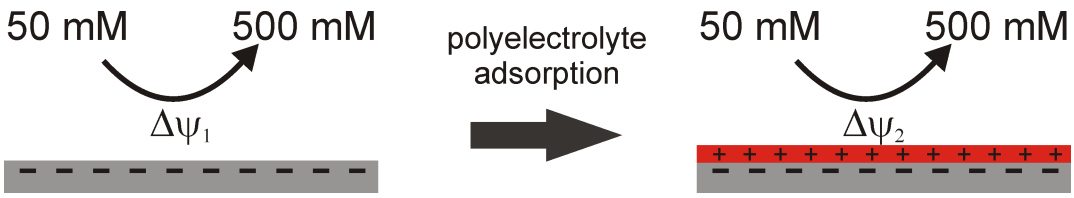

Figure 4.21: In this type of experiment, the ionic strength on top of the sensor surface is exchanged from 50 mM to 500 mM. This leads to a change in the capacitance of the double layer and thus to a change of the surface potential. This change of surface potential depends on the total surface charge and thus is changed by the adsorption of charged molecules such as polyelectrolytes.

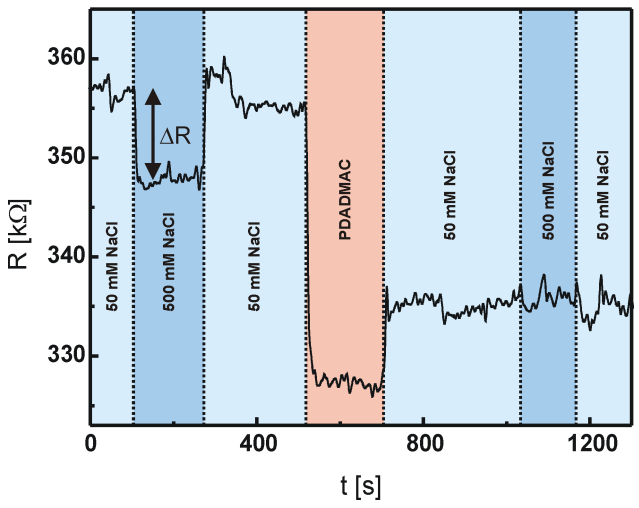

Figure 4.22: The experiment shows the adsorption of PDADMAC (DC 100%) to a clean sensor surface. The sheet resistance is plotted against time. For the negatively charged silicon oxide surface, a change of the ionic strength of the buffer solution (50 mM to 500 mM NaCl and back) causes a change of the surface potential ψ and thus of the sheet resistance R as indicated by the arrow. After the adsorption of PDADMAC, the surface charge is exactly compensated by the polyelectrolyte charge, and therefore no change in sheet resistance is observed upon buffer exchange.

buildup, we have performed an experiment, in which two buffers with different ionic strength are exchanged after each polyelectrolyte deposition step. Fig. 4.22 shows such buffer exchanges before and after the deposition of PDADMAC to a blank sensor surface. The sheet resistance of the SOI device is plotted against time. First, a 10 mM Tris buffer at pH 7.5 containing 50 mM NaCl is applied to a clean silicon oxide sensor surface. Next, the ionic strength is changed by injecting a 10 mM Tris buffer at the same pH but with a higher concentration of NaCl of 500 mM. As the silicon oxide is negatively charged at pH 7.5, this leads to a lower sheet resistance corresponding to a less negative surface potential. Subsequently, the solution on top of the sensor is replaced again by the buffer containing 50 mM NaCl and the sheet resistance increases again to the previous level. Now a PDADMAC solution (DC 100%) is injected and the positively charged polymer binds to the sensor surface increasing the surface potential and thus decreasing the sheet resistance. The sensor is rinsed with the 50 mM NaCl buffer which is then exchanged against the 500 mM NaCl buffer. This exchange now is not accompanied by a change in sheet resistance indicating a sensor surface that is uncharged in total. Therefore the negative charge of the sensor surface has been exactly compensated by the charge of the PDADMAC layer.

Charge Compensation for Different DCs. Fig. 4.23 shows the changes in surface potential caused by a buffer exchange between 50 mM and 500 mM NaCl $\Delta\psi_{\text{salt}} = \psi_{500\text{ mV}} - \psi_{50\text{ mV}}$ and the corresponding total surface charge $\sigma = \sigma_{\text{S}} + \sigma_{\text{extra}}$ for different polyelectrolytes as the topmost layer. The experiment shown in Fig. 4.22 is represented by the first part of Fig. 4.23(a), where the buffer exchange leads to a change in surface potential $\Delta\psi_{\text{salt}}$ of 9 mV for the bare sensor surface and 0 mV after the deposition of a PDADMAC layer. After the following adsorption of PSS, an even higher $\Delta\psi_{\text{salt}}$ of 18 mV is observed. This can be interpreted as follows: The adsorbing positively charged PDADMAC does not overcompensate, but exactly compensate the negative charge of the silicon oxide surface ($\sigma = -7$ mC/m^2, as derived from $\Delta\psi_{\text{salt}} = 9$ mV). Next, the negatively charged PSS is adsorbed on top of the PDADMAC layer. After this deposition step, $\Delta\psi_{\text{salt}}$ amounts to 18 mV, indicating that with the PSS about twice the charge density of the original silicon oxide surface ($\sigma = -14$ mC/m^2) has been absorbed. To achieve multilayer buildup, the following layer of positively charged polyelectrolyte should again compensate the previous surface charge to allow for the continuation of the formation process, assuming that each PSS-terminated polyelectrolyte multilayer surface is identical. As shown in Fig. 4.23(b) and (c) this is the case for P(DADMAC-*stat*-NMVA) with a DC of 75% but not for a DC of 50%. For 75%, the charge of a PSS terminated surface is compensated by the adsorption of the positively charged polyelectrolyte ($\Delta\psi_{\text{salt}} = 0$), whereas

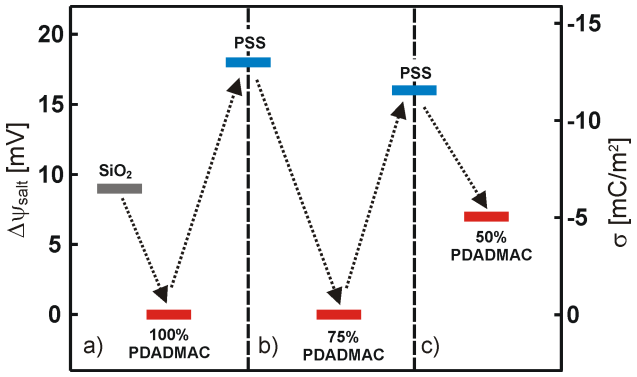

Figure 4.23: The change in surface potential $\Delta\psi_{\text{salt}}$ caused by a buffer exchange between 50 mM and 500 mM NaCl is shown for different polyelectrolytes (left axis, errors in the range of 2 mV). $\Delta\psi_{\text{salt}}$ is calculated from the change in sheet resistance ΔR as indicated in Fig. 4.22. On the right axis, the corresponding total surface charge σ is shown as derived from $\Delta\psi_{\text{salt}}$. In (a) the change in surface potential and the total surface charge are given before and after the adsorption of fully charged PDADMAC to the bare sensor surface and after the following adsorption of PSS. In (b) and (c) the corresponding values are given before and after the adsorption of P(DADMAC-*stat*-NMVA) to a PSS terminated surface.

for 50% no full charge compensation of the previous PSS surface occurs ($\Delta\psi_{\text{salt}} = 7$ mV corresponding to a total surface charge of $\sigma = -5$ mC/m^2). Thus the threshold for charge compensation lies between 50 and 75% in accordance with the threshold observed for the formation of multilayers. The first PDADMAC layer adsorbs at only half of the charge density ($\Delta\sigma = +7$ mC/m^2) that is found for the following layers of PSS and PDADMAC ($\Delta\sigma = \mp 14$ mC/m^2). Due to the difference in surface potential of the respective negative surface it is assumed that the structure of the first PDADMAC layer differs from the latter adsorbed PDADMAC layers. This can be understood in terms of different physical and chemical properties of the underlying silicon oxide surface as compared to the polyelectrolyte layers. The absence of charge reversion in the presented experiments cannot be explained by electrostatic driving forces within a strict mean-field approach. However, when local interactions are taken into account, multilayer formation can be explained even in the case of exact charge compensation. A delicate balance of local electrostatic and non-electrostatic interactions as well as the gain of entropy by counter ion release is thus responsible for the multilayer formation [76, 65, 33, 77]. A similar reason is given for the formation of multilayers at high ionic strengths (> 0.5 M), where the surface charges are more or less screened [28]. The exact values of the charge densities adsorbing in each step as well as the minimum DC required for the multilayer formation will certainly depend on the system under investigation, as for different polyelectrolytes, a

different threshold has been observed [78].

4.3 Detection and Quantification of Enzymatic Activity

In this part of the thesis, we show that we can make use of the SOI device as a biosensor for the detection of enzymatic activity. Field-effect sensors such as the SOI sensor are well-suited to monitor polyelectrolyte adsorption as demonstrated in the previous sections. Therefore, enzymes could potentially be detected which either cleave polyelectrolytes or build up polyelectrolytes . The latter has been previously employed in the detection of PCR products by a field effect device [79], where negatively charged DNA polymers are produced from single nucleotides. There, it has been found that PCR products can be detected over reagents such as the Taq polymerase or nucleotide monomers indicating that permanent electrostatic adsorption requires stronger multivalent interactions. Here, we show that we can detect enzymes which cleave polyelectrolyte substrates. In the following sections, two enzymes are studied: the protease trypsin and the glycosidase heparinase. Polyelectrolytes strongly adsorb to a charged surface (e.g. PEMs buildup) whereas small charged molecules such as monomers or dimers are hardly adsorbed. Based on this, we have developed a novel technique for the detection of the enzymes mentioned above. It has been demonstrated by simulations that the binding of (poly-)electrolytes to a charged surface is achieved when the attractive free energy is greater than kT [80]. For the adsorption of polyelectrolytes of different length, the gain in electrostatic energy per monomer unit is approximately the same. However, for longer polymers less translational entropy per monomer unit is lost as compared to shorter ones [81], which leads to a stronger adsorption.

4.3.1 Protease Activity: Trypsin Digestion of Poly-L-Lysine

Trypsin (EC 3.4.21.4) is a serine endopeptidase produced in the pancreas with a molecular weight of 23.8 kDa [82]. A serine residue in the active site nucleophilicly attacks the carbonyl-C of the substrate's peptide bond. An anionic aspartate residue inside its substrate binding pocket attracts cationic residues thereby generating its substrate specificity. Trypsin predominantly cleaves proteins at the C-terminal side of lysine and arginine residues. Thus, the natural polyelectrolyte poly-L-lysine (PLL) is a suitable substrate for trypsin [83]. It was found by paper chromatography that the main products are dilysine and trilysine because the end bonds next to a carboxyl or amino group are not split [84].

Monomer vs. Polymer Adsorption. In our detection scheme, we employ PLL as a

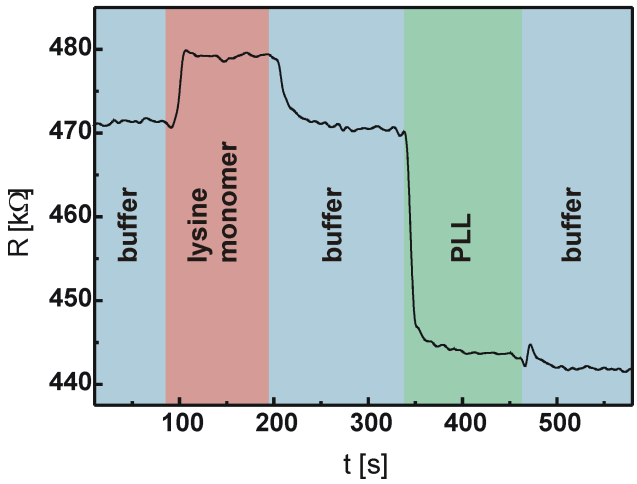

Figure 4.24: Lysine monomers at 0.01% (w/v) in Tris buffer are injected into the fluid chamber. Afterwards, the system is rinsed with buffer. No significant change of the sheet resistance is observed. Next, PLL at the same concentration (0.01% (w/v)) is injected and the system is rinsed with buffer. The resulting decrease of sheet resistance corresponds to an increased surface potential due to the binding of positively charged PLL molecules to the sensor surface.

substrate for trypsin. The positively charged PLL readily adsorbs to a negatively charged silicon oxide surface [2] and can easily be detected by the SOI sensor. On the contrary, we have shown that the adsorption of lysine monomers to the sensor surface cannot be detected. This can be seen in Fig. 4.24. First, the sensor is equilibrated with Tris buffer (10 mM Tris containing 50 mM NaCl at pH 7.4). Next a 0.01% (w/v) solution of lysine in Tris buffer is injected into the flow chamber. The increase of the sheet resistance and thus decrease of the surface potential is caused by the basicity of lysine, which increases the pH of the solution. After the injection of pure buffer solution, the sheet resistance decreases again to the previous value. Hence, no binding of lysine monomers to the sensor surface can be detected. Now a 0.01% (w/v) PLL solution in Tris buffer is injected into the flow chamber. This leads to a decrease of the sheet resistance corresponding to an increase of the surface potential caused by the adsorption of the positively charged polymer. When the chamber is rinsed with buffer solution, no further change in surface potential is observed. This indicates the irreversible binding of PLL caused by a lower entropy loss as compared to the monomers.

Detection of Trypsin. The trypsin cleavage of PLL into small peptides is employed for the electrical detection of trypsin activity. Predominantly, dimers and trimers are obtained [84], which are too short to efficiently bind to the sensor surface as shown for

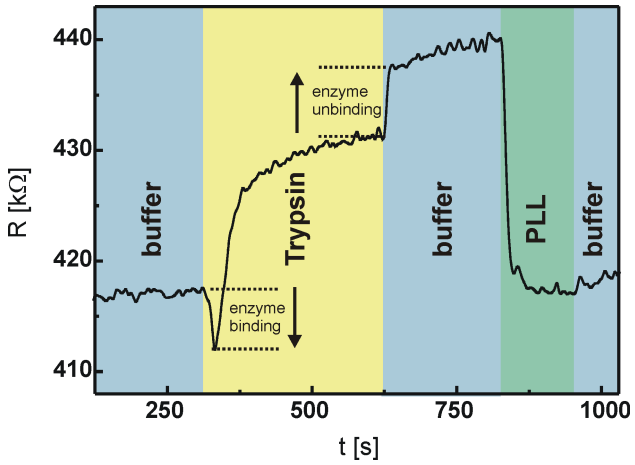

Figure 4.25: A PLL covered sensor chip is equilibrated with buffer. Next, a trypsin solution of 0.5 mg/ml is injected. The enzyme cleaves the PLL substrate. The fragments are released into the solution which decreases the surface potential as positively charged molecules desorb from the surface. The chip is rinsed with buffer and PLL can be readsorbed to the surface. Arrows indicate the binding and unbinding of the enzyme.

lysine monomers. No monomers can be obtained by trypsin digestion, as the endopeptidase trypsin only breaks peptide bonds within the molecule. For the online detection of trypsin activity, we start with a PLL coated sensor chip as shown in Fig. 4.25. After equilibration with buffer, a 5 mg/ml trypsin solution is injected (from bovine pancreas, Sigma-Aldrich). The enzyme starts cleaving the polyelectrolyte and the fragments are released into the solution. Thus, positively charged molecules desorb from the surface which decreases the surface potential and therefore increases the measured sheet resistance. Next, the chip is rinsed with buffer, which further increases the sheet resistance. This could be caused by the release of surface bound trypsin as indicated in by the arrows in Fig. 4.25. At a pH of 7.4, the net charge of trypsin is positive as it shows a pK value of 11 [85], which is in agreement with a decrease of the sheet resistance caused by the binding of the enzyme and an increase of the sheet resistance with its unbinding. Additionally, this effect vanishes for smaller trypsin concentrations, where PLL digestion is slower and the surface is not saturated with trypsin. The sensor can be reused for trypsin detection by reloading it with PLL, which demonstrates that the polyelectrolyte has efficiently been removed from the surface. The initial velocity of the trypsin digestion in terms of surface potential change per second can be extracted from the graph using the calibration data. This initial velocity is plotted for different trypsin concentrations in Fig. 4.26. Concentrations down to 50 ng/ml could be detected corresponding to a molar concentration of 2 nM.

Proof of Specificity. To control the specificity of the digestion, a second protease with

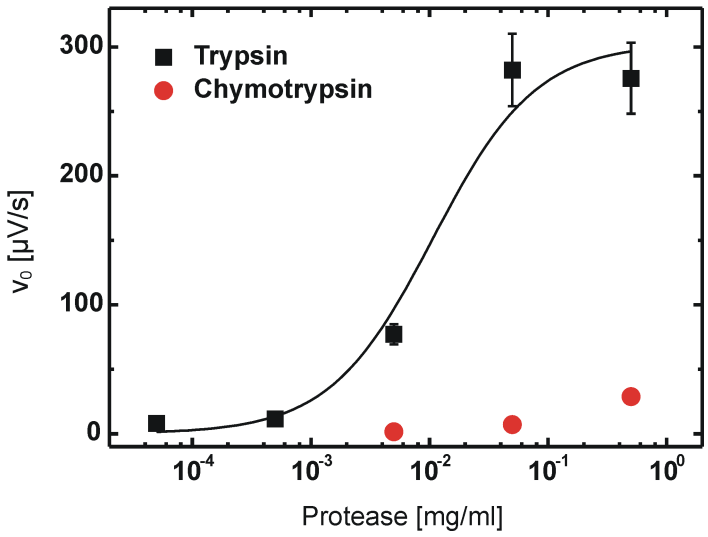

Figure 4.26: The initial velocity of the PLL digestion as measured in terms of surface potential change per second is plotted for different trypsin and chymotrypsin concentrations. Trypsin activity could be detected down to 50 ng/ml, chymotrypsin concentration down to 50 μg/ml. The solid line represents a fit by the surface Michaelis-Menten equation (Eq. (4.58)).

different specificity was studied. Chymotrypsin (EC 3.4.21.1) is a similar serine endopeptidase also produced in the pancreas. It preferentially cleaves peptides at the C-terminal side of tyrosine, tryptophan, and phenylalanine. However, it has been shown that also the amide bonds in PLL are slowly hydrolyzed by chymotrypsin [86], yet not as efficiently as the digestion by trypsin. This was observed as a considerably lower initial velocity detected by the field effect device as shown in Fig. 4.26. In contrast to trypsin, chymotrypsin (from bovine pancreas, Sigma Aldrich) could only be detected down to 50 μg/ml corresponding to a molar concentration of 2 μM. Thus, it can be shown that PLL is a better substrate for trypsin as compared to chymotrypsin.

Surface Enzyme Kinetics. Conventional Michaelis-Menten kinetics cannot be applied for surface enzyme reactions as considered here. In contrast to solution kinetics, it is not the substrate concentration but the enzyme concentration which is varied. A quantitative model for enzyme-catalyzed surface reactions coupling both adsorption kinetics and enzyme kinetics has been proposed in Ref. [46]. In the case of trypsin digestion, the surface reaction can be divided into three steps: First, trypsin adsorbs onto the surface bound PLL forming an enzyme-substrate complex. Next, the enzyme-substrate complex reacts to form the surface bound products. In the last step, PLL fragments will desorb from the surface if short enough. If the surface enzyme reaction is slow compared to the adsorption

of the enzyme and the release of fragments into the solution, a steady state solution for the enzyme kinetics can be found [46]. Interestingly, it has the same functional form as obtained in a solution Michaelis-Menten kinetics. However, the surface reaction rate is a function of the solution enzyme [E] concentration instead of the substrate concentration

$$v_0 = \frac{v_{\max}[\mathrm{E}]}{K_\mathrm{M} + [\mathrm{E}]} \tag{4.58}$$

with the initial velocity v_0, the maximal velocity $v_{\max}$ and the surface Michaelis-Menten constant K_M. We assume that a change in surface charge is proportional to the corresponding change in surface potential, which holds in the Debye-Hückel limit. Then the initial velocity can be measured in terms of surface potential change per time unit. Thus we have applied Eq. (4.58) to the concentration dependent data of the trypsin digestion as shown in Fig. 4.26. The fit represented by the solid line yields a maximal velocity $v_{\max} = 300 \pm 20$ μV/s and a surface Michaelis-Menten constant of $K_\mathrm{M} = 400 \pm 150$ nM. Trypsin shows a high catalytic efficiency already at small enzyme concentrations combined with a high affinity for the substrate as can be seen from the small K_M value. As chymotrypsin was available only in a limited range of concentrations, a similar fit for chymotrypsin is impractical.

Inhibition of Trypsin. Next, we want to demonstrate the specific inactivation of trypsin by an enzyme inhibitor. Phenylmethylsulfonylfluoride (PMSF) is a serine protease inhibitor which covalently binds to the active site serine thereby inactivating the enzyme [87, 88]. Fig. 4.27 shows the inactivation of trypsin. A PLL coated sensor chip was equilibrated in buffer solution. PMSF was added to a 0.5 mg/ml solution of trypsin resulting in a final inhibitor concentration of 10 mg/ml. The solution was injected into the flow chamber, leading to a decrease of the sheet resistance, which could be ascribed to the high concentration of PMSF. After a rinse with buffer solution, only a slight increase in sheet resistance as compared to the previous buffer level is observed due to almost complete inactivation by PMSF. This can also be seen in the following reloading of the sensor with PLL solution: Only a small amount of PLL is adsorbed as the surface was already almost fully covered with PLL.

Conclusion. In summary, it has been shown that the enzymatic activity of the serine proteases trypsin and chymotrypsin can be monitored electrically employing the polyelectrolyte PLL as a substrate. The higher specificity of trypsin as compared to chymotrypsin towards a lysine containing substrate was demonstrated and analyzed quantitatively. Trypsin activity can be inhibited by the serine protease inhibitor PMSF. The detection of the enzymatic activity is based on the desorption of PLL fragments from the

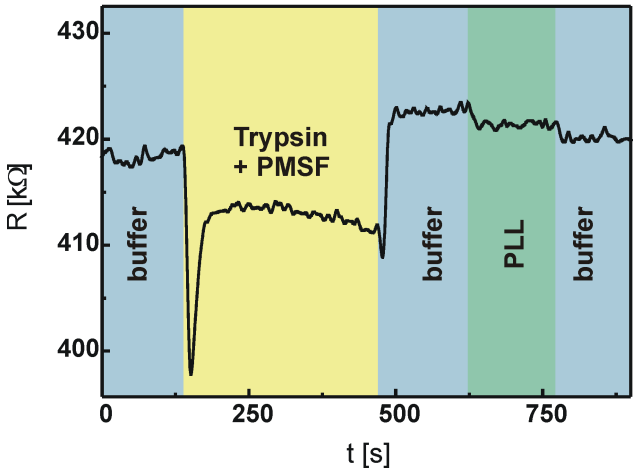

Figure 4.27: The inhibition of 0.5 mg/ml trypsin by the serine protease inhibitor PMSF is shown. After equilibration with buffer, a 0.5 mg/ml trypsin solution containing 10 mg/ml PMSF was added to a PLL coated sensor chip. Due to the inactivation of trypsin by PMSF, only a slight increase in sheet resistance is observed after a rinse with buffer solution.

sensor surface upon addition of the enzyme solution.

4.3.2 Glycosidase Activity: Heparin Digestion by Heparinase

In this section, we investigate if the presented approach for the detection of enzymatic activity can also be used with a different enzyme. Therefore we make use of the glycosidase heparinase, which cleaves heparin. Heparin is a highly sulfated glycosaminoglycan with an average of 2.5 sulfate residues per disaccharide unit, which makes it the most highly charged polymer in mammalian tissue [89]. Glycosaminoglycans are unbranched polysaccharides consisting of alternating uronic acid and hexosamine residues. Native heparin is a polymer with a molecular weight ranging from 3 kDa to 40 kDa. The most common disaccharide unit of heparin is shown in Fig. 4.28. Under physiological conditions the ester and amide sulfate groups are deprotonated and thus negatively charged. Heparin inhibits the clotting of blood and occurs almost exclusively in the intracellular granules of mast cells in arterial walls.

Heparin Detection. Heparin has previously been detected by field effect devices [90, 91]. For its detection, it has been adsorbed on surfaces covered with the cationic protein protamine. Here, the negatively charged sensor surface is instead covered with PLL (0.01% (w/v) in 10 mM Tris containing 50 mM NaCl at pH 7.4). Both protamine and PLL are pos-

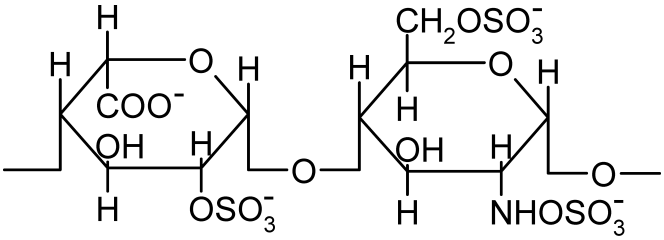

Figure 4.28: Most common disaccharide unit of heparin.

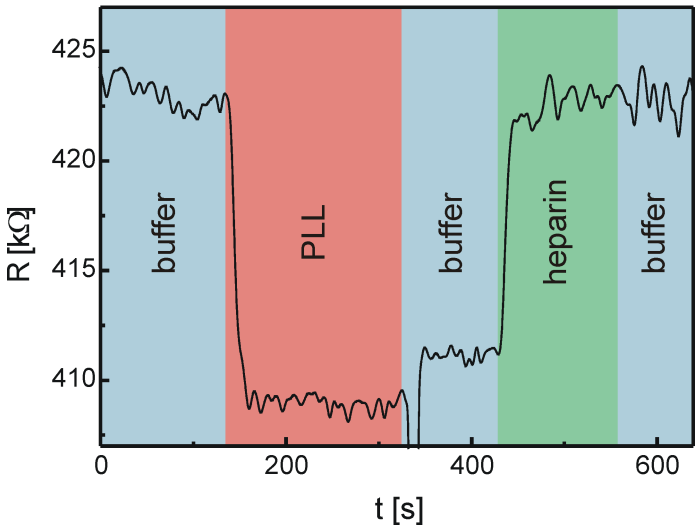

Figure 4.29: Heparin (50 μg/ml) is bound to a PLL coated sensor surface. The adsorption of the strongly negatively charged heparin leads to an increase of sheet resistance and thus to a decrease of surface potential.

itively charged and can be used likewise for the immobilization of the negatively charged heparin. The PLL coated SOI sensor allows for the detection of the negatively charged heparin down to concentrations of 0.5 μg/ml. In Fig. 4.29 the detection of 50 μg/ml heparin (in 10 mM Tris containing 50 mM NaCl at pH 7.4, Sigma-Aldrich) is shown, leading to a decrease of the surface potential of 8.5 mV. This corresponds to the maximum signal obtained, hence the surface is saturated with heparin.

Disaccharide vs. Polysaccharide Detection The enzyme heparinase I (EC 4.2.2.7, from *flavobacterium heparinum*) cleaves heparin selectively, via an elimination mechanism, at the linkages between hexosamines and O-sulfated iduronic acids, yielding mainly disaccharides [92]. As in the case of trypsin, a polyelectrolyte which strongly binds to the sensor surface is cleaved. For heparinase detection, the dimeric product is required to bind to the sensor surface with a lower affinity as compared to the polysaccharide heparin. This

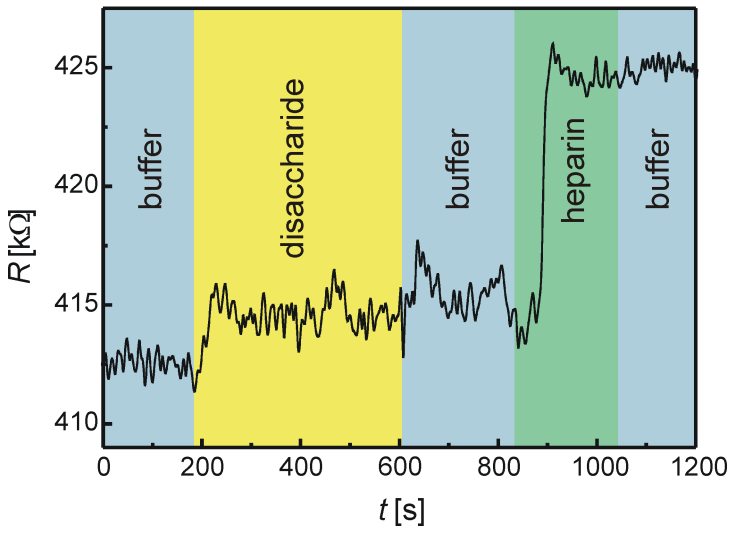

Figure 4.30: A solution of heparin disaccharide I S (10 μg/ml) only slightly increases the sheet resistance whereas the binding of heparin (5 μg/ml) leads to a significant increase.

prerequisite was tested comparing the binding of a commercially available disaccharide (heparin disaccharide I S, Sigma-Aldrich) with the binding of polymeric heparin. The used disaccharide is the typical product of heparinase I. Fig. 4.30 shows the binding of a heparin disaccharide (10 μg/ml in Tris) to a PLL coated surface. Only a slight increase in sheet resistance corresponding to a decrease of surface potential of 1.8 mV is observed. In contrast, a 5 μg/ml heparin solution (half the concentration of the disaccharide) leads to a significant increase in sheet resistance corresponding to a decrease of surface potential of 7.7 mV. Thus, the product of heparinase I binds to the PLL-covered sensor with a lower affinity as compared to its substrate heparin, which opens up a means of heparinase detection.

Heparinase Detection. Interestingly, in an experiment, where a solution of heparinase I (0.04 International Units (I.U.) per ml in 10 mM Tris containing 50 mM NaCl and 4 mM $CaCl_2$ at pH 7.4, Sigma-Aldrich) was directly added to a heparin coated sensor, the sheet resistance was not changed. Thus, the activity of heparinase I is not detectable when the substrate is immobilized to the sensor surface. This is in agreement with the finding that heparinase I will degrade heparin in solution, but not in blood, where heparin is bound to thrombin and thus is unavailable to the heparinase enzyme [93]. To detect the activity of the enzyme in solution, heparinase I was incubated with a 5 μg/ml heparin solution in 10 mM Tris containing 50 mM NaCl and 4 mM $CaCl_2$ at pH 7.4 for 1 h at 37°C. The final heparinase I concentration in the reaction mixture was $1.6 \cdot 10^{-3}$ I.U./ml. Afterwards, the solution was added to a PLL coated chip (Fig. 4.31), which resulted in an increase of the

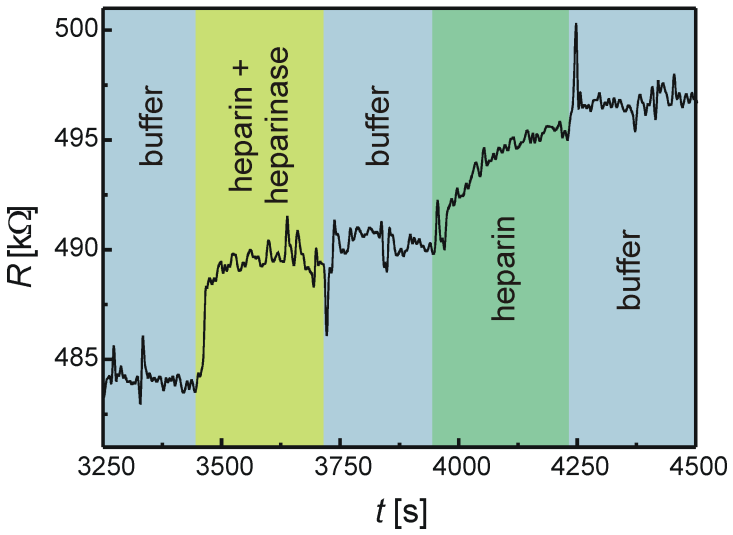

Figure 4.31: Heparin solution which had been incubated with heparinase I was added to a PLL covered sensor chip. The observed surface potential change is reduced by a factor of two as a consequence of heparinase I activity. Next, an untreated heparin solution was injected, demonstrating that the sensor surface was not yet fully covered with heparin.

sheet resistance corresponding to a surface potential decrease of 4.5 mV. Thus, the total signal decreased by a factor of approximately two by heparinase I digestion as compared to the untreated heparin solution of equivalent concentration (cf. Fig. 4.30). Finally, a solution containing 5 μg/ml heparin was injected, which resulted in a further increase of the sheet resistance corresponding to a surface potential decrease of 5.0 mV, leading to a saturation of the sensor surface with heparin.

Conclusion. We have found that the activity of heparinase I in solution can be detected by the sensor. However, it was not possible to detect the activity of heparinase I when the substrate is immobilized on the sensor surface. This is in contrast to the results obtained for trypsin, where the activity can easily be detected online at the surface. Either, surface bound heparin is not accessible as a substrate for heparinase I as indicated by Ref. [93], the enzyme is inactivated by the surface proximity, or the incubation temperature and time are too low. To clarify this, a different method of heparin immobilization could be employed. For this, it is crucial to make sure that heparin is located close enough to the sensor surface to avoid screening of its charges. In principle, the measurement could be carried out at an ambient temperature of 37°C. However, the effect of a prolonged reaction time can only be analyzed when long-term drifts of the device can be sufficiently controlled.

4.4 Detection of Bovine Serum Albumin

In this section, we investigate the detection of the protein bovine serum albumin (BSA) by the SOI based sensor. As proteins are composed of charged as well as uncharged amino acids, they normally exhibit a significantly lower charge density as compared to the polyelectrolytes studied in the previous sections. Typically, proteins have a dimension of the same order of magnitude as the screening length in buffers of physiological ionic strength. Therefore, we assume that the charge distribution and orientation relative to the sensor surface is crucial for their detection. Charges that are close to the surface have a higher contribution to the sensor signal as compared to charges farther away from the surface, which are partially or completely screened.

Experimental Procedure. BSA was adsorbed to the blank silicon oxide sensor surface in various concentrations ranging from 0.01 mg/ml to 10 mg/ml. BSA (minimum 98%) was purchased from Sigma-Aldrich. Solutions of various BSA concentrations were prepared by direct dissolution in 10 mM Tris buffer at pH 7.5 containing 50 mM NaCl. The BSA solutions were injected into the flow chamber starting with the lowest concentration. After obtaining a stable sensor signal, the chamber was rinsed with Tris buffer. When a stable signal was obtained, the procedure was repeated with a higher BSA concentration. For comparison, the adsorption of BSA was also studied by ellipsometry. Silicon wafers were coated with BSA solutions for three minutes. Afterwards, the wafers were rinsed with Millipore water and dried in a nitrogen stream.

Results and Interpretation. Fig. 4.32(a) shows the obtained film thickness as a function of BSA concentration. The maximum thickness (2 nm) of the dried film was obtained for 10 mg/ml. Similarly, an increase of the surface potential change with increasing protein concentration is found, as shown in Fig. 4.32(b), with a maximum value of 7.2 ± 1.6 mV. However, from the negative charge of the protein (approximately 15 e^- per molecule at neutral pH) we would expect a decrease of the surface potential and not an increase as it is observed. One could think of a dielectric effect caused by the adsorption of a protein layer with a dielectric constant lower than that of the bulk electrolyte solution. However, when the surface is negatively charged, this should lead to a decrease in the surface potential. Therefore, the observed increase cannot be attributed to a dielectric effect. Alternatively, the increase of the surface potential could be ascribed to a dipole moment of the adsorbed layer as a consequence of an oriented protein adsorption. Using the capacitor model for one charged layer including screening (section 4.1.2) we can estimate whether this hypothesis is reasonable. Therefore, we assume that the charges of the proteins are located in two planes: positive charges in the plane of the sensor surface and negative charges in a plane

at a distance d from the sensor surface (Fig. 4.32(b) inset). As the crystal structure of BSA is not available, we have instead used the structure of the human homologue, human serum albumin (HSA), in the following. HSA shares 90% sequence homology with BSA. Using the "Web Server to Calculate Dipole Moments of Proteins" (Clifford Felder and Joel Sussman, Dept. of Structural Biology Weizmann Institute, 761000 Rehovot, Israel, http://bioportal.weizmann.ac.il/dipol/) HSA (Protein Data Bank ID 1e7i [94]) we find a total of 97 negatively charged and 82 positively charged residues. When we assume a maximum surface density for BSA of 60 nm^2 per molecule [95], the capacitor model depicted in the inset of Fig. 4.32(b) allows us to calculate the potential change evoked by the oriented adsorption of the protein. A separation of only 20 negatively charged residues and 5 positively charged residues at a distance of 2.1 nm, positive residues pointing towards the negative silicon oxide, can result in an increase of the surface potential of approximately 7 mV assuming that the bulk screening length and dielectric constant also apply to the protein layer. This is in good agreement with the value obtained from the measurements. This charge distribution corresponds to a dipole moment of approximately 1400 Debye, which is in the same order of magnitude as the value given by the Web Server (1233 Debye) with respect to the center of mass of the protein. Thus, the increase of the surface potential caused by the adsorption of a protein that is negatively charged in total can be explained within the model by the directed adsorption of a dipolar molecule. A similar effect has been observed using a carbon nanotube field effect device [96]. In this work, a conductance change opposite from what could be expected based on molecular charge was found, indicating that it is not the net charge of the protein alone that determines the device response. In section 4.2.7, an increase of the surface potential was detected for the adsorption of the neutral polymer PNMVA (Fig. 4.20). For this homopolymer, a dipolar effect can be excluded, however variations of the local pH and changes in the specific adsorption of ions have been discussed. These effects may as well contribute to the detection of BSA adsorption. To distinguish these effects, changes in the local pH could possibly be detected by the incorporation of a pH-sensitive dye as described for polyelectrolyte multilayers [21]. The specific adsorption of ions could be analyzed using different cations, though this could alter the adsorption of the proteins.

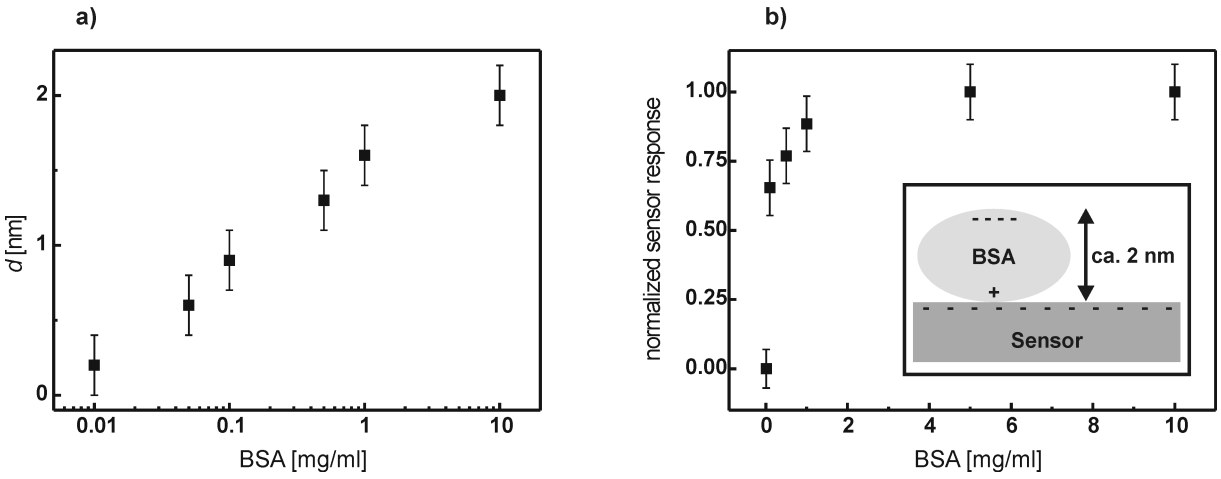

Figure 4.32: (a) The thickness of BSA films on top of a silicon wafer was determined by ellipsometry. Samples were dried in a nitrogen stream before measurement. (b) The adsorption of BSA to the blank silicon oxide sensor surface at concentrations from 0.01 mg/ml to 10 mg/ml is shown. The sensor response was normalized with respect to the maximum value obtained for saturation (7.2 ± 1.6 mV). The inset displays the dipolar adsorption of BSA as assumed in the capacitor model (section 4.1.2).

5 Outlook

In this thesis, a field effect sensor based on SOI technology has been employed for the detection of synthetic as well as biological polyelectrolytes. The adsorption of these polymers is readily detected due to their high charge density. We have developed a theoretical description, which quantitatively describes the response of the sensor device. This capacitor model was successfully applied to the detection of polyelectrolyte multilayers (PEMs) giving further insight into their basic physical properties. In the meantime, our model has also been further employed for the analysis of the adsorption of PEMs to a carbon nanotube field effect device as described in Ref. [97]. Still, there are observations such as the signal caused by the adsorption of a neutral polymer, which cannot be explained within the model. Variations of the local pH at the sensor surface as well as the specific adsorption of ions, which have been discussed as possible explanations, are not included in the model. However, these effects are taken into account in Ref. [52, 63] for the description of the pH, ion and charge sensitivity of a SOI device. Combining this numerical approach with the analytical model presented in this work could lead to an improved understanding of the detection of polyelectrolyte multilayers and other complex systems.

The electrical detection of the adsorption of bovine serum albumin (BSA) to the sensor surface could be demonstrated in this thesis. A surface potential change opposite to what could be expected based on the net molecular charge was observed. This effect can be explained within our capacitor model in terms of a dipolar orientation of the bound molecules. Thus, it is not the net charge of the molecule alone but also the charge distribution which determines the sensor signal at a certain ionic strength of the buffer solution. The influence of the exact charge distribution could possibly be investigated using polyproline helices [98], which contain charged amino acids at defined positions. A histidine linker can be used for the immobilization of such peptides [6]. Measuring the X-ray reflectivity and the electrical response of the sensor in parallel should further lead towards a better understanding of the distance dependency of the sensor signal. For this, we have already demonstrated that the SOI substrate is suitable for X-ray reflectivity (see section 4.2.3).

We have used the SOI device as a biosensor for the detection of enzymatic activity exploiting the good detectability of biological polyelectrolyte substrates. Enzymes were chosen which cleave polyelectrolytes into smaller molecules. These fragments desorb from the sensor surface, thereby changing the surface charge and thus the surface potential. Any enzyme which can change the charge at the sensor surface can potentially be detected by the field effect sensor. It has been shown that the sensor surface can be functionalized with

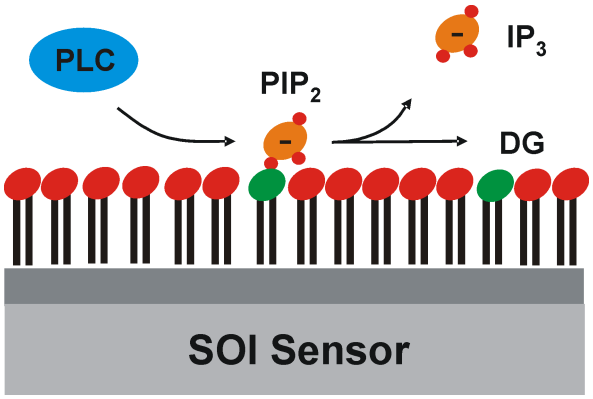

Figure 5.1: The enzyme PLC cleaves the phospholipid PIP_2 of the plasma membrane. The neutral lipid DAG is left in the membrane, whereas the charged molecule IP_3 is released into the solution. The thereby caused change in surface charge could possibly be detected by a field effect device such as the SOI sensor.

lipid membranes, on which charging and discharging can be observed quantitatively [6]. Phospholipase C (PLC) is an enzyme, which cleaves the phospholipid phosphatidylinositol 4,5-bisphosphate (PIP_2) contained in the plasma membrane [99] as depicted in Fig. 5.1. Charged inositol 1,4,5-triphosphate (IP_3) is released into the solution, while the neutral lipid diacylglycerol (DAG) remains in the plasma membrane. If such a lipid membrane containing PIP_2 was brought onto the sensor surface, the activity of PLC could possibly be observed in real-time as a decrease of the surface potential.

Initially, biosensor development has focused on enzyme-based systems [100]. In the mean time, also antibody-based biosensors have gained interest. Antibodies are particularly useful in measuring small molecules. However, with most sensor types the direct detection of the binding of small molecules is unfavorable, as only low signals can be obtained (Fig. 5.2(a)). Thus, it would be advantageous to use a competitive assay format (Fig. 5.2(b)), assuming that the binding of large antibodies can be detected more easily. In this detection format, small analyte molecules in solution can be measured by the amount of antibody binding to the analyte-functionalized surface. A high concentration of analyte in solution will result in a low signal as only few antibodies are available at the surface. A first study of antibody detection using the SOI device has been presented in Ref. [52]. For a further amplification of the sensor signal, a charged colloidal probe could be attached to a secondary antibody (Fig. 5.2(c)). Alternatively, oligonucleotide aptamers could be used in place of antibodies. These molecules are evolutionary engineered through *in vitro* selection to bind to a specific target molecule [101]. Aptamers offer advantages over antibodies as they consist of highly charged nucleic acids and can be easily produced by

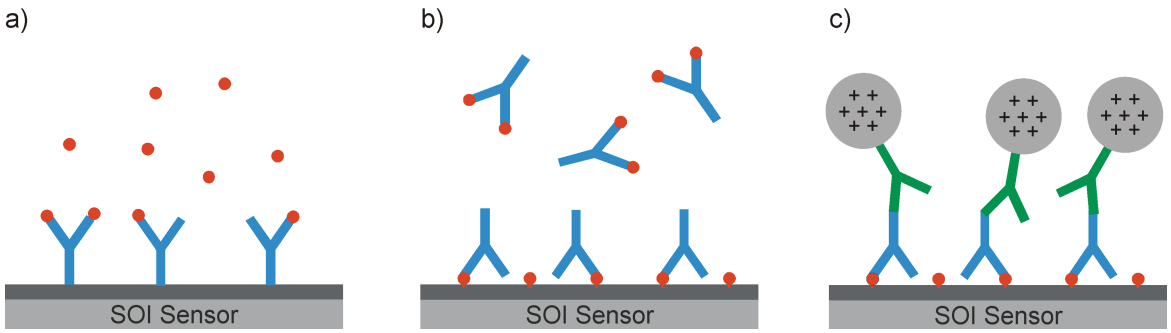

Figure 5.2: (a) For the direct detection of analyte molecules, antibodies are immobilized at the sensor surface. (b) In a competitive assay format, the concentration of analyte in solution determines the amount of antibody which can bind to the analyte-functionalized surface. This is favorable as compared to (a), because the large antibodies give a higher signal. (c) The signal could be further amplified using a secondary antibody carrying a charged colloidal probe.

chemical synthesis. It has previously been demonstrated that oligonucleotides are readily detected by field effect devices [2, 3]. Therefore, aptamer-based assay formats are highly promising for application with the SOI sensor.

A Basic Model for Multiple Charged Layers: Derivation of the Expression for U_1

In this appendix, we present the detailed derivation of the expression for the surface potential of a field-effect device functionalized with multiple charged layers as described in section 4.1.1. We use the same notation as introduced in this section. The total voltage U_{tot} is given by the sum of all potential differences

$$\sum_{i=1}^{N} E_i d_i = U_{\text{tot}}, \tag{A.1}$$

where E_i is the electric field in the respective area. We apply Gauss' law for each charged layer ($E_0 = E_{N+1} = 0$)

$$\varepsilon_{i+1} E_{i+1} - \varepsilon_i E_i = \sigma_i \qquad \text{for } i = 0, 1, \ldots, N. \tag{A.2}$$

Eq. (A.1) and Eq. (A.2) constitute a system of $N+2$ linear equations for the N unknown variables E_i ($i = 1, \ldots, N$) and the 2 unknown variables σ_0, σ_N. All other surface charges are fix. The voltage $U_1 = E_1 d_1$, which drops over the sensor device, determines the charge carrier concentration and thus the sheet resistance. We want to understand how charged layers at the sensor surface influence the sheet resistance, which is a function of U_1, so we have to solve for E_1 or U_1, respectively. From Eq. (A.1) we know that

$$E_1 d_1 + \sum_{i=2}^{N} E_i d_i = U_{\text{tot}}, \tag{A.3}$$

i.e.

$$U_1 = U_{\text{tot}} - \sum_{i=2}^{N} E_i d_i, \tag{A.4}$$

and we have to find expressions for E_i, $i = 2, \ldots, N$. From Eq. (A.2) we find

$$\varepsilon_i E_i - \varepsilon_{i-1} E_{i-1} = \sigma_{i-1}, \tag{A.5}$$

which by recursion leads to

$$E_i = \frac{1}{\varepsilon_i} \sum_{j=0}^{i-1} \sigma_j. \tag{A.6}$$

We insert Eq. (A.6) into Eq. (A.4) and obtain

$$\begin{aligned} U_1 &= U_{\text{tot}} - \sum_{i=2}^{N} \frac{d_i}{\varepsilon_i} \sum_{j=0}^{i-1} \sigma_j \\ &= U_{\text{tot}} - \sum_{i=2}^{N} \frac{d_i}{\varepsilon_i} \left(\sum_{j=1}^{i-1} \sigma_j + \sigma_0 \right). \end{aligned} \tag{A.7}$$

With $U_1 = E_1 d_1 = \frac{\sigma_0}{\varepsilon_1} d_1$, i.e. $\sigma_0 = \frac{\varepsilon_1 U_1}{d_1}$ we find

$$\begin{aligned} U_1 &= U_{\text{tot}} - \sum_{i=2}^{N} \frac{d_i}{\varepsilon_i} \left(\sum_{j=1}^{i-1} \sigma_j + \frac{\varepsilon_1 U_1}{d_1} \right) \\ &= U_{\text{tot}} - \sum_{i=2}^{N} \frac{d_i}{\varepsilon_i} \sum_{j=1}^{i-1} \sigma_j - U_1 \frac{\varepsilon_1}{d_1} \sum_{i=2}^{N} \frac{d_i}{\varepsilon_i}, \end{aligned} \tag{A.8}$$

so we can solve for U_1

$$\begin{aligned} U_1 &= \frac{d_1}{\varepsilon_1} \frac{1}{\sum_{i=1}^{N} \frac{d_i}{\varepsilon_i}} \left(U_{\text{tot}} - \sum_{i=2}^{N} \frac{d_i}{\varepsilon_i} \sum_{j=1}^{i-1} \sigma_j \right) \\ &= \frac{d_1}{\varepsilon_1} \frac{1}{\sum_{i=1}^{N} \frac{d_i}{\varepsilon_i}} \left(U_{\text{tot}} - \sum_{i=1}^{N} \frac{d_i}{\varepsilon_i} \sum_{j=1}^{i-1} \sigma_j \right). \end{aligned} \tag{A.9}$$

B Capacitor Model for One Charged Layer Including Screening: Derivation of the Expression for U_1

In this appendix, we present the detailed derivation of the expression for the surface potential of a field-effect device functionalized with one charged layer including screening by mobile ions as described in section 4.1.2. We use the same notation as introduced in this section. From the boundary conditions given in section 4.1.2 it follows that

$$A = 0, \qquad A' = -\frac{\sigma_0}{\varepsilon_1}, \tag{B.1}$$

$$B = U_{\text{tot}} - \frac{\sigma_L}{\varepsilon_L} x_L, \qquad B' = \frac{\sigma_L}{\varepsilon_L} \tag{B.2}$$

and

$$\begin{aligned} C\exp(-\kappa x_1) + D\exp(\kappa x_1) + \frac{\sigma_0}{\varepsilon_1}x_1 &= 0, && \text{(B.3)}\\ \varepsilon\kappa\left[-C\exp(-\kappa x_1) + D\exp(\kappa x_1)\right] + \sigma_0 &= -\sigma_1, && \text{(B.4)}\\ \frac{\sigma_L}{\varepsilon_L}x_2 + U_{\text{tot}} - \frac{\sigma_L}{\varepsilon_L}x_L - C\exp(-\kappa x_2) - D\exp(\kappa x_2) &= 0, && \text{(B.5)}\\ \sigma_L - \varepsilon\kappa\left[-C\exp(-\kappa x_2) + D\exp(\kappa x_2)\right] &= -\sigma. && \text{(B.6)} \end{aligned}$$

Combining Eq. (B.3) with Eq. (B.4) and Eq. (B.5) with Eq. (B.6), respectively, we find for C

$$C = \frac{1}{2}\left[-\frac{\sigma_0}{\varepsilon_1}x_1 + \frac{1}{\varepsilon\kappa}(\sigma_1+\sigma_0)\right]\exp(\kappa x_1) \tag{B.7}$$

and

$$C = \frac{1}{2}\left[U_{\text{tot}} - \frac{\sigma_L}{\varepsilon_L}d_L - \frac{1}{\varepsilon\kappa}(\sigma+\sigma_L)\right]\exp(\kappa x_2)\,. \tag{B.8}$$

Accordingly, we find for D

$$D = \frac{1}{2}\left[-\frac{\sigma_0}{\varepsilon_1}x_1 - \frac{1}{\varepsilon\kappa}(\sigma_1+\sigma_0)\right]\exp(-\kappa x_1) \tag{B.9}$$

and

$$D = \frac{1}{2}\left[U_{\text{tot}} - \frac{\sigma_L}{\varepsilon_L}d_L + \frac{1}{\varepsilon\kappa}(\sigma+\sigma_L)\right]\exp(-\kappa x_2)\,. \tag{B.10}$$

We can eliminate C and D

$$C = \frac{1}{2}\left[U_{\text{tot}} - \frac{\sigma_L}{\varepsilon_L}d_L - \frac{1}{\varepsilon\kappa}(\sigma+\sigma_L)\right]\exp(\kappa x_2) = \frac{1}{2}\left[-\frac{\sigma_0}{\varepsilon_1}x_1 + \frac{1}{\varepsilon\kappa}(\sigma_1+\sigma_0)\right]\exp(\kappa x_1) \tag{B.11}$$

$$D = \frac{1}{2}\left[U_{\text{tot}} - \frac{\sigma_L}{\varepsilon_L}d_L + \frac{1}{\varepsilon\kappa}(\sigma+\sigma_L)\right]\exp(-\kappa x_2) = \frac{1}{2}\left[-\frac{\sigma_0}{\varepsilon_1}x_1 - \frac{1}{\varepsilon\kappa}(\sigma_1+\sigma_0)\right]\exp(-\kappa x_1) \tag{B.12}$$

and obtain two equations for σ_0 and σ_L

$$\begin{aligned} &\left(\tfrac{d_L}{\varepsilon_L} - \tfrac{1}{\varepsilon\kappa}\right)\exp(-\kappa x_2)\left[\sigma_0\left(\tfrac{x_1}{\varepsilon_1} - \tfrac{1}{\varepsilon\kappa}\right)\exp(\kappa x_1) - \sigma_L\left(\tfrac{d_L}{\varepsilon_L} + \tfrac{1}{\varepsilon\kappa}\right)\exp(\kappa x_2)\right]\\ = \;&\left(\tfrac{d_L}{\varepsilon_L} - \tfrac{1}{\varepsilon\kappa}\right)\exp(-\kappa x_2)\left[-U_{\text{tot}}\exp(\kappa x_2) + \tfrac{1}{\varepsilon\kappa}\sigma\exp(\kappa x_2) + \tfrac{1}{\varepsilon\kappa}\sigma_1\exp(\kappa x_1)\right] \end{aligned} \tag{B.13}$$

and

$$\begin{aligned} & \left(\frac{d_L}{\varepsilon_L}+\frac{1}{\varepsilon\kappa}\right)\exp(\kappa x_2)\left[\sigma_0\left(\frac{x_1}{\varepsilon_1}+\frac{1}{\varepsilon\kappa}\right)\exp(-\kappa x_1)-\sigma_L\left(\frac{d_L}{\varepsilon_L}-\frac{1}{\varepsilon\kappa}\right)\exp(-\kappa x_2)\right] \\ = & \left(\frac{d_L}{\varepsilon_L}+\frac{1}{\varepsilon\kappa}\right)\exp(\kappa x_2)\left[-U_{\text{tot}}\exp(-\kappa x_2)-\frac{1}{\varepsilon\kappa}\sigma\exp(-\kappa x_2)-\frac{1}{\varepsilon\kappa}\sigma_1\exp(-\kappa x_1)\right]. \end{aligned} \tag{B.14}$$

Now, we can eliminate σ_L and obtain an expression for σ_0

$$\sigma_0=\frac{1}{\varepsilon\kappa}\frac{2U_{\text{tot}}+2\sigma\frac{d_L}{\varepsilon_L}+\sigma_1\left[\exp(-\kappa d)\left(\frac{d_L}{\varepsilon_L}-\frac{1}{\varepsilon\kappa}\right)+\exp(\kappa d)\left(\frac{d_L}{\varepsilon_L}+\frac{1}{\varepsilon\kappa}\right)\right]}{\left(\frac{d_L}{\varepsilon_L}-\frac{1}{\varepsilon\kappa}\right)\exp(-\kappa d)\left(\frac{x_1}{\varepsilon_1}-\frac{1}{\varepsilon\kappa}\right)-\left(\frac{d_L}{\varepsilon_L}+\frac{1}{\varepsilon\kappa}\right)\exp(\kappa d)\left(\frac{x_1}{\varepsilon_1}+\frac{1}{\varepsilon\kappa}\right)}. \tag{B.15}$$

U_1 is then obtained from σ_0 as follows:

$$\begin{aligned} U_1 &= \psi_{(\text{i})}(d_1)-\psi_{(\text{i})}(0)=-\frac{\sigma_0}{\varepsilon_1}d_1 \\ &= -\frac{d_1}{\varepsilon_1}\frac{1}{\varepsilon\kappa}\frac{2U_{\text{tot}}+2\sigma\frac{d_L}{\varepsilon_L}+\sigma_1\left[\exp(-\kappa d)\left(\frac{d_L}{\varepsilon_L}-\frac{1}{\varepsilon\kappa}\right)+\exp(\kappa d)\left(\frac{d_L}{\varepsilon_L}+\frac{1}{\varepsilon\kappa}\right)\right]}{\left(\frac{d_L}{\varepsilon_L}-\frac{1}{\varepsilon\kappa}\right)\exp(-\kappa d)\left(\frac{x_1}{\varepsilon_1}-\frac{1}{\varepsilon\kappa}\right)-\left(\frac{d_L}{\varepsilon_L}+\frac{1}{\varepsilon\kappa}\right)\exp(\kappa d)\left(\frac{x_1}{\varepsilon_1}+\frac{1}{\varepsilon\kappa}\right)}. \end{aligned} \tag{B.16}$$

C Capacitor Model for the Description of Polyelectrolyte Multilayers: Surface Charges

In this appendix, we present the detailed derivation of the expression for the surface potential of a field-effect device functionalized with polyelectrolyte multilayers, where the charges are situated on plates with the surface charge density of $\pm\sigma$. The model is described in the first part of section 4.1.3. We use the same notation as introduced there. From the boundary conditions given in section 4.1.3 for surface charges it follows that

$$A=0, \qquad A'=-\frac{\sigma_0}{\varepsilon_1}, \tag{C.1}$$

$$B=U_{\text{tot}}-\frac{\sigma_L}{\varepsilon_L}x_L, \qquad B'=\frac{\sigma_L}{\varepsilon_L}, \tag{C.2}$$

and

$$C_1 \exp(-\kappa x_1) + D_1 \exp(\kappa x_1) = -\frac{\sigma_0}{\varepsilon_1} x_1, \tag{C.3}$$

$$-C_1 \exp(-\kappa x_1) + D_1 \exp(\kappa x_1) = -\frac{1}{\varepsilon\kappa}(\sigma_1 + \sigma_0), \tag{C.4}$$

$$C_N \exp(-\kappa x_{N+1}) + D_N \exp(\kappa x_{N+1}) = U_{\text{tot}} - \frac{\sigma_L}{\varepsilon_L} d_L, \tag{C.5}$$

$$-C_N \exp(-\kappa x_{N+1}) + D_N \exp(\kappa x_{N+1}) = -\frac{1}{\varepsilon\kappa}\left((-1)^N \sigma - \sigma_L\right). \tag{C.6}$$

To simplify matters we use the following matrix form

$$\begin{pmatrix} e^{-\kappa x_1} & e^{\kappa x_1} \\ -e^{-\kappa x_1} & e^{\kappa x_1} \end{pmatrix} \begin{pmatrix} C_1 \\ D_1 \end{pmatrix} = \begin{pmatrix} -\frac{\sigma_0}{\varepsilon_1} x_1 \\ -\frac{1}{\varepsilon\kappa}(\sigma_1 + \sigma_0) \end{pmatrix}, \tag{C.7}$$

$$\begin{pmatrix} e^{-\kappa x_{N+1}} & e^{\kappa x_{N+1}} \\ -e^{-\kappa x_{N+1}} & e^{\kappa x_{N+1}} \end{pmatrix} \begin{pmatrix} C_N \\ D_N \end{pmatrix} = \begin{pmatrix} U_{\text{tot}} - \frac{\sigma_L}{\varepsilon_L} d_L \\ -\frac{1}{\varepsilon\kappa}\left((-1)^N \sigma - \sigma_L\right) \end{pmatrix} \tag{C.8}$$

or

$$\begin{aligned} \begin{pmatrix} C_1 \\ D_1 \end{pmatrix} &= \frac{1}{2} \begin{pmatrix} e^{\kappa x_1} & -e^{\kappa x_1} \\ e^{-\kappa x_1} & e^{-\kappa x_1} \end{pmatrix} \begin{pmatrix} -\frac{\sigma_0}{\varepsilon_1} x_1 \\ -\frac{1}{\varepsilon\kappa}(\sigma_1 + \sigma_0) \end{pmatrix} \\ &= \frac{1}{2} \begin{pmatrix} -x_1 \frac{\sigma_0}{\varepsilon_1} e^{\kappa x_1} + \frac{1}{\kappa\varepsilon}(\sigma_0 + \sigma_1) e^{\kappa x_1} \\ -x_1 \frac{\sigma_0}{\varepsilon_1} e^{-\kappa x_1} - \frac{1}{\kappa\varepsilon} e^{-\kappa x_1}(\sigma_0 + \sigma_1) \end{pmatrix}, \end{aligned} \tag{C.9}$$

$$\begin{aligned} \begin{pmatrix} C_N \\ D_N \end{pmatrix} &= \frac{1}{2} \begin{pmatrix} e^{\kappa x_{N+1}} & -e^{\kappa x_{N+1}} \\ e^{-\kappa x_{N+1}} & e^{-\kappa x_{N+1}} \end{pmatrix} \begin{pmatrix} U_{\text{tot}} - \frac{\sigma_L}{\varepsilon_L} d_L \\ -\frac{1}{\varepsilon\kappa}\left((-1)^N \sigma - \sigma_L\right) \end{pmatrix} \\ &= \frac{1}{2} \begin{pmatrix} \frac{1}{\kappa\varepsilon} e^{\kappa x_{N+1}} \left(-\sigma_L + \sigma(-1)^N\right) + e^{\kappa x_{N+1}} \left(U_{\text{tot}} - \frac{\sigma_L}{\varepsilon_L} d_L\right) \\ -\frac{1}{\kappa\varepsilon} e^{-\kappa x_{N+1}} \left(-\sigma_L + \sigma(-1)^N\right) + e^{-\kappa x_{N+1}} \left(U_{\text{tot}} - \frac{\sigma_L}{\varepsilon_L} d_L\right) \end{pmatrix}. \end{aligned} \tag{C.10}$$

For $n = 2, \ldots, N$ we find

$$C_n e^{-\kappa x_n} + D_n e^{\kappa x_n} - C_{n-1} e^{-\kappa x_n} - D_{n-1} e^{\kappa x_n} = 0, \tag{C.11}$$

$$-C_n e^{-\kappa x_n} + D_n e^{\kappa x_n} + C_{n-1} e^{-\kappa x_n} - D_{n-1} e^{\kappa x_n} = \frac{(-1)^{n-1}}{\varepsilon\kappa}\sigma. \tag{C.12}$$

This can also be written in matrix form according to

$$\begin{aligned} & \begin{pmatrix} \exp(-\kappa x_n) & \exp(\kappa x_n) \\ -\exp(-\kappa x_n) & \exp(\kappa x_n) \end{pmatrix} \begin{pmatrix} C_n \\ D_n \end{pmatrix} \\ = & \begin{pmatrix} \exp(-\kappa x_n) & \exp(\kappa x_n) \\ -\exp(-\kappa x_n) & \exp(\kappa x_n) \end{pmatrix} \begin{pmatrix} C_{n-1} \\ D_{n-1} \end{pmatrix} + \begin{pmatrix} 0 \\ \frac{(-1)^{n-1}}{\varepsilon\kappa}\sigma \end{pmatrix}. \end{aligned} \tag{C.13}$$

Now we solve for C_n and D_n

$$\begin{aligned} \begin{pmatrix} C_n \\ D_n \end{pmatrix} &= \begin{pmatrix} C_{n-1} \\ D_{n-1} \end{pmatrix} + \begin{pmatrix} \exp(-\kappa x_n) & \exp(\kappa x_n) \\ -\exp(-\kappa x_n) & \exp(\kappa x_n) \end{pmatrix}^{-1} \begin{pmatrix} 0 \\ \frac{(-1)^{n-1}}{\varepsilon\kappa}\sigma \end{pmatrix} \\ &= \begin{pmatrix} C_{n-1} \\ D_{n-1} \end{pmatrix} + \frac{1}{2} \begin{pmatrix} \exp(\kappa x_n) & -\exp(\kappa x_n) \\ \exp(-\kappa x_n) & \exp(-\kappa x_n) \end{pmatrix} \begin{pmatrix} 0 \\ \frac{(-1)^{n-1}}{\varepsilon\kappa}\sigma \end{pmatrix} \\ &= \begin{pmatrix} C_{n-1} \\ D_{n-1} \end{pmatrix} + \frac{1}{2}\frac{(-1)^{n-1}}{\varepsilon\kappa}\sigma \begin{pmatrix} -\exp(\kappa x_n) \\ \exp(-\kappa x_n) \end{pmatrix}. \end{aligned} \tag{C.14}$$

Thus we obtain the following relation

$$\begin{pmatrix} C_{n+1} \\ D_{n+1} \end{pmatrix} = \begin{pmatrix} C_n \\ D_n \end{pmatrix} + \frac{1}{2}\frac{(-1)^n}{\varepsilon\kappa}\sigma \begin{pmatrix} -\exp(\kappa x_{n+1}) \\ \exp(-\kappa x_{n+1}) \end{pmatrix}, \qquad n = 1, \ldots, N-1 \tag{C.15}$$

which can be used to relate C_{n+1} and D_{n+1} to C_1 and D_1

$$\begin{pmatrix} C_{n+1} \\ D_{n+1} \end{pmatrix} = \begin{pmatrix} C_1 \\ D_1 \end{pmatrix} + \frac{1}{2}\frac{\sigma}{\kappa\varepsilon}\sum_{k=1}^{n}(-1)^k \begin{pmatrix} -\exp(\kappa x_{k+1}) \\ \exp(-\kappa x_{k+1}) \end{pmatrix}, \tag{C.16}$$

and also C_N and D_N to C_1 and D_1

$$\begin{pmatrix} C_N \\ D_N \end{pmatrix} = \begin{pmatrix} C_1 \\ D_1 \end{pmatrix} + \frac{1}{2}\frac{\sigma}{\kappa\varepsilon}\sum_{k=1}^{N-1}(-1)^k \begin{pmatrix} -\exp(\kappa x_{k+1}) \\ \exp(-\kappa x_{k+1}) \end{pmatrix}. \tag{C.17}$$

Now we want to determine σ_0. Therefore we need to evaluate the sum

$$\sum_{k=1}^{N-1}(-1)^k \begin{pmatrix} -\exp(\kappa x_{k+1}) \\ \exp(-\kappa x_{k+1}) \end{pmatrix}.$$

With

$$x_n = d_1 + (n-1)\,d \tag{C.18}$$

we find

$$\sum_{k=1}^{N-1}(-1)^k \exp\left(-\kappa x_{k+1}\right) = \exp\left(-\kappa d_1\right) \sum_{n=1}^{N-1}\left(-\exp\left(-\kappa d\right)\right)^n . \tag{C.19}$$

Using

$$\sum_{n=1}^{N-1}\left(-\exp\left(x\right)\right)^n = -\frac{\exp\left(x\right)+(-1)^N \exp\left(Nx\right)}{1+\exp\left(x\right)} \tag{C.20}$$

we find

$$\sum_{i=1}^{N-1}(-1)^i \exp\left(-\kappa x_{i+1}\right) = -\exp\left(-\kappa d_1\right) \frac{\exp\left(-\kappa d\right)+(-1)^N \exp\left(-\kappa dN\right)}{1+\exp\left(-\kappa d\right)}. \tag{C.21}$$

This yields

$$\sum_{k=1}^{N-1}(-1)^k \begin{pmatrix} -\exp\left(\kappa x_{k+1}\right) \\ \exp\left(-\kappa x_{k+1}\right) \end{pmatrix} = \begin{pmatrix} \exp\left(\kappa d_1\right) \frac{\exp(\kappa d)+(-1)^N \exp(\kappa dN)}{1+\exp(\kappa d)} \\ -\exp\left(-\kappa d_1\right) \frac{\exp(-\kappa d)+(-1)^N \exp(-\kappa dN)}{1+\exp(-\kappa d)} \end{pmatrix}. \tag{C.22}$$

When we insert Eq. (C.22) into Eq. (C.17) we obtain

$$\begin{pmatrix} C_N \\ D_N \end{pmatrix} = \begin{pmatrix} C_1 \\ D_1 \end{pmatrix} + \frac{1}{2}\frac{1}{\kappa}\frac{\sigma}{\varepsilon} \begin{pmatrix} \exp\left(\kappa d_1\right) \frac{\exp(\kappa d)+(-1)^N \exp(\kappa dN)}{1+\exp(\kappa d)} \\ -\exp\left(-\kappa d_1\right) \frac{\exp(-\kappa d)+(-1)^N \exp(-\kappa dN)}{1+\exp(-\kappa d)} \end{pmatrix} \tag{C.23}$$

and using the expressions for $\begin{pmatrix} C_N \\ D_N \end{pmatrix}$ and $\begin{pmatrix} C_1 \\ D_1 \end{pmatrix}$ this leads to

$$\begin{aligned} &\begin{pmatrix} \frac{1}{\kappa\varepsilon} e^{\kappa x_{N+1}} \left(-\sigma_L + \sigma\left(-1\right)^N\right) + e^{\kappa x_{N+1}} \left(U_{\text{tot}} - \frac{\sigma_L}{\varepsilon_L} d_L\right) \\ -\frac{1}{\kappa\varepsilon} e^{-\kappa x_{N+1}} \left(-\sigma_L + \sigma\left(-1\right)^N\right) + e^{-\kappa x_{N+1}} \left(U_{\text{tot}} - \frac{\sigma_L}{\varepsilon_L} d_L\right) \end{pmatrix} \\ &= \begin{pmatrix} -x_1 \frac{\sigma_0}{\varepsilon_1} e^{\kappa x_1} + \frac{1}{\kappa\varepsilon}\left(\sigma_0+\sigma_1\right) e^{\kappa x_1} \\ -x_1 \frac{\sigma_0}{\varepsilon_1} e^{-\kappa x_1} - \frac{1}{\kappa\varepsilon} e^{-\kappa x_1}\left(\sigma_0+\sigma_1\right) \end{pmatrix} + \frac{1}{\kappa}\frac{\sigma}{\varepsilon} \begin{pmatrix} e^{\kappa d_1} \frac{e^{\kappa d}+(-1)^N e^{\kappa dN}}{1+e^{\kappa d}} \\ -e^{-\kappa d_1} \frac{e^{-\kappa d}+(-1)^N e^{(-\kappa dN)}}{1+e^{(-\kappa d)}} \end{pmatrix}. \end{aligned} \tag{C.24}$$

To determine σ_0 we express this system of equations in matrix form according to

$$\begin{pmatrix} a_{11} & a_{12} \\ a_{21} & a_{22} \end{pmatrix} \begin{pmatrix} \sigma_0 \\ \sigma_L \end{pmatrix} = \begin{pmatrix} s_1 \\ s_2 \end{pmatrix}. \tag{C.25}$$

This results in

$$\begin{pmatrix} e^{\kappa x_1}\left(\frac{x_1}{\varepsilon_1}-\frac{1}{\kappa\varepsilon}\right) & -e^{\kappa x_{N+1}}\left(\frac{d_L}{\varepsilon_L}+\frac{1}{\kappa\varepsilon}\right) \\ e^{-\kappa x_1}\left(\frac{x_1}{\varepsilon_1}+\frac{1}{\kappa\varepsilon}\right) & -e^{-\kappa x_{N+1}}\left(\frac{d_L}{\varepsilon_L}-\frac{1}{\kappa\varepsilon}\right) \end{pmatrix} \begin{pmatrix} \sigma_0 \\ \sigma_L \end{pmatrix} = \begin{pmatrix} s_1 \\ s_2 \end{pmatrix} \tag{C.26}$$

with

$$\begin{aligned} \begin{pmatrix} s_1 \\ s_2 \end{pmatrix} &= \begin{pmatrix} \frac{1}{\kappa\varepsilon}\sigma_1 e^{\kappa x_1} - \frac{(-1)^N}{\kappa\varepsilon}\sigma e^{\kappa x_{N+1}} - e^{\kappa x_{N+1}}U_{\text{tot}} \\ -\frac{1}{\kappa\varepsilon}\sigma_1 e^{-\kappa x_1} + \frac{(-1)^N}{\kappa\varepsilon}\sigma e^{-\kappa x_{N+1}} - e^{-\kappa x_{N+1}}U_{\text{tot}} \end{pmatrix} \\ &\quad + \frac{1}{\kappa}\frac{\sigma}{\varepsilon}\begin{pmatrix} e^{\kappa d_1}\frac{e^{\kappa d}+(-1)^N e^{\kappa dN}}{1+e^{\kappa d}} \\ -e^{-\kappa d_1}\frac{e^{-\kappa d}+(-1)^N e^{-\kappa dN}}{1+e-\kappa d} \end{pmatrix}. \end{aligned} \tag{C.27}$$

Now, we multiply by the inverse

$$\begin{pmatrix} \sigma_0 \\ \sigma_L \end{pmatrix} = \begin{pmatrix} -e^{\kappa x_1}\left(\frac{1}{\kappa\varepsilon}-\frac{x_1}{\varepsilon_1}\right) & -e^{\kappa x_{N+1}}\left(\frac{1}{\kappa\varepsilon}+\frac{d_L}{\varepsilon_L}\right) \\ e^{-\kappa x_1}\left(\frac{1}{\kappa\varepsilon}+\frac{x_1}{\varepsilon_1}\right) & e^{-\kappa x_{N+1}}\left(\frac{1}{\kappa\varepsilon}-\frac{d_L}{\varepsilon_L}\right) \end{pmatrix}^{-1} \begin{pmatrix} s_1 \\ s_2 \end{pmatrix}, \tag{C.28}$$

so we can write σ_0 as follows:

$$\sigma_0 = \frac{\left(s_1 e^{-\kappa x_{N+1}}\left(-\frac{d_L}{\varepsilon_L}+\frac{1}{\kappa\varepsilon}\right)+s_2 e^{\kappa x_{N+1}}\left(\frac{d_L}{\varepsilon_L}+\frac{1}{\kappa\varepsilon}\right)\right)}{-\left(\frac{1}{\kappa\varepsilon}-\frac{x_1}{\varepsilon_1}\right)\left(\frac{1}{\kappa\varepsilon}-\frac{d_L}{\varepsilon_L}\right)e^{-\kappa Nd}+\left(\frac{1}{\kappa\varepsilon}+\frac{x_1}{\varepsilon_1}\right)\left(\frac{1}{\kappa\varepsilon}+\frac{d_L}{\varepsilon_L}\right)e^{\kappa Nd}}. \tag{C.29}$$

Finally, we use σ_0 to determine U_1

$$\begin{aligned} U_1 &= \psi_{(\mathrm{i})}(d_1) - \psi_{(\mathrm{i})}(0) = -\frac{\sigma_0}{\varepsilon_1}d_1 \\ &= \frac{d_1}{\varepsilon_1}\frac{\left(s_1 e^{-\kappa x_{N+1}}\left(-\frac{d_L}{\varepsilon_L}+\frac{1}{\kappa\varepsilon}\right)+s_2 e^{\kappa x_{N+1}}\left(\frac{d_L}{\varepsilon_L}+\frac{1}{\kappa\varepsilon}\right)\right)}{\left(\frac{1}{\kappa\varepsilon}-\frac{x_1}{\varepsilon_1}\right)\left(\frac{1}{\kappa\varepsilon}-\frac{d_L}{\varepsilon_L}\right)e^{-\kappa Nd}-\left(\frac{1}{\kappa\varepsilon}+\frac{x_1}{\varepsilon_1}\right)\left(\frac{1}{\kappa\varepsilon}+\frac{d_L}{\varepsilon_L}\right)e^{\kappa Nd}}. \end{aligned} \tag{C.30}$$

D Capacitor Model for the Description of Polyelectrolyte Multilayers: Volume Charges

In this appendix, we present the detailed derivation of the expression for the surface potential of a field-effect device functionalized with polyelectrolyte multilayers, where the charges are assumed to be homogeneously distributed in layers with a volume charge density $\rho = \pm\frac{\sigma}{d}$. The model is described in the second part of section 4.1.3. We use the same notation as introduced there. For layers of a finite thickness d which have a

homogeneous volume charge density of ρ the Debye-Hückel equation is given by

$$\frac{\mathrm{d}^2}{\mathrm{d}x^2}\psi(x) - \kappa^2\psi(x) = -\frac{1}{\varepsilon}\rho(x). \tag{D.1}$$

We are interested in the solution $\psi(x)$ to this equation. The inhomogeneity $\rho(x)$ is not dependent on $\psi(x)$. The solution is then given by the general solution of the homogeneous differential equation $\psi_\mathrm{h}(x)$

$$\frac{\mathrm{d}^2}{\mathrm{d}x^2}\psi_\mathrm{h}(x) - \kappa^2\psi_\mathrm{h}(x) = 0 \tag{D.2}$$

$$\psi_\mathrm{h}(x) = C\exp(-\kappa x) + D\exp(\kappa x) \tag{D.3}$$

plus a particular solution of the inhomogeneous differential equation. So first we have to find such a particular solution. This can be done using the Green's function $G(x-x')$, which is the solution of

$$\frac{\mathrm{d}^2}{\mathrm{d}x^2}G(x-x') - \kappa^2 G(x-x') = -\frac{1}{\varepsilon}\delta(x-x'). \tag{D.4}$$

A particular solution for the inhomogeneous equation is then given by

$$\psi_\mathrm{p}(x) = \int \mathrm{d}x'\rho(x')\,G(x-x'). \tag{D.5}$$

A Green's function for the given differential equation is

$$G(x-x') = \frac{1}{2\varepsilon\kappa}\exp(-\kappa|x-x'|). \tag{D.6}$$

Assuming a homogeneous charge distribution from x_0 to x_0+d we obtain

$$\psi_\mathrm{p}(x) = \frac{1}{2\varepsilon\kappa}\rho_0\int_{x_0}^{x_0+d}\mathrm{d}x'\exp(-\kappa|x-x'|). \tag{D.7}$$

For $x_0 < x < x_0+d$ this yields

$$\begin{aligned}
\psi_\mathrm{p}(x) &= \frac{1}{2\varepsilon\kappa}\rho_0\int_{x_0}^{x_0+d}\mathrm{d}x'\exp(-\kappa|x-x'|)\\
&= \frac{1}{2\varepsilon\kappa}\rho_0\left(\int_{x_0}^{x}\mathrm{d}x'\exp(-\kappa(x-x')) + \int_{x}^{x_0+d}\mathrm{d}x'\exp(\kappa(x-x'))\right)\\
&= \frac{1}{2\varepsilon\kappa^2}\rho_0\left(2-\exp(-\kappa(x-x_0)) - \exp(\kappa(x-x_0-d))\right).
\end{aligned} \tag{D.8}$$

We add the general solution of the homogeneous equation $\psi_{\mathrm{h}}(x)$

$$\begin{aligned}\psi_{\mathrm{tot}}(x) &= \psi_{\mathrm{p}}(x) + \psi_{\mathrm{h}}(x) \\ &= Ce^{-\kappa x} + De^{\kappa x} + \frac{1}{2\varepsilon\kappa^2}\rho_0\left(2 - e^{-\kappa(x-x_0)} - e^{\kappa(x-x_0-d)}\right). \end{aligned} \tag{D.9}$$

The coefficients C and D of $\psi_{\mathrm{tot}}(x)$ have not yet been determined. We choose C and D so that

$$\psi_{\mathrm{tot}}(x_0) = \psi_{\mathrm{tot}}(x_0 + d) = 0, \tag{D.10}$$

i.e.

$$C\exp(-\kappa x_0) + D\exp(\kappa x_0) = \frac{1}{2\varepsilon\kappa^2}\rho_0\left(\exp(-\kappa d) - 1\right) \tag{D.11}$$

and

$$C\exp\left(-\kappa\left(x_0 + d\right)\right) + D\exp\left(\kappa\left(x_0 + d\right)\right) = \frac{1}{2\varepsilon\kappa^2}\rho_0\left(\exp(-\kappa d) - 1\right). \tag{D.12}$$

We multiply by $\exp\left(-\kappa\left(x_0 + d\right)\right)$ and $\exp(-\kappa x_0)$, respectively

$$\begin{aligned}&C\exp(-\kappa x_0)\exp\left(-\kappa\left(x_0 + d\right)\right) + D\exp(\kappa x_0)\exp\left(-\kappa\left(x_0 + d\right)\right) \\ &= \frac{1}{2\varepsilon\kappa^2}\rho_0\left(\exp(-\kappa d) - 1\right)\exp\left(-\kappa\left(x_0 + d\right)\right), \end{aligned} \tag{D.13}$$

$$\begin{aligned}&C\exp\left(-\kappa\left(x_0 + d\right)\right)\exp(-\kappa x_0) + D\exp\left(\kappa\left(x_0 + d\right)\right)\exp(-\kappa x_0) \\ &= \frac{1}{2\varepsilon\kappa^2}\rho_0\left(\exp(-\kappa d) - 1\right)\exp(-\kappa x_0) \end{aligned} \tag{D.14}$$

and obtain for D

$$D = \frac{1}{2\varepsilon\kappa^2}\rho_0\frac{\left(\exp(-\kappa d) - 1\right)\left(\exp\left(-\kappa\left(x_0 + d\right)\right) - \exp(-\kappa x_0)\right)}{\exp(-\kappa d) - \exp(\kappa d)}. \tag{D.15}$$

We multiply by $\exp\left(\kappa\left(x_0 + d\right)\right)$ and $\exp(\kappa x_0)$, respectively

$$\begin{aligned}&C\exp(-\kappa x_0)\exp\left(\kappa\left(x_0 + d\right)\right) + D\exp(\kappa x_0)\exp\left(\kappa\left(x_0 + d\right)\right) \\ &= \frac{1}{2\varepsilon\kappa^2}\rho_0\left(\exp(-\kappa d) - 1\right)\exp\left(\kappa\left(x_0 + d\right)\right), \end{aligned} \tag{D.16}$$

$$\begin{aligned}&C\exp\left(-\kappa\left(x_0 + d\right)\right)\exp(\kappa x_0) + D\exp\left(\kappa\left(x_0 + d\right)\right)\exp(\kappa x_0) \\ &= \frac{1}{2\varepsilon\kappa^2}\rho_0\left(\exp(-\kappa d) - 1\right)\exp(\kappa x_0) \end{aligned} \tag{D.17}$$

and obtain for C

$$C = \frac{1}{2\varepsilon\kappa^2}\rho_0\frac{\left(\exp(-\kappa d) - 1\right)\left(\exp\left(\kappa\left(x_0 + d\right)\right) - \exp(\kappa x_0)\right)}{\exp(\kappa d) - \exp(-\kappa d)}. \tag{D.18}$$

Thus

$$\psi_{\rm tot}\left(x\right) = \frac{1}{2\varepsilon\kappa^2}\rho_0\Bigg[\left(e^{-\kappa d}-1\right)\frac{\left(e^{\kappa(x_0+d)}-e^{\kappa x_0}\right)e^{-\kappa x}-\left(e^{-\kappa(x_0+d)}-e^{-\kappa x_0}\right)e^{\kappa x}}{e^{\kappa d}-e^{-\kappa d}} + \left(2-e^{-\kappa(x-x_0)}-e^{\kappa(x-x_0-d)}\right)\Bigg]. \tag{D.19}$$

For $\psi'_{\rm tot}$ we find

$$\psi'_{\rm tot}\left(x\right) = \frac{1}{2\varepsilon\kappa}\rho_0\Bigg[\frac{\left(1-e^{-\kappa d}\right)}{e^{\kappa d}-e^{-\kappa d}}\left[\left(e^{\kappa(x_0+d)}-e^{\kappa x_0}\right)e^{-\kappa x}+\left(e^{-\kappa(x_0+d)}-e^{-\kappa x_0}\right)e^{\kappa x}\right] + e^{-\kappa(x-x_0)}-e^{\kappa(x-x_0-d)}\Bigg]. \tag{D.20}$$

Thus

$$\begin{aligned}\psi'_{\rm tot}\left(x_0\right) &= \frac{1}{2\varepsilon\kappa}\rho_0\left[\frac{1-\exp\left(-\kappa d\right)}{\exp\left(\kappa d\right)-\exp\left(-\kappa d\right)}\left[\exp\left(\kappa d\right)+\exp\left(-\kappa d\right)-2\right]+1-\exp\left(-\kappa d\right)\right]\\ &= \frac{1}{\varepsilon\kappa}\rho_0\left[\frac{1-\exp\left(-\kappa d\right)}{1+\exp\left(-\kappa d\right)}\right]\end{aligned} \tag{D.21}$$

as well as

$$\begin{aligned}\psi'_{\rm tot}\left(x_0+d\right) &= \frac{1}{2\varepsilon\kappa}\rho_0\left[\frac{\left(1-e^{-\kappa d}\right)}{e^{\kappa d}-e^{-\kappa d}}\left[2-e^{-\kappa d}-e^{\kappa d}\right]+e^{-\kappa d}-1\right]\\ &= \frac{1}{\varepsilon\kappa}\rho_0\left[\frac{1-e^{\kappa d}}{1+e^{\kappa d}}\right].\end{aligned} \tag{D.22}$$

For $\psi'_{\rm tot}$ at the left side of the charged layer we write $\psi'_{\rm tot,l}$, and for $\psi'_{\rm tot}$ at the right side we write $\psi'_{\rm tot,r}$, i.e.

$$\psi'_{\rm tot,l} = \frac{1}{\varepsilon\kappa}\rho_0\left[\frac{1-\exp\left(-\kappa d\right)}{1+\exp\left(-\kappa d\right)}\right], \tag{D.23}$$

$$\begin{aligned}\psi'_{\rm tot,r} &= \frac{1}{\varepsilon\kappa}\rho_0\left[\frac{1-\exp\left(\kappa d\right)}{1+\exp\left(\kappa d\right)}\right]\\ &= -\frac{1}{\varepsilon\kappa}\rho_0\left[\frac{1-\exp\left(-\kappa d\right)}{1+\exp\left(-\kappa d\right)}\right] = -\psi'_{\rm tot,l}.\end{aligned} \tag{D.24}$$

Now we consider multilayers consisting of N alternately charged layers. We have to find the solutions in the $N+2$ domains (i), $(\text{ii})_1$, ..., $(\text{ii})_N$ and (iii)

$$\begin{aligned}
\psi_{(\text{i})}(x) &= A'x + A, && \text{(D.25)}\\
\psi_{(\text{ii})_n}(x) &= C_n \exp(-\kappa x) + D_n \exp(\kappa x) + \psi_{\text{tot},n}(x), \qquad n = 1, \ldots, N && \text{(D.26)}\\
\psi_{(\text{iii})}(x) &= B'x + B. && \text{(D.27)}
\end{aligned}$$

$\psi_{\text{tot},n}$ is obtained from ψ_{tot} by substituting ρ_0 by $\rho_{0,n} = (-1)^{n+1}\rho_0$. The boundary conditions for the potential are given by

$$\psi_{(\text{i})}(0) = 0, \qquad \psi'_{(\text{i})}(0) = -\frac{\sigma_0}{\varepsilon_1}, \quad \text{(D.28)}$$

$$\psi_{(\text{iii})}(x_L) = U_{\text{tot}}, \qquad \psi'_{(\text{iii})}(x_L) = \frac{\sigma_L}{\varepsilon_L} \quad \text{(D.29)}$$

$$\psi_{(\text{ii})_1}(x_1) - \psi_{(\text{i})}(x_1) = 0, \qquad \varepsilon\psi'_{(\text{ii})_1}(x_1) - \varepsilon_1\psi'_{(\text{i})}(x_1) = -\sigma_1, \quad \text{(D.30)}$$

$$\psi_{(\text{iii})}(x_{N+1}) - \psi_{(\text{ii})_N}(x_{N+1}) = 0, \qquad \varepsilon_L\psi'_{(\text{iii})}(x_{N+1}) - \varepsilon\psi'_{(\text{ii})_N}(x_{N+1}) = 0, \quad \text{(D.31)}$$

$$\psi_{(\text{ii})_n}(x_n) - \psi_{(\text{ii})_{n-1}}(x_n) = 0, \qquad \varepsilon\psi'_{(\text{ii})_n}(x_n) - \varepsilon\psi'_{(\text{ii})_{n-1}}(x_n) = 0, \quad \text{(D.32)}$$

$$n = 2, \ldots, N$$

with

$$\begin{aligned}
x_0 &= 0, && \text{(D.33)}\\
x_n &= d_1 + (n-1)\,d, \qquad n = 1, \ldots, N+1, && \text{(D.34)}\\
x_L &= d_1 + Nd + d_L. && \text{(D.35)}
\end{aligned}$$

From the boundary condition it follows that

$$A = 0, \qquad A' = -\frac{\sigma_0}{\varepsilon_1}, \quad \text{(D.36)}$$

$$B = U_{\text{tot}} - \frac{\sigma_L}{\varepsilon_L}x_L, \qquad B' = \frac{\sigma_L}{\varepsilon_L} \quad \text{(D.37)}$$

i.e

$$
\begin{aligned}
C_1 \exp\left(-\kappa x_1\right) + D_1 \exp\left(\kappa x_1\right) &= -\frac{\sigma_0}{\varepsilon_1} x_1, && \text{(D.38)}\\
-C_1 \exp\left(-\kappa x_1\right) + D_1 \exp\left(\kappa x_1\right) &= -\frac{1}{\varepsilon\kappa}\left(\sigma_1 + \sigma_0 + \varepsilon\psi'_{\mathrm{tot,l},1}\right), && \text{(D.39)}\\
C_N \exp\left(-\kappa x_{N+1}\right) + D_N \exp\left(\kappa x_{N+1}\right) &= U_{\mathrm{tot}} - \frac{\sigma_L}{\varepsilon_L} d_L, && \text{(D.40)}\\
-C_N \exp\left(-\kappa x_{N+1}\right) + D_N \exp\left(\kappa x_{N+1}\right) &= -\frac{1}{\varepsilon\kappa}\left(\varepsilon\psi'_{\mathrm{tot,r},N} - \sigma_L\right). && \text{(D.41)}
\end{aligned}
$$

For $n = 2, \ldots, N$ we find

$$
\begin{aligned}
C_n e^{-\kappa x_n} + D_n e^{\kappa x_n} - C_{n-1} e^{-\kappa x_n} - D_{n-1} e^{\kappa x_n} &= 0, && \text{(D.42)}\\
-C_n e^{-\kappa x_n} + D_n e^{\kappa x_n} + C_{n-1} e^{-\kappa x_n} - D_{n-1} e^{\kappa x_n} &= -\frac{1}{\kappa}\left(\psi'_{\mathrm{tot,l},n} - \psi'_{\mathrm{tot,r},n-1}\right). && \text{(D.43)}
\end{aligned}
$$

To obtain equations which are formally equivalent to the equations obtained in case of charged plates (Eq. (C.3) - Eq. (C.6)) we write:

$$
-\frac{1}{\kappa}\left(\psi'_{\mathrm{tot,l},n} - \psi'_{\mathrm{tot,r},n-1}\right) = \frac{(-1)^{n-1}}{\varepsilon\kappa}\sigma \qquad \text{(D.44)}
$$

i.e.

$$
\sigma = (-1)^n \varepsilon\left(\psi'_{\mathrm{tot,l},n} - \psi'_{\mathrm{tot,r},n-1}\right). \qquad \text{(D.45)}
$$

With

$$
\rho_{0,n} = (-1)^{n+1}\rho_0 \qquad \text{(D.46)}
$$

and

$$
\begin{aligned}
\psi'_{\mathrm{tot,l},n} &= \frac{1}{\varepsilon\kappa}\rho_{0,n}\left[\frac{1-\exp\left(-\kappa d\right)}{1+\exp\left(-\kappa d\right)}\right] = (-1)^{n+1}\frac{1}{\varepsilon\kappa}\rho_0\left[\frac{1-\exp\left(-\kappa d\right)}{1+\exp\left(-\kappa d\right)}\right], && \text{(D.47)}\\
\psi'_{\mathrm{tot,r},n} &= \frac{1}{\varepsilon\kappa}\rho_{0,n}\left[\frac{1-\exp\left(\kappa d\right)}{1+\exp\left(\kappa d\right)}\right] = (-1)^{n+1}\frac{1}{\varepsilon\kappa}\rho_0\left[\frac{1-\exp\left(\kappa d\right)}{1+\exp\left(\kappa d\right)}\right], && \text{(D.48)}
\end{aligned}
$$

it follows that

$$
\begin{aligned}
\psi'_{\mathrm{tot,l},n} - \psi'_{\mathrm{tot,r},n-1} &= (-1)^{n+1}\frac{1}{\varepsilon\kappa}\rho_0\left[\frac{1-e^{-\kappa d}}{1+e^{-\kappa d}}\right] - (-1)^{n}\frac{1}{\varepsilon\kappa}\rho_0\left[\frac{1-e^{\kappa d}}{1+e^{\kappa d}}\right]\\
&= (-1)^{n+1}\frac{1}{\varepsilon\kappa}\rho_0\left(\left[\frac{1-e^{-\kappa d}}{1+e^{-\kappa d}}\right] + \left[\frac{1-e^{\kappa d}}{1+e^{\kappa d}}\right]\right) = 0. && \text{(D.49)}
\end{aligned}
$$

With this we can write

$$\begin{aligned}\sigma &= (-1)^n \varepsilon (-1)^{n+1} \frac{1}{\varepsilon\kappa}\rho_0 \left(\left[\frac{1-\exp(-\kappa d)}{1+\exp(-\kappa d)} \right] + \left[\frac{1-\exp(\kappa d)}{1+\exp(\kappa d)} \right] \right) \\ &= -\frac{1}{\kappa}\rho_0 \left(\left[\frac{1-\exp(-\kappa d)}{1+\exp(-\kappa d)} \right] + \left[\frac{1-\exp(\kappa d)}{1+\exp(\kappa d)} \right] \right) = 0. \end{aligned} \tag{D.50}$$

For clarity we substitute names according to

$$\sigma_1 \rightarrow \tilde{\sigma}_1, \tag{D.51}$$

$$\sigma_L \rightarrow \tilde{\sigma}_L, \tag{D.52}$$

$$U_{\text{tot}} \rightarrow \tilde{U}_{\text{tot}}. \tag{D.53}$$

Eq. (D.38) - Eq. (D.41) are now given by

$$C_1 \exp(-\kappa x_1) + D_1 \exp(\kappa x_1) = -\frac{\sigma_0}{\varepsilon_1} x_1, \tag{D.54}$$

$$-C_1 \exp(-\kappa x_1) + D_1 \exp(\kappa x_1) = -\frac{1}{\varepsilon\kappa}\left(\tilde{\sigma}_1 + \sigma_0 + \varepsilon\psi'_{\text{tot,l,1}}\right), \tag{D.55}$$

$$C_N \exp(-\kappa x_{N+1}) + D_N \exp(\kappa x_{N+1}) = \tilde{U}_{\text{tot}} - \frac{\tilde{\sigma}_L}{\varepsilon_L} d_L, \tag{D.56}$$

$$-C_N \exp(-\kappa x_{N+1}) + D_N \exp(\kappa x_{N+1}) = -\frac{1}{\varepsilon\kappa}\left(\varepsilon\psi'_{\text{tot,r},N} - \tilde{\sigma}_L\right). \tag{D.57}$$

We define

$$\sigma_1 = \tilde{\sigma}_1 + \varepsilon\psi'_{\text{tot,l,1}} \tag{D.58}$$

$$\sigma_L = -\varepsilon\psi'_{\text{tot,r},N} + \tilde{\sigma}_L + (-1)^N \sigma \tag{D.59}$$

$$\tilde{\sigma}_L - \sigma_L = \varepsilon\psi'_{\text{tot,r},N} - (-1)^N \sigma \tag{D.60}$$

$$\begin{aligned} U_{\text{tot}} &= \tilde{U}_{\text{tot}} - \frac{d_L}{\varepsilon_L}\left(\tilde{\sigma}_L - \sigma_L\right) \\ &= \tilde{U}_{\text{tot}} + \frac{d_L}{\varepsilon_L}\left(-\varepsilon\psi'_{\text{tot,r},N} + (-1)^N \sigma\right). \end{aligned} \tag{D.61}$$

Now we can write Eq. (D.54) - Eq. (D.57)

$$\begin{aligned} C_1 \exp(-\kappa x_1) + D_1 \exp(\kappa x_1) &= -\frac{\sigma_0}{\varepsilon_1} x_1, && \text{(D.62)} \\ -C_1 \exp(-\kappa x_1) + D_1 \exp(\kappa x_1) &= -\frac{1}{\varepsilon\kappa}(\sigma_1 + \sigma_0), && \text{(D.63)} \\ C_N \exp(-\kappa x_{N+1}) + D_N \exp(\kappa x_{N+1}) &= U_{\text{tot}} - \frac{\sigma_L}{\varepsilon_L} d_L, && \text{(D.64)} \\ -C_N \exp(-\kappa x_{N+1}) + D_N \exp(\kappa x_{N+1}) &= -\frac{1}{\varepsilon\kappa}\left((-1)^N \sigma - \sigma_L\right). && \text{(D.65)} \end{aligned}$$

The equations are now formally identical to the equations for the charged plates (Eq. (C.3) - Eq. (C.6)). Therefore we can apply the same solution:

$$\sigma_0 = \frac{\left(s_1 e^{-\kappa x_{N+1}}\left(-\frac{d_L}{\varepsilon_L} + \frac{1}{\kappa\varepsilon}\right) + s_2 e^{\kappa x_{N+1}}\left(\frac{d_L}{\varepsilon_L} + \frac{1}{\kappa\varepsilon}\right)\right)}{-\left(\frac{1}{\kappa\varepsilon} - \frac{x_1}{\varepsilon_1}\right)\left(\frac{1}{\kappa\varepsilon} - \frac{d_L}{\varepsilon_L}\right) e^{-\kappa N d} + \left(\frac{1}{\kappa\varepsilon} + \frac{x_1}{\varepsilon_1}\right)\left(\frac{1}{\kappa\varepsilon} + \frac{d_L}{\varepsilon_L}\right) e^{\kappa N d}} \tag{D.66}$$

with

$$\begin{aligned} \begin{pmatrix} s_1 \\ s_2 \end{pmatrix} &= \begin{pmatrix} \frac{1}{\kappa\varepsilon}\sigma_1 e^{\kappa x_1} - \frac{(-1)^N}{\kappa\varepsilon}\sigma e^{\kappa x_{N+1}} - e^{\kappa x_{N+1}} U_{\text{tot}} \\ -\frac{1}{\kappa\varepsilon}\sigma_1 e^{-\kappa x_1} + \frac{(-1)^N}{\kappa\varepsilon}\sigma e^{-\kappa x_{N+1}} - e^{-\kappa x_{N+1}} U_{\text{tot}} \end{pmatrix} \\ &\quad + \frac{1}{\kappa}\frac{\sigma}{\varepsilon}\begin{pmatrix} e^{\kappa d_1}\frac{e^{\kappa d} + (-1)^N e^{\kappa d N}}{1 + e^{\kappa d}} \\ -e^{-\kappa d_1}\frac{e^{-\kappa d} + (-1)^N e^{-\kappa d N}}{1 + e^{-\kappa d}} \end{pmatrix}. \end{aligned} \tag{D.67}$$

With

$$U_1 = -\frac{d_1}{\varepsilon_1}\sigma_0 \tag{D.68}$$

and $\sigma = 0$ we obtain

$$\begin{pmatrix} s_1 \\ s_2 \end{pmatrix} = \begin{pmatrix} \frac{1}{\kappa\varepsilon}\sigma_1 e^{\kappa x_1} - e^{\kappa x_{N+1}} U_{\text{tot}} \\ -\frac{1}{\kappa\varepsilon}\sigma_1 e^{-\kappa x_1} - e^{-\kappa x_{N+1}} U_{\text{tot}} \end{pmatrix} \tag{D.69}$$

and

$$U_1 = \frac{1}{\kappa\varepsilon}\frac{d_1}{\varepsilon_1}\frac{\sigma_1\left(e^{-\kappa N d}\left(\frac{1}{\kappa\varepsilon} - \frac{d_L}{\varepsilon_L}\right) - e^{\kappa N d}\left(\frac{1}{\kappa\varepsilon} + \frac{d_L}{\varepsilon_L}\right)\right) - 2U_{\text{tot}}}{\left(\frac{1}{\kappa\varepsilon} - \frac{d_1}{\varepsilon_1}\right)\left(\frac{1}{\kappa\varepsilon} - \frac{d_L}{\varepsilon_L}\right) e^{-\kappa N d} - \left(\frac{1}{\kappa\varepsilon} + \frac{d_1}{\varepsilon_1}\right)\left(\frac{1}{\kappa\varepsilon} + \frac{d_L}{\varepsilon_L}\right) e^{\kappa N d}}. \tag{D.70}$$

Using Eq. (D.58) and Eq. (D.61) we find

$$U_1 = \frac{1}{\kappa\varepsilon}\frac{d_1}{\varepsilon_1}\frac{\left(\tilde{\sigma}_1 + \varepsilon\psi'_{\text{tot,l,1}}\right)\left(e^{-\kappa N d}\left(\frac{1}{\kappa\varepsilon} - \frac{d_L}{\varepsilon_L}\right) - e^{\kappa N d}\left(\frac{1}{\kappa\varepsilon} + \frac{d_L}{\varepsilon_L}\right)\right) - 2\left(\tilde{U}_{\text{tot}} - \varepsilon\frac{d_L}{\varepsilon_L}\psi'_{\text{tot,r},N}\right)}{\left(\frac{1}{\kappa\varepsilon} - \frac{d_1}{\varepsilon_1}\right)\left(\frac{1}{\kappa\varepsilon} - \frac{d_L}{\varepsilon_L}\right) e^{-\kappa N d} - \left(\frac{1}{\kappa\varepsilon} + \frac{d_1}{\varepsilon_1}\right)\left(\frac{1}{\kappa\varepsilon} + \frac{d_L}{\varepsilon_L}\right) e^{\kappa N d}} \tag{D.71}$$

with

$$\psi'_{\mathrm{tot,l,1}} = \frac{1}{\varepsilon\kappa}\frac{\tilde{\sigma}}{d}\left[\frac{1-\exp\left(-\kappa d\right)}{1+\exp\left(-\kappa d\right)}\right], \tag{D.72}$$

$$\psi'_{\mathrm{tot,r},N} = (-1)^{N+1}\frac{1}{\varepsilon\kappa}\frac{\tilde{\sigma}}{d}\left[\frac{1-\exp\left(\kappa d\right)}{1+\exp\left(\kappa d\right)}\right] = (-1)^{N}\frac{1}{\varepsilon\kappa}\frac{\tilde{\sigma}}{d}\left[\frac{1-\exp\left(-\kappa d\right)}{1+\exp\left(-\kappa d\right)}\right]. \tag{D.73}$$

We define an effective charge density $\tilde{\sigma}_{\mathrm{eff}}$ as follows

$$\tilde{\sigma}_{\mathrm{eff}} = \frac{1}{\kappa d}\left[\frac{1-\exp\left(-\kappa d\right)}{1+\exp\left(-\kappa d\right)}\right]\tilde{\sigma}. \tag{D.74}$$

This yields

$$U_1\left(N\right) = \frac{1}{\kappa\varepsilon}\frac{d_1}{\varepsilon_1}\frac{\left(\tilde{\sigma}_1+\tilde{\sigma}_{\mathrm{eff}}\right)\left(e^{-\kappa N d}\left(\frac{1}{\kappa\varepsilon}-\frac{d_L}{\varepsilon_L}\right)-e^{\kappa N d}\left(\frac{1}{\kappa\varepsilon}+\frac{d_L}{\varepsilon_L}\right)\right)-2\left(\tilde{U}_{\mathrm{tot}}-\frac{d_L}{\varepsilon_L}\left(-1\right)^N\tilde{\sigma}_{\mathrm{eff}}\right)}{\left(\frac{1}{\kappa\varepsilon}-\frac{d_1}{\varepsilon_1}\right)\left(\frac{1}{\kappa\varepsilon}-\frac{d_L}{\varepsilon_L}\right)e^{-\kappa N d}-\left(\frac{1}{\kappa\varepsilon}+\frac{d_1}{\varepsilon_1}\right)\left(\frac{1}{\kappa\varepsilon}+\frac{d_L}{\varepsilon_L}\right)e^{\kappa N d}}. \tag{D.75}$$

Rewriting Eq. (D.75) in terms of capacitances and using hyperbolic functions leads to the final expression

$$U_1\left(N\right) = \frac{\left(\left(\tilde{\sigma}_1+\tilde{\sigma}_{\mathrm{eff}}\right)\right)\left[\frac{1}{C_{\mathrm{P}}}\sinh\left(\kappa N d\right)+\frac{1}{C_{\mathrm{D}}}\cosh\left(\kappa N d\right)\right]+\left(\tilde{U}_{\mathrm{tot}}-\frac{1}{C_{\mathrm{D}}}(-1)^N\tilde{\sigma}_{\mathrm{eff}}\right)}{\left(C_{\mathrm{S}}/C_{\mathrm{P}}+C_{\mathrm{P}}/C_{\mathrm{D}}\right)\sinh\left(\kappa N d\right)+\left(1+C_{\mathrm{S}}/C_{\mathrm{D}}\right)\cosh\left(\kappa N d\right)}. \tag{D.76}$$

References

[1] F. Pouthas, C. Gentil, D. Cote, G. Zeck, B. Straub, and U. Bockelmann. Spatially resolved electronic detection of biopolymers. *Physical Review E*, 70(3):031906, 2004.

[2] J. Fritz, E. B. Cooper, S. Gaudet, P. K. Sorger, and S. R. Manalis. Electronic detection of dna by its intrinsic molecular charge. *Proc Natl Acad Sci U S A*, 99(22):14142–14146, 2002.

[3] F. Uslu, S. Ingebrandt, D. Mayer, S. Bocker-Meffert, M. Odenthal, and A. Offenhausser. Labelfree fully electronic nucleic acid detection system based on a field-effect transistor device. *Biosensors & Bioelectronics*, 19(12):1723–1731, 2004.

[4] Y. Cui, Q. Q. Wei, H. K. Park, and C. M. Lieber. Nanowire nanosensors for highly sensitive and selective detection of biological and chemical species. *Science*, 293(5533):1289–1292, 2001.

[5] W. S. Yang and R. J. Hamers. Fabrication and characterization of a biologically sensitive field-effect transistor using a nanocrystalline diamond thin film. *Applied Physics Letters*, 85(16):3626–3628, 2004.

[6] S. Q. Lud, M. G. Nikolaides, I. Haase, M. Fischer, and A. R. Bausch. Field effect of screened charges: electrical detection of peptides and proteins by a thin-film resistor. *Chemphyschem*, 7(2):379–384, 2006.

[7] G. Steinhoff, O. Purrucker, M. Tanaka, M. Stutzmann, and M. Eickhoff. $Al_xGa_{1-x}N$ - a new material system for biosensors. *Advanced Functional Materials*, 13(11):841–846, 2003.

[8] G. Steinhoff, B. Baur, G. Wrobel, S. Ingebrandt, A. Offenhausser, A. Dadgar, A. Krost, M. Stutzmann, and M. Eickhoff. Recording of cell action potentials with AlGaN/GaN field-effect transistors. *Applied Physics Letters*, 86(3):033901, 2005.

[9] S. M. Luber, K. Adlkofer, U. Rant, A. Ulman, A. Golzhauser, M. Grunze, D. Schuh, A. Tanaka, M. Tornow, and G. Abstreiter. Liquid phase sensors based on chemically functionalized GaAs/AlGaAs heterostructures. *Physica E-Low-Dimensional Systems & Nanostructures*, 21(2-4):1111–1115, 2004.

[10] A. Härtl, E. Schmich, J. A. Garrido, J. Hernando, S. C. R. Catharino, S. Walter, P. Feulner, A. Kromka, D. Steinmuller, and M. Stutzmann. Protein-modified

nanocrystalline diamond thin films for biosensor applications. *Nature Materials*, 3(10):736–742, 2004.

[11] M. G. Nikolaides, S. Rauschenbach, S. Luber, K. Buchholz, M. Tornow, G. Abstreiter, and A. R. Bausch. Silicon-on-insulator based thin-film resistor for chemical and biological sensor applications. *Chemphyschem*, 4(10):1104–1106, 2003.

[12] G. Decher, J. D. Hong, and J. Schmitt. Buildup of ultrathin multilayer films by a self-assembly process. iii : Consecutively alternating adsorption of anionic and cationic polyelectrolytes on charged surfaces. *Thin Solid Films*, 210:831–835, 1992.

[13] G. Decher. Fuzzy nanoassemblies: Toward layered polymeric multicomposites. *Science*, 277(5330):1232–1237, 1997.

[14] P. Bertrand, A. Jonas, A. Laschewsky, and R. Legras. Ultrathin polymer coatings by complexation of polyelectrolytes at interfaces: suitable materials, structure and properties. *Macromolecular Rapid Communications*, 21(7):319–348, 2000.

[15] R. von Klitzing. Internal structure of polyelectrolyte multilayer assemblies. *Physical Chemistry Chemical Physics*, 8(43):5012–5033, 2006.

[16] T. Farhat, G. Yassin, S. T. Dubas, and J. B. Schlenoff. Water and ion pairing in polyelectrolyte multilayers. *Langmuir*, 15(20):6621–6623, 1999.

[17] J. B. Schlenoff, H. Ly, and M. Li. Charge and mass balance in polyelectrolyte multilayers. *Journal Of The American Chemical Society*, 120(30):7626–7634, 1998.

[18] J. Schmitt, T. Grunewald, G. Decher, P. S. Pershan, K. Kjaer, and M. Lösche. Internal structure of layer-by-layer adsorbed polyelectrolyte films - a neutron and X-Ray reflectivity study. *Macromolecules*, 26(25):7058–7063, 1993.

[19] M. Lösche, J. Schmitt, G. Decher, W. G. Bouwman, and K. Kjaer. Detailed structure of molecularly thin polyelectrolyte multilayer films on solid substrates as revealed by neutron reflectometry. *Macromolecules*, 31(25):8893–8906, 1998.

[20] G. B. Sukhorukov, E. Donath, H. Lichtenfeld, E. Knippel, M. Knippel, A. Budde, and H. Mohwald. Layer-by-layer self assembly of polyelectrolytes on colloidal particles. *Colloids And Surfaces A-Physicochemical And Engineering Aspects*, 137(1-3):253–266, 1998.

[21] R. v. Klitzing and H. Möhwald. Proton concentration profile in ultrathin polyelectrolyte films. *Langmuir*, 11:3554–3559, 1995.

[22] C. J. Slevin, A. Malkia, P. Liljeroth, M. Toiminen, and K. Kontturi. Electrochemical characterization of polyelectrolyte multilayers deposited at liquid-liquid interfaces. *Langmuir*, 19(4):1287–1294, 2003.

[23] N. G. Hoogeveen, M. A. C. Stuart, and G. J. Fleer. Polyelectrolyte adsorption on oxides .1. Kinetics and adsorbed amounts. *Journal Of Colloid And Interface Science*, 182(1):133–145, 1996.

[24] R. Steitz, W. Jaeger, and R. v. Klitzing. Influence of charge density and ionic strength on the multilayer formation of strong polyelectrolytes. *Langmuir*, 17(15):4471–4474, 2001.

[25] K. Glinel, A. Moussa, A. M. Jonas, and A. Laschewsky. Influence of polyelectrolyte charge density on the formation of multilayers of strong polyelectrolytes at low ionic strength. *Langmuir*, 18(4):1408–1412, 2002.

[26] B. Schoeler, G. Kumaraswamy, and F. Caruso. Investigation of the influence of polyelectrolyte charge density on the growth of multilayer thin films prepared by the layer-by-layer technique. *Macromolecules*, 35(3):889–897, 2002.

[27] U. Voigt, V. Khrenov, K. Thuer, M. Hahn, W. Jaeger, and R. von Klitzing. The effect of polymer charge density and charge distribution on the formation of multilayers. *Journal Of Physics-Condensed Matter*, 15(1):S213–S218, 2003.

[28] U. Voigt, W. Jaeger, G. H. Findenegg, and R. V. Klitzing. Charge effects on the formation of multilayers containing strong polyelectrolytes. *Journal Of Physical Chemistry B*, 107(22):5273–5280, 2003.

[29] K. Lowack and C. A. Helm. Molecular mechanisms controlling the self-assembly process of polyelectrolyte multilayers. *Macromolecules*, 31(3):823–833, 1998.

[30] P. Fischer and A. Laschewsky. Layer-by-layer adsorption of identically charged polyelectrolytes. *Macromolecules*, 33(3):1100–1102, 2000.

[31] W. B. Stockton and M. F. Rubner. Molecular-level processing of conjugated polymers .4. Layer-by-layer manipulation of polyaniline via hydrogen-bonding interactions. *Macromolecules*, 30(9):2717–2725, 1997.

[32] Q. Wang. Charge inversion by flexible polyelectrolytes on flat surfaces from self-consistent field calculations. *Macromolecules*, 38(21):8911–8922, 2005.

[33] A. Shafir and D. Andelman. Polyelectrolyte multilayer formation: Electrostatics and short-range interactions. *European Physical Journal E*, 19(2):155–162, 2006.

[34] L. C. Clark and C. Lyons. Electrode systems for continuous monitoring in cardiovascular surgery. *Ann N Y Acad Sci*, 102:29–45, 1962.

[35] P. Bergveld. Thirty years of isfetology - what happened in the past 30 years and what may happen in the next 30 years. *Sensors And Actuators B-Chemical*, 88(1):1–20, 2003.

[36] M. J. Schöning and A. Poghossian. Recent advances in biologically sensitive field-effect transistors (BioFETs). *Analyst*, 127(9):1137–1151, 2002.

[37] D. R. Thévenot, K. Toth, R. A. Durst, and G. S. Wilson. Electrochemical biosensors: recommended definitions and classification. *Biosens Bioelectron*, 16(1-2):121–131, 2001.

[38] M. M. F. Choi. Progress in enzyme-based biosensors using optical transducers. *Microchimica Acta*, 148(3-4):107–132, 2004.

[39] S. Andreescu and J. L. Marty. Twenty years research in cholinesterase biosensors: From basic research to practical applications. *Biomolecular Engineering*, 23(1):1–15, 2006.

[40] P. V. Bernhardt. Enzyme electrochemistry - biocatalysis on an electrode. *Australian Journal Of Chemistry*, 59(4):233–256, 2006.

[41] B. Baur, J. Howgate, H. G. von Ribbeck, Y. Gawlina, V. Bandalo, G. Steinhoff, M. Stutzmann, and M. Eickhoff. Catalytic activity of enzymes immobilized on AlGaN/GaN solution gate field-effect transistors. *Applied Physics Letters*, 89(18):183901, 2006.

[42] S. V. Dzyadevych, A. P. Soldatkin, Y. I. Korpan, V. N. Arkhypova, A. V. El'skaya, J.-M. Chovelon, C. Martelet, and N. Jaffrezic-Renault. Biosensors based on enzyme field-effect transistors for determination of some substrates and inhibitors. *Anal Bioanal Chem*, 377(3):496–506, 2003.

[43] S. Caras and J. Janata. Field-effect transistor sensitive to penicillin. *Analytical Chemistry*, 52(12):1935–1937, 1980.

[44] M. J. Schöning and A. Poghossian. Bio FEDs (field-effect devices): State-of-the-art and new directions. *Electroanalysis*, 18(19-20):1893–1900, 2006.

[45] F. Lottspeich and H. Zorbas, editors. *Bioanalytik*. Spektrum Akademischer Verlag, 1998.

[46] H. J. Lee, A. W. Wark, T. T. Goodrich, S. P. Fang, and R. M. Corn. Surface enzyme kinetics for biopolymer microarrays: a combination of Langmuir and Michaelis-Menten concepts. *Langmuir*, 21(9):4050–4057, 2005.

[47] P. Bergveld. Development of an ion-sensitive solid-state device for neurophysiological measurements. *IEEE Trans Biomed Eng*, 17(1):70–71, 1970.

[48] S. M. Sze. *Semiconductor devices. Physics and Technology*, chapter 6. John Wiley, 2002.

[49] D. C. Grahame. The electrical double layer and the theory of electrocapillarity. *Chem. Rev.*, 41:441–501, 1947.

[50] A. J. Bard and L. R. Faulkner. *Electrochemical Methods*. John Wiley & Sons, 2001.

[51] D. Landheer, G. Aers, W. R. McKinnon, M. J. Deen, and J. C. Ranuarez. Model for the field effect from layers of biological macromolecules on the gates of metal-oxide-semiconductor transistors. *J. Appl. Phys.*, 98:044701, 2005.

[52] B. K. Wunderlich. Silicon-On-Insulator basierter Biosensor: Möglichkeiten der quantitativen Detektion. Diplomarbeit, Technische Universität München, 2006.

[53] T. Yonehara and K. Sakaguchi. ELTRAN: Novel SOI wafer technology. *YSAP International*, 4:10–16, 2001.

[54] M. G. Nikolaides. *Silicon-on-insulator based thin-film-resistor for the detection of biomolecular interactions*. Dissertation, Fakultät für Physik der Technische Universität München, 2004.

[55] W. M. Siu and R. S. C. Cobbold. Basic properties of the electrolyte-SiO_2-Si system - physical and theoretical aspects. *IEEE Transactions On Electron Devices*, 26(11):1805–1815, 1979.

[56] P. A. Neff, A. Naji, C. Ecker, B. Nickel, R. v. Klitzing, and A. R. Bausch. Electrical detection of self-assembled polyelectrolyte multilayers by a thin film resistor. *Macromolecules*, 39(2):463–466, 2006.

[57] P. A. Neff, B. K. Wunderlich, S. Q. Lud, and A. R. Bausch. Silicon-on-insulator based thin film resistors for quantitative biosensing applications. *phys. stat. sol. (a)*, 203(14):3417–3423, 2006.

[58] M. Schönhoff. Self-assembled polyelectrolyte multilayers. *Current Opinion In Colloid & Interface Science*, 8(1):86–95, 2003.

[59] M. Schönhoff. Layered polyelectrolyte complexes: physics of formation and molecular properties. *Journal Of Physics-Condensed Matter*, 15(49):R1781–R1808, 2003.

[60] H. H. Rmaile and J. B. Schlenoff. "Internal pK_a's" in polyelectrolyte multilayers: Coupling protons and salt. *Langmuir*, 18(22):8263–8265, 2002.

[61] L. J. Bousse, S. Mostarshed, and D. Hafeman. Combined measurement of surface-potential and zeta potential at insulator electrolyte interfaces. *Sensors And Actuators B-Chemical*, 10(1):67–71, 1992.

[62] C. Reich, P. A. Neff, A. R. Bausch, J. O. Rädler, and Bert Nickel. Supported membranes on polyelectrolyte layers studied by X-ray reflectometry. *phys. stat. sol. (a)*, 203(14):3463–3467, 2006.

[63] B. K. Wunderlich, P. A. Neff, and A. R. Bausch. Modelling field effect devices for biosensing applications. *in preparation.*

[64] J. N. Israelachvili. *Intermolecular and Surface forces.* Academic Press, London, 1991.

[65] R. R. Netz. Debye-Hückel theory for slab geometries. *European Physical Journal E*, 3(2):131–141, 2000.

[66] K. Hänni-Ciunel, G. Findenegg, and R. v. Klitzing. *in preparation.*

[67] C. Tedeschi, H. Möhwald, and S. Kirstein. Polarity of layer-by-layer deposited polyelectrolyte films as determined by pyrene fluorescence. *Journal Of The American Chemical Society*, 123(5):954–960, 2001.

[68] R. Steitz, V. Leiner, R. Siebrecht, and R. v. Klitzing. Influence of the ionic strength on the structure of polyelectrolyte films at the solid/liquid interface. *Colloids And Surfaces A-Physicochemical And Engineering Aspects*, 163(1):63–70, 2000.

[69] J. E. Wong, F. Rehfeldt, P. Hanni, M. Tanaka, and R. v. Klitzing. Swelling behavior of polyelectrolyte multilayers in saturated water vapor. *Macromolecules*, 37(19):7285–7289, 2004.

[70] D. Carriere, R. Krastev, and M. Schönhoff. Oscillations in solvent fraction of polyelectrolyte multilayers driven by the charge of the terminating layer. *Langmuir*, 20(26):11465–11472, 2004.

[71] B. Schwarz and M. Schönhoff. Surface potential driven swelling of polyelectrolyte multilayers. *Langmuir*, 18(8):2964–2966, 2002.

[72] O. F. Mohammed, D. Pines, J. Dreyer, E. Pines, and E. T. J. Nibbering. Sequential proton transfer through water bridges in acid-base reactions. *Science*, 310(5745):83–86, 2005.

[73] R. Pomès and B. Roux. Molecular mechanism of H^+ conduction in the single-file water chain of the gramicidin channel. *Biophys J*, 82(5):2304–2316, 2002.

[74] Y. Wu, B. Ilan, and G. A. Voth. Charge delocalization in proton channels, ii: The synthetic LS2 channel and proton selectivity. *Biophys J*, 92(1):61–69, 2007.

[75] P. A. Neff, B. K.Wunderlich, R. v. Klitzing, and A. R. Bausch. Formation and dielectric properties of polyelectrolyte multilayers studied by a silicon-on-insulator based thin film resistor. *Langmuir*, accepted.

[76] J. F. Joanny. Polyelectrolyte adsorption and charge inversion. *European Physical Journal B*, 9(1):117–122, 1999.

[77] N. Laugel, C. Betscha, M. Winterhalter, J. C. Voegel, P. Schaaf, and V. Ball. Relationship between the growth regime of polyelectrolyte multilayers and the polyanion/polycation complexation enthalpy. *Journal Of Physical Chemistry B*, 110(39):19443–19449, 2006.

[78] N. G. Hoogeveen, M. A. C. Stuart, G. J. Fleer, and M. R. Bohmer. Formation and stability of multilayers of polyelectrolytes. *Langmuir*, 12(15):3675–3681, 1996.

[79] C. S. J. Hou, N. Milovic, M. Godin, P. R. Russo, R. Chakrabarti, and S. R. Manalis. Label-free microelectronic PCR quantification. *Analytical Chemistry*, 78(8):2526–2531, 2006.

[80] P. Chodanowski and S. Stoll. Polyelectrolyte adsorption on charged particles in the Debye-Hückel approximation. a Monte Carlo approach. *Macromolecules*, 34(7):2320–2328, 2001.

[81] G. J. Fleer, M. A. Stuart Cohen, J. M. H. M. Scheutjens, T. Cosgrove, and B. Vincent. *Polymers at Interfaces*. Chapman and Hall, London, 1993.

[82] R. M. Stroud, L. M. Kay, and R. E. Dickerson. Structure of bovine trypsin - electron-density maps of inhibited enzyme at 5 A and at 27 A resolution. *Journal Of Molecular Biology*, 83(2):185–&, 1974.

[83] E. Katchalski. Poly-alpha-amino acids. *Advances In Protein Chemistry*, 6:123–185, 1951.

[84] S. G. Waley and J. Watson. The action of trypsin on polylysine. *Biochem J*, 55(2):328–337, 1953.

[85] M. Bier and F. F. Nord. On the mechanism of enzyme acition. XLVI. the effect of certain ions on crystalline trypsin and reinvestigation of its isoelectric point. *Arch Biochem*, 33(2):320–332, 1951.

[86] W. G. Miller. Degradation of synthetic polypeptides . 3. Degradation of poly-alpha,l-lysine by proteolytic enzymes in 0.20 M sodium chloride. *Journal Of The American Chemical Society*, 86(19):3918–&, 1964.

[87] R. Kitz and I. B. Wilson. Esters of methanesulfonic acid as irreversible inhibitors of acetylcholinesterase. *J Biol Chem*, 237:3245–3249, 1962.

[88] A. M. Gold and D. E. Fahrney. The mechanism of reactivation of phenylmethane-sulfonyl alpha-chymotrypsin. *Biochem Biophys Res Commun*, 10:55–59, 1963.

[89] D. Voet and J. G. Voet. *Biochemistry*. John Wiley & Sons, 1995.

[90] J. C. van Kerkhof, P. Bergveld, and R. B. M. Schasfoort. The ISFET based heparin sensor with a monolayer of protamine as affinity ligand. *Biosensors & Bioelectronics*, 10(3-4):269–282, 1995.

[91] N. M. Milovic, J. R. Behr, M. Godin, C. S. J. Hou, K. R. Payer, A. Chandrasekaran, P. R. Russo, R. Sasisekharan, and S. R. Manalis. Monitoring of heparin and its low-molecular-weight analogs by silicon field effect. *Proc Natl Acad Sci U S A*, 103(36):13374–13379, 2006.

[92] U. R. Desai, H. M. Wang, and R. J. Linhardt. Substrate-specificity of the heparin lyases from flavobacterium-heparinum. *Archives Of Biochemistry And Biophysics*, 306(2):461–468, 1993.

[93] Sigma-Aldrich. *Product Information H 2519 Heparinase I*, 2005.

[94] A. A. Bhattacharya, T. Grüne, and S. Curry. Crystallographic analysis reveals common modes of binding of medium and long-chain fatty acids to human serum albumin. *J Mol Biol*, 303(5):721–732, 2000.

[95] F. Vollmer, D. Braun, A. Libchaber, M. Khoshsima, I. Teraoka, and S. Arnold. Protein detection by optical shift of a resonant microcavity. *Applied Physics Letters*, 80(21):4057–4059, 2002.

[96] R. J. Chen, S. Bangsaruntip, K. A. Drouvalakis, N. W. S. Kam, M. Shim, Y. M. Li, W. Kim, P. J. Utz, and H. J. Dai. Noncovalent functionalization of carbon nanotubes for highly specific electronic biosensors. *Proceedings Of The National Academy Of Sciences Of The United States Of America*, 100(9):4984–4989, 2003.

[97] A. B. Artyukhin, M. Stadermann, R. W. Friddle, P. Stroeve, O. Bakajin, and A. Noy. Controlled electrostatic gating of carbon nanotube FET devices. *Nano Letters*, 6(9):2080–2085, 2006.

[98] B. Schuler, E. A. Lipman, P. J. Steinbach, M. Kumke, and W. A. Eaton. Polyproline and the "spectroscopic ruler" revisited with single-molecule fluorescence. *Proc Natl Acad Sci U S A*, 102(8):2754–2759, 2005.

[99] R. J. Galneder. *Enzymkinetik von Phospholipase C und Aggregationsverhalten von Gentransfer-Komplexen*. Dissertation, Technische Universität München, 2001.

[100] A. J. Killard, M. R. Smyth, K. Grennan, L. Micheli, and G. Palleschi. Rapid antibody biosensor assays for environmental analysis. *Biochem Soc Trans*, 28(2):81–84, 2000.

[101] L. C. Bock, L. C. Griffin, J. A. Latham, E. H. Vermaas, and J. J. Toole. Selection of single-stranded DNA molecules that bind and inhibit human thrombin. *Nature*, 355(6360):564–566, 1992.

List of Publications

P. A. Neff, A. Naji, C. Ecker, R. v. Klitzing and A. R. Bausch. Electrical detection of self-assembled polyelectrolyte multilayers by a thin film resistor. *Macromolecules*, 39(2):463-466, 2006.

P. A. Neff, B. K. Wunderlich, S. Q. Lud and A. R. Bausch. Silicon-on-insulator based thin film resistors for quantitative biosensing applications. *phys. stat. sol. (a)*, 203(14):3417-3423, 2006.

C. Reich, P. A. Neff, A. R. Bausch, J. O. Rädler and B. Nickel. Supported membranes on polyelectrolyte layers studied by X-ray reflectometry. *phys. stat. sol. (a)*, 203(14):3463-3467, 2006.

P. A. Neff, B. K. Wunderlich, R. v. Klitzing and A. R. Bausch. Formation and dielectric properties of polyelectrolyte multilayers studied by a silicon-on-insulator based thin film resistor. *Langmuir*, accepted.

P. A. Neff, B. K. Wunderlich and A. R. Bausch. Electrical detection of protease activity by a silicon-on-insulator based thin film resistor. *in preparation.*

B. K. Wunderlich, P. A. Neff and A. R. Bausch. Modelling field effect devices for biosensing applications. *in preparation.*

Danksagung

Ich bedanke mich bei

Prof. Andreas Bausch dafür, dass er es mir ermöglicht hat, an einem so vielseitigen Thema an der Schnittstelle von Physik, Chemie und Biologie zu arbeiten und es nach eigenen Vorstellungen umzusetzen. Dabei konnte ich immer auf seine Unterstützung in fachlicher und persönlicher Hinsicht zählen.

Prof. Regine v. Klitzing, ohne die ich nie in die Tiefen der Polyelektrolytmultilagen vorgedrungen wäre. Sie hat mich nicht nur mit Material und ellipsometrischen Daten versorgt, sondern hatte auch immer ein offenes Ohr für meine Fragen.

Dr. Ali Naji für die gute Zusammenarbeit und dafür, dass er sich die Zeit genommen hat, meine Experimente und Rechnungen nachzuvollziehen.

Bernhard Wunderlich für die hervorragende Zusammenarbeit, für die ausgedehnten und fruchtbaren Diskussionen sowie für das Korrekturlesen meiner Arbeit. Sein unermüdliches Bestreben, alles genau zu verstehen, hat uns sehr viel weitergebracht.

Cornelia Neunteufel für die tolle gemeinsame Zeit im Labor und insbesondere für die Freundschaft darüberhinaus.

Dan Stark für seine Hilfe bei LabVIEW-Problemen und für den Anstoß, mich den Polyelektrolytmultilagen auch theoretisch zu nähern.

Andreas Serr und Prof. Roland Netz, die sehr zu meinem Verständnis der Polyelektrolytadsorption beigetragen haben.

Christian Reich und Dr. Bert Nickel für die Messungen der Röntgenreflektivität und die interessante und spannende Zeit am HASYLAB.

Dr. Christian Ecker für die ellipsometrischen Messungen in Puffer.

Dr. Karin Buchholz, die mir die Halbleitertechnologie beigebracht hat und mir jeder Zeit mit Rat und Tat bei der Chipherstellung zur Seite stand.

Robert Lechner für die vielen Spitzen am Bonder, die er immer schnellstmöglich ausgetauscht hat.

Sonja Matich, Sebastian Strobel und Angelika Stumpf für das Aufdampfen der Kontakte.

Dr. Ulrich Hausmann für das Sägen der Wafer.

Johann Jaud und Michael Schlierf dafür, dass sie mir als Ansprechpartner nicht nur in Computerangelegenheiten zur Seite standen.

Bernd Wagner für die unvergessliche gemeinsame Bürozeit, für die vielen guten Gespräche und seine moralische Unterstützung.

allen Kolleginnen und Kollegen von E22 für das angenehme Arbeitsklima und nicht zuletzt für die zahlreichen E-Mails mit dem Betreff "citcc".

meinem Freund Tobias Zibold dafür, dass er immer für mich da ist, und dafür, dass er stets geduldig, selbst beim Mittagessen, auf all meine Fragen eingegangen ist. Und natürlich für das kritische Lesen meiner Arbeit.

meinen Eltern für ihre ausdauernde persönliche wie finanzielle Förderung, die mir meine Ausbildung bis hin zur Promotion ermöglicht hat.